ISSN: 1947-3931 (Print), 1947-394X (Online) Volume 1, Number 3, November 2009

Engineering

Prof. Hong Liu University of Oklahoma, USA

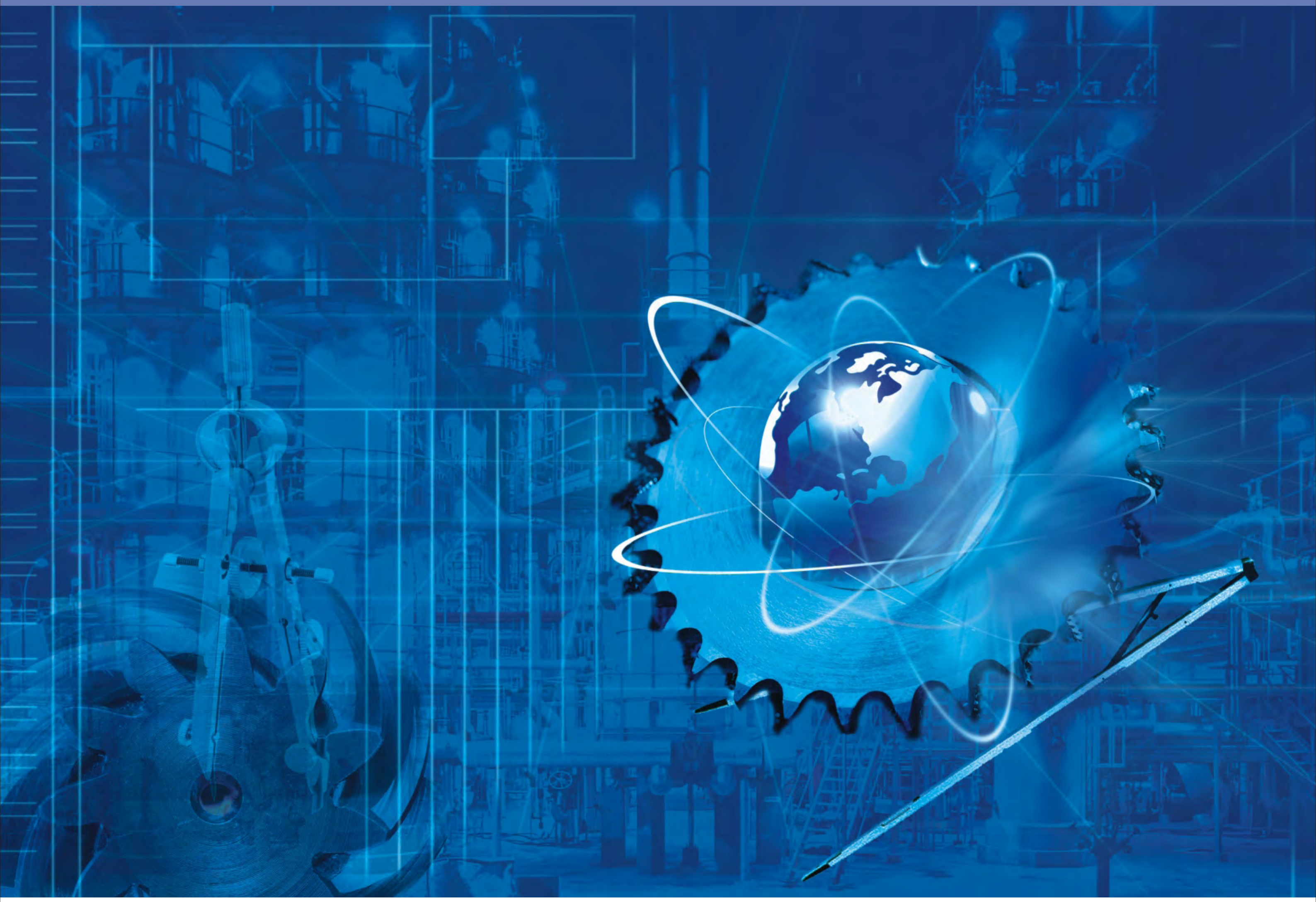

www.scirp.org/journal/eng/

Scientific Research

Journal Editorial Board

ISSN: 1947-3931 (Print), 1947-394X (Online)

http://www.scirp.org/journal/eng

Engineering, **2009, 1, 133-215**
Published Online November 2009 in SciRes (http://www.scirp.org/journal/eng).

TABLE OF CONTENTS

Volume 1 Number 3 November 2009

Engineering

Journal Information

SUBSCRIPTIONS

Engineering (Online at Scientific Research Publishing, www.SciRP.org) is published quarterly by Scientific Research Publishing, Inc., USA.

E-mail: eng@scirp.org

Subscription rates: Volume 1 2009

Print: $50 per copy.

Electronic: free, available on www.SciRP.org.

To subscribe, please contact Journals Subscriptions Department, E-mail: eng@scirp.org

Sample copies: If you are interested in subscribing, you may obtain a free sample copy by contacting Scientific Research Publishing, Inc at the above address.

SERVICES

Advertisements

Advertisement Sales Department, E-mail: eng@scirp.org

Reprints (minimum quantity 100 copies)

Reprints Co-ordinator, Scientific Research Publishing, Inc., USA.

E-mail: eng@scirp.org

COPYRIGHT

PRODUCTION INFORMATION

For manuscripts that have been accepted for publication, please contact:

E-mail: eng@scirp.org

Engineering, **2009, 1, 133-139**
doi:10.4236/eng.2009.13016 Published Online November 2009 (http://www.scirp.org/journal/eng).

Effect of Oscillating Jet Velocity on the Jet Impingement Cooling of an Isothermal Surface

Nawaf H. SAEID
Department of Mechanical, Manufacturing and Materials Engineering,
The University of Nottingham Malaysia Campus, Semenyih, Malaysia
E-mail: *nawaf.saeid@nottingham.edu.my*
Received January 10, 2009; *revised February* 21, 2009; *accepted February* 23, 2009

Abstract

Numerical investigation of the unsteady two-dimensional slot jet impingement cooling of a horizontal heat source is carried out in the present article. The jet velocity is assumed to be in the laminar flow regime and it has a periodic variation with the flow time. The solution is started with zero initial velocity components and constant initial temperature, which is same as the jet temperature. After few periods of oscillation the flow and heat transfer process become periodic. The performance of the jet impingement cooling is evaluated by calculation of friction coefficient and Nusselt number. Parametric study is carried out and the results are presented to show the effects of the periodic jet velocity on the heat and fluid flow. The results indicate that the average Nusselt number and the average friction coefficient are oscillating following the jet velocity oscillation with a small phase shift at small periods. The simulation results show that the combination of Re =200 with the period of the jet velocity between 1.5 sec and 2.0 sec and high amplitude (0.25 m/s to 0.3 m/s) gives average friction coefficient and Nusselt number higher than the respective steady-state values.

Keywords: Heat Transfer, Unsteady Convection, Jet Impingement, Periodic Oscillation, Numerical Study

1. Introduction

Jet Impinging is widely used for cooling, heating and drying in several industrial applications due to their high heat removal rates with relatively low pressure drop. In many industrial applications, such as in cooling of electronics surfaces, the jet outflow is confined between the heated surface and an opposing surface in which the jet orifice is located. Recently many researchers [1–7] have carried out numerical and experimental investigations of laminar impinging jet cooling with different fluids and under various boundary conditions.

The literature review reveals that the behavior of the two-dimensional laminar impinging jet is not well understood. Numerical results of Li *et al*. [8] indicate that there exist two different solutions in some range of geometric and flow parameters of the laminar jet impingement flow. The two steady flow patterns are obtained under identical boundary conditions but only with different initial flow fields. This indicates that the unsteady state analysis is important to have better understanding of the flow and heat transfer in jet impingement. Finite-difference approach was used by Chiriac and Ortega [9] in computing the steady and unsteady flow and heat transfer due to a confined two-dimensional slot jet impinging on an isothermal plate. The jet Reynolds number was varied from Re=250 to 750 for a Prandtl number of 0.7 and a fixed jet-to-plate spacing of H=W= 5. They found that the flow becomes unsteady at a Reynolds number between 585 and 610. Chung *et al*. [10] have solved the unsteady compressible Navier–Stokes equations for impinging jet flow using a high-order finite difference method with non-reflecting boundary conditions. Their results show that the impingement heat transfer is very unsteady and the unsteadiness is caused by the primary vortices emanating from the jet nozzle.

Camci and Herr [11] have showed that it is possible to convert a stationary impinging cooling jet into a self-oscillating-impinging jet by adding two communication ports at the throat section. Their experimental results show that a self-oscillating turbulent impinging-jet configuration is extremely beneficial in enhancing the heat removal performance of a conventional (stationary) impinging jet. It is of great importance to investigate the

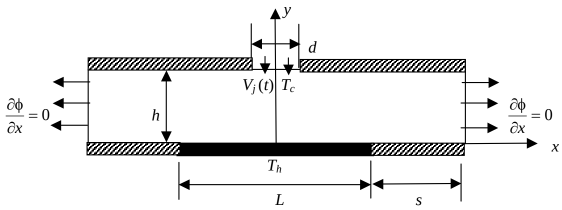

Figure 1. Schematic diagram of the physical model and coordinate system.

effect of periodic flow on the performance of the laminar jet impingement cooling process. Such investigation has been carried out numerically by Poh *et al* [12] to study the effect of flow pulsations on time-averaged Nusselt number under a laminar impinging jet. The target wall in this study is considered from the stagnation point until the exit. The whole target wall is subjected to a constant heat flux. The working fluid is water and the flow is assumed to be axi-symmetric semi-confined. They found that the combination of Re = 300, f = 5 Hz and H/d = 9 give the best heat transfer performance.

In applications such as electronics the components are usually considered as discrete heat sources and the cooling fluid is air. Therefore the objective of the present study is to investigate the periodic laminar jet impingement of air to cool a discrete and isothermal heat source.

2. Mathematical Model

A schematic diagram of impinging jet is shown in Figure 1. The jet exits through a slot of width d with distance h from the target-heated surface. All walls are adiabatic except the target plate where temperature is constant (T_h) and higher than the jet exit temperature (T_c).

The mathematical formulation of the present problem is based on the following assumptions:

1) the flow is two-dimensional, laminar and income-pressible;
2) initial temperature and velocity profiles are assumed to be uniform across the jet width;
3) the thermo-physical properties of the fluid are constants and obtained at average temperature of the jet inlet and heater temperatures; and
4) the viscous heating is neglected in the energy conservation.

Based on the above assumptions, the governing equations for the unsteady heat and fluid flow are as follows:

Mass conservation equation

$$\frac{\partial u}{\partial x}+\frac{\partial v}{\partial y}=0 \tag{1}$$

Momentum conservation equations

$$\frac{\partial u}{\partial t}+u\frac{\partial u}{\partial x}+v\frac{\partial u}{\partial y}=\frac{\partial}{\partial x}\left(\upsilon\frac{\partial u}{\partial x}\right)+\frac{\partial}{\partial y}\left(\upsilon\frac{\partial u}{\partial y}\right)-\frac{1}{\rho}\frac{\partial p}{\partial x} \tag{2}$$

$$\frac{\partial v}{\partial t}+u\frac{\partial v}{\partial x}+v\frac{\partial v}{\partial y}=\frac{\partial}{\partial x}\left(\upsilon\frac{\partial v}{\partial x}\right)+\frac{\partial}{\partial y}\left(\upsilon\frac{\partial v}{\partial y}\right)-\frac{1}{\rho}\frac{\partial p}{\partial y} \tag{3}$$

Energy conservation equation

$$\frac{\partial T}{\partial t}+u\frac{\partial T}{\partial x}+v\frac{\partial T}{\partial y}=\frac{\partial}{\partial x}\left(\alpha\frac{\partial T}{\partial x}\right)+\frac{\partial}{\partial y}\left(\alpha\frac{\partial T}{\partial y}\right) \tag{4}$$

where u and v are velocity components in x and y-directions respectively, T is temperature, p is pressure and t is time. ρ, υ and α are kinematic viscosity and thermal diffusivity of the fluid respectively.

Due to the symmetry around y-axis, only one-half of the flow field is considered for computational purpose. Therefore the initial and boundary conditions are:

Initial condition

$$u(x,y,0) = v(x,y,0) = 0 \text{ and } T(x,y,0) = T_c \tag{5}$$

At x = 0 symmetry

$$\frac{\partial u}{\partial x}=\frac{\partial v}{\partial x}=\frac{\partial T}{\partial x}=0 \tag{6a}$$

At x = (L/2+s) exit

$$\frac{\partial u}{\partial x}=\frac{\partial v}{\partial x}=\frac{\partial T}{\partial x}=0 \tag{6b}$$

At y = 0 lower wall

$$u = v = 0 \text{ and } T = T_h \text{ for } x \le L/2 \text{ otherwise } \frac{\partial T}{\partial y}=0 \tag{6c}$$

At y = h upper boundary

$$u = 0,\ v = -V_j(t) \text{ and } T = T_c \text{ for } x \le d/2 \text{ otherwise } u = v = \frac{\partial T}{\partial y}=0 \tag{6d}$$

The present study investigates the effect of the jet velocity - $V_j(t)$ when it has a periodic variation with the flow time as:

$$V_j(t)=\bar{V}+\varepsilon\times\cos\left(\frac{2\pi}{\tau}t\right) \tag{7}$$

where $\bar{V}$ is the average jet velocity, and ε and τ are the amplitude and period of the oscillation respectively.

The length of the lower adiabatic wall has an important influence on the accuracy of the results, where the exit boundary condition can be realistic. In the present study the length of the lower adiabatic wall is selected to be 3 times the heated surface (L/2) similar to that adopted by Rady [4].

3. Numerical Solution Procedure

The solution domain was meshed by divided it into spacing quadrilateral cells. The cells were clusters near the symmetry axis where steep variations in velocity and temperature are expected.

FLUENT 6.3 is used as a tool for numerical solution of the governing equations based on finite-volume method. QUICK discretization scheme [13] is selected for convection-diffusion formulation for momentum and energy equations. The central differencing scheme is used for the diffusion terms. The discretized equations were solved following the SIMPLEC algorithm [14]. Relaxation factors are used to avoid divergence in the iteration. The typical relaxation factors were used as 0.7 for momentum equations, 0.3 for the pressure and 1.0 for the energy equation. For time integral the first order implicit scheme is used, which is unconditional stable.

The convergence criterion is based on the residual in the governing equations. The maximum residual in the energy was 10^{-7} and the residual of other variables were lower than 10^{-5} in the converged solution. In all the computational cases the global heat and mass balance are satisfied in the converged solution within $\pm 10^{-3}$ %.

Air is used as working fluid with constant physical properties. Most of the benchmark results are presented with constant Prandtl number, Pr = 0.71, for air. The average temperature between the cold incoming jet and the hot plate is selected to be 300K so that the Prandtl number is approximately 0.71. The plate temperature is fixed at 310K and the incoming jet temperature is maintained at 290K. The properties were found from the properties tables of air at an average temperature of 300K as: density ρ = 1.1614 kg/m^3, specific heat c_p = 1007 J/kgK, thermal conductivity k = 0.0263 W/mK and viscosity of $\mu = 1.846\times10^{-5}$ kg/ms.

4. Results and Discussions

The performance of the jet impingement cooling is evaluated based on the friction coefficient and Nusselt number, which are defined respectively as:

$$c_f = \frac{\tau_w}{\frac{1}{2}\rho\bar{V}^2} = \mu\left(\partial u/\partial y\right)_{y=0} \Big/ \tfrac{1}{2}\rho\bar{V}^2 \quad (8)$$

$$Nu = \frac{q_w\, d}{\left(T_h - T_c\right)k} = -d\left(\partial T/\partial y\right)_{y=0} \Big/ \left(T_h - T_c\right) \quad (9)$$

where τ_w is the wall shear stress and q_w is the wall heat flux. The average friction coefficient and the average Nusselt number at the heated plate are also calculated by integrating the local values over the length of the plate as follows:

$$\overline{c_f} = \frac{2}{L}\int_0^{L/2} c_f\, dx \quad (10)$$

$$\overline{Nu} = \frac{2}{L}\int_0^{L/2} Nu\, dx \quad (11)$$

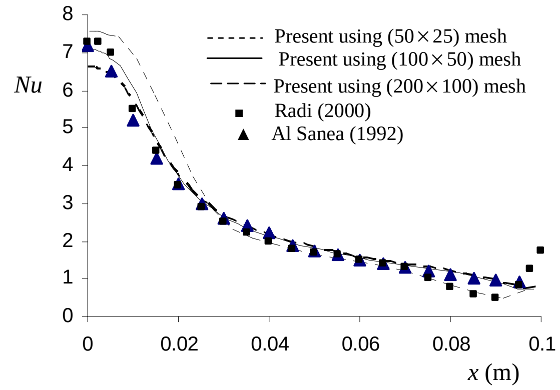

(a)

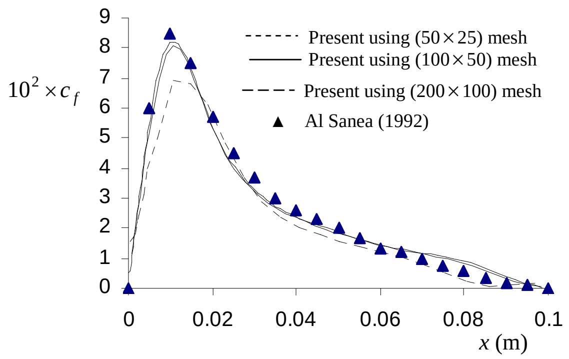

(b)

Figure 2. (a) Variation of Nusselt number along the heated plate.Re = 200, h/d = 4, L/d = 20 and Pr = 0.71; (b) Variation of friction coefficient along the heated plate.Re = 200, h/d = 4, L/d = 20 and Pr = 0.71.

Table 1. Values of $\overline{Nu}$ with grid refinement compared with reference values.

Re	$\overline{Nu}$				
	Al-Senea (1992)	Rady (2000)	Present results using different mesh sizes		
			(50×25)	(100×50)	(200×100)
100	1.596	1.46	1.4880	1.4743	1.4599
200	2.505	2.38	2.4332	2.4539	2.4473

Table 2. Values of average friction coefficient with grid refinement.

Re	V (m/s)	$\overline{c_f}$		
		Present results using different mesh sizes		
		(50×25)	(100×50)	(200×100)
100	0.159	0.030436	0.031934	0.031900
200	0.318	0.025352	0.028638	0.029346

The effect of mesh size on the accuracy of calculating friction coefficient and Nusselt number is studied for steady flow with constant jet velocity. The present results obtained using different mesh sizes are compared with the results of Al-Senea [2] and Rady [4]. The results presented in Figure 2(a) and Table 1 shows the comparison of local and average Nusselt number respectively. Figure 2(b) and Table 2 show the simulation results for local and average friction coefficient respectively. The present results show that the mesh with 100×50 quadrilateral cells in the x and y directions respectively gives results with acceptable accuracy. The mesh is designed so that the jet width, which is d/2 = 0.005 m is divided into 10 cells (control volumes). The heated surface L/2 = 0.1 m (which gives L/d = 20) is discretized into 50 divisions and the remaining adiabatic lower wall is divided into 50 divisions. The height h = 0.04 m (where h/d = 4) in the vertical direction is divided into 50 divisions. The results shown in Figures 2 and Tables 1 and 2 also show that halving or duplicating the mesh size have minor effects on the values of the Nusselt number and friction coefficient. Therefore the results obtained using mesh with 100×50 quadrilateral cells can be considered as grid independent results. Good agreements of the present results with those references cited in [2] and [4] are observed for two different values of the Reynolds number in the laminar regime. Where Re is the Reynolds number defined based on average jet velocity and jet width as: $\mathrm{Re}=\rho\overline{V}d/\mu$. It is worth mentioning that the values of $\overline{c_f}$ are not listed in the references [2] and [4].

In unsteady flows in general and especially periodic flows, the time step size has a great influence of the accuracy of the results. The time step size can be made to be a function of the frequency/period of the flow oscillation as implemented by Saeid [15,16]. In the present periodic flow problem, the time step size is selected a function of the period of the jet flow oscillation as $\Delta t=\tau/100$ sec.

To study the effect of the amplitude ε of the oscillation on the flow, the jet velocity is made to oscillate with time according to Equation (7) with fixed values of period τ = 10 sec and Re = 200. It is important to note that the definition of Reynolds number in the present study is based on average jet velocity. To get Re = 200, the average jet velocity should be 0.318 m/s since the geometry of the problem and the air properties are assumed constants. Therefore the maximum amplitude of the oscillation is selected to be 0.3 m/s so that there will be always positive impinging velocity on the target surface.

The initial conditions in the unsteady simulation are defined in (5) which assume that the solution domain is filled with stagnant air at jet temperature. Then the jet starts to inflow and the target surface temperature in-

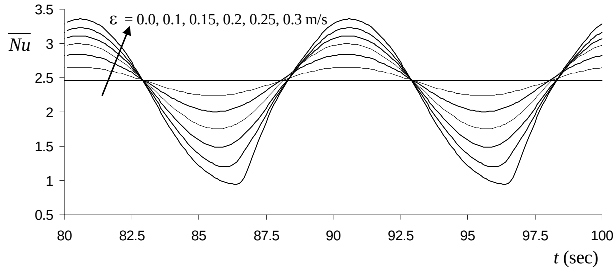

(a)

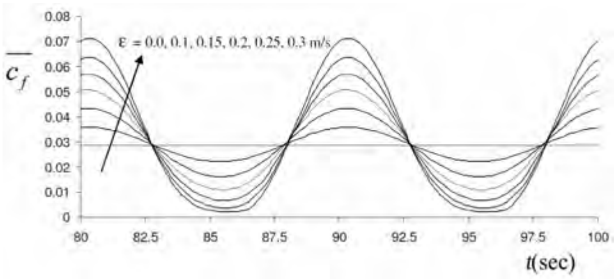

(b)

Figure 3. (a) Oscillation of $\overline{Nu}$ with τ = 10 sec and Re = 200; (b) Oscillation of $\overline{c_f}$ with τ = 10 sec and Re = 200.

creases suddenly from T_c to T_h. At this time the value of Nusselt number goes to very high value. Then, when the jet velocity oscillates the calculated values of average Nusselt number is found to oscillate accordingly. This oscillation becomes steady periodic oscillation after some periods of oscillation. The steady periodic oscillation is achieved when the amplitude and the average values of the average Nusselt number become constant for different periods.

The numerical results of oscillation of the average Nusselt number in the ninth and tenth periods with τ = 10 sec and Re = 200 is shown in Figure 3(a). The corresponding oscillation of the average friction coefficient in the ninth and tenth periods is shown in Figure 3(b).

Both the Nusselt number and the friction coefficient are observed to oscillate in all the cases for different values of ε with a small phase change with the jet oscillation (which is cosine wave). For small values of the amplitude of the jet inflow oscillation (ε = 0.1 m/s to 0.2 m/s), the calculated average Nusselt number is oscillating in smooth sinusoidal oscillation as shown in Figure 3.

The effect of the period of the jet inflow velocity is studied and the results are shown in Figures 4a and 4b as $\overline{Nu}$ against ωt and $\overline{c_f}$ against ωt respectively, where ω is the frequency of the oscillation ($\omega=2\pi/\tau$). Figure 4 shows clearly how the period of the jet velocity influences the periodic variation of $\overline{Nu}$ and $\overline{c_f}$ for

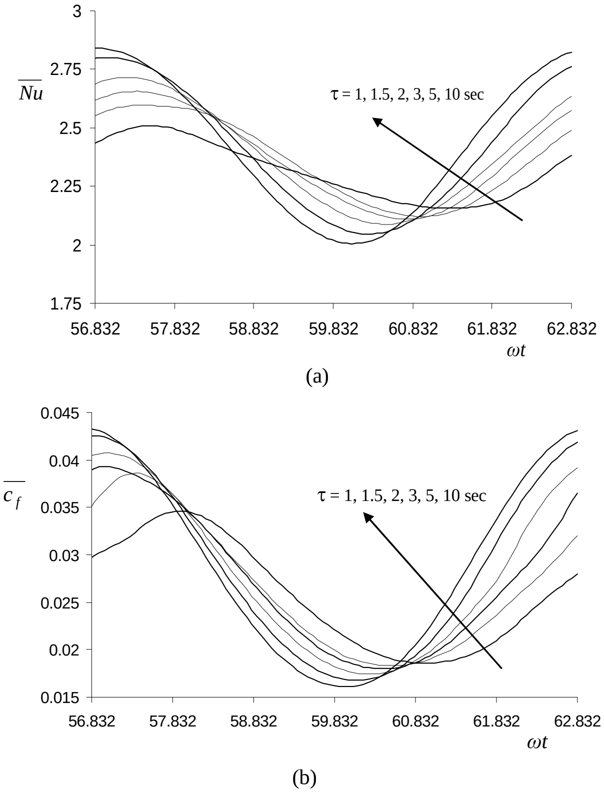

Figure 4. (a) Periodic oscillation of $\overline{Nu}$ with ε = 0.1 m/s, and Re = 200; (b) Periodic oscillation of $\overline{c_f}$ with ε = 0.1 m/s, and Re = 200.

Re = 200 with forcing amplitude ε = 0.1. At high values of τ there will be enough time for the momentum and heat transfer to follow the effect of the periodic variation of the jet velocity. Therefore the average Nusselt number and average friction coefficient are found to follow the jet velocity function (cosine-function) for high values of τ (5 and 10) as shown in Figure 4.

The amplitude of both the average Nusselt number and average friction coefficient oscillation is higher for larger periods of jet oscillation. Figure 4 shows also, as τ decreases, the peak values of average Nusselt number and average friction coefficient are delayed.

The results presented in Figures 3 and 4 show the oscillation of both the average Nusselt number and average friction coefficient according to the jet velocity oscillation; therefore it is important to introduce the cyclic average value of the space-averaged friction coefficient and Nusselt number defined respectively as:

$$\overline{\overline{c_f}} = \frac{1}{\tau}\int_{t_o}^{t_o+\tau} \overline{c_f}\, dt \tag{12}$$

$$\overline{\overline{Nu}} = \frac{1}{\tau}\int_{t_o}^{t_o+\tau} \overline{Nu}\, dt \tag{13}$$

where t_o represents the time required to reach the steady periodic oscillation process (around 9 periods of oscillation). Figures 5(a) and 5(b) show respectively the variation of $\overline{\overline{Nu}}$ and $\overline{\overline{c_f}}$ with ε for different values of the period of the jet oscillation and constant Re =200.

For small values of ε (less than 0.15 m/s), the cyclic average value of the space-averaged Nusselt number ($\overline{\overline{Nu}}$) is decreasing with the increase of either ε or τ as shown in Figure 5(a). Figure 5(b) shows that $\overline{\overline{c_f}}$ also decr- eases with the increase of either ε or τ for small values of ε.

This means that the cooling process is deteriorated by using oscillating jet under these conditions. The results presented in Figure 5 show also the possibility of cooling enhancement when the period of the jet velocity between 1.5 sec and 2.0 sec and high amplitude (0.25 m/s to 0.3 m/s) with Re = 200.

At these conditions the cyclic average value of both the space-averaged friction coefficient and Nusselt number are found to be higher than the steady-state value (when ε = 0) as shown in Figure 5.

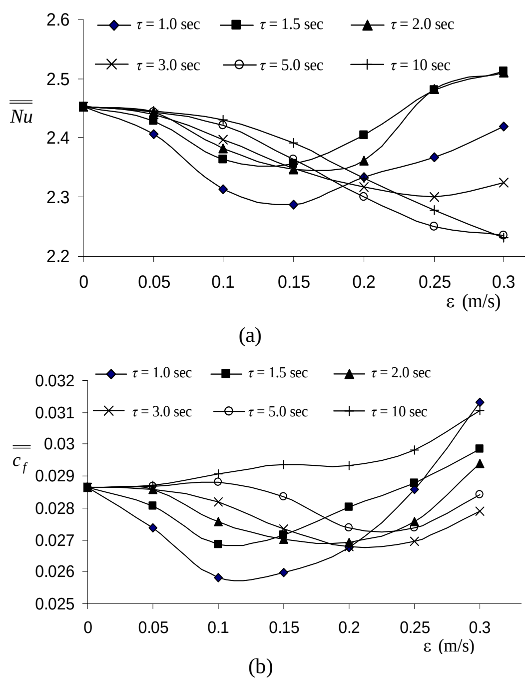

Figure 5. (a) Variation of $\overline{\overline{Nu}}$ with ε at Re =200; (b) Variation of $\overline{\overline{c_f}}$ with ε at Re =200.

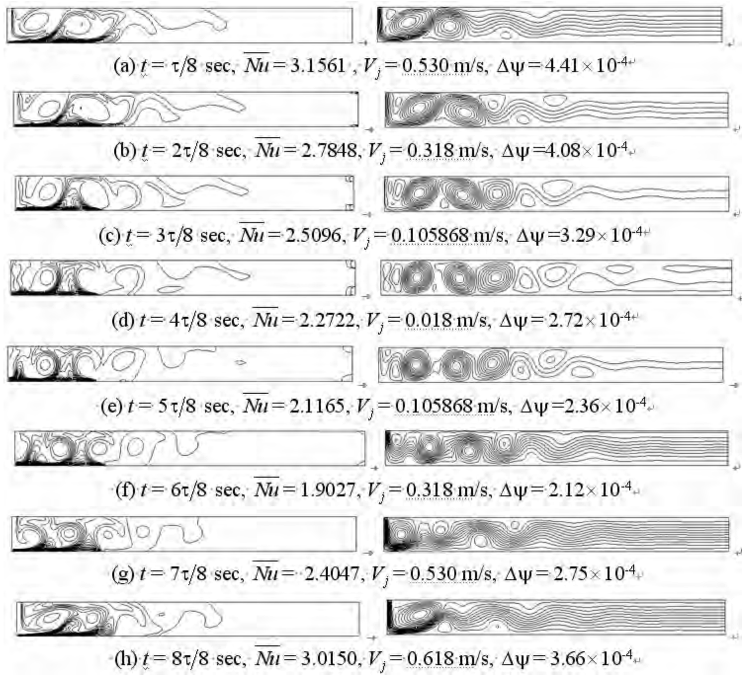

Figure 6. Isotherms, ΔT = 1K (left) and streamlines (right) for a cycle of oscillation with ε = 0.3 m/s, τ = 2 sec, and Re= 200.

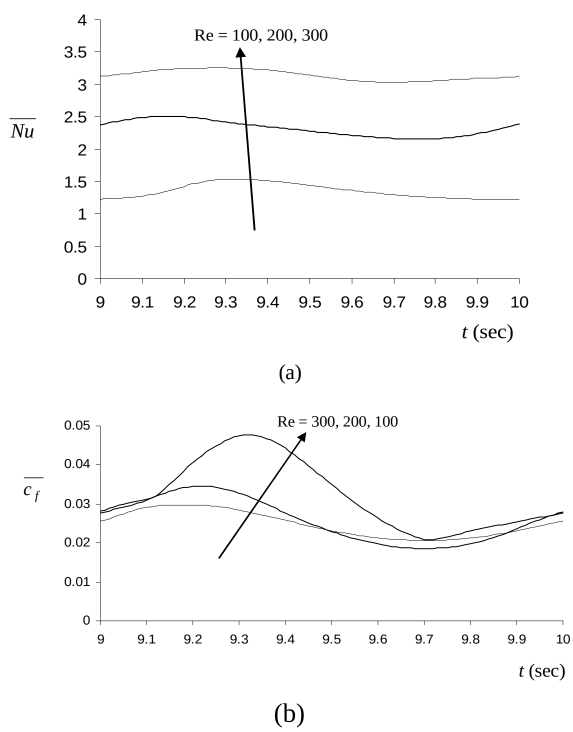

Figure 7. (a) Periodic oscillation of $\overline{Nu}$ with ε = 0.1 m/s and τ = 1 sec; (b) Periodic oscillation of $\overline{c_f}$ with ε = 0.1 m/s and τ = 1 sec.

From the results presented in Figure 5 it can be seen that the increase of $\overline{\overline{Nu}}$ is about 2.3% while the increase in $\overline{\overline{c_f}}$ is 2.6% when the period of the jet velocity is 2.0 sec and amplitude of 0.3 m/s with Re = 200.

In order to have better understanding, the period of the last cycle is divided into eight time steps. At each time step the isotherms and streamlines are shown in Figure 6 for the periodic oscillation with ε = 0.3 m/s, τ = 2 sec and Re = 200.

The isotherms show some high temperature points on the heated target wall. These hot spots are moving along the heated surface according to the jet velocity oscillation. Obviously when the jet velocity is small near the minimum at $t = 4\tau/8$ sec (V_j =0.018 m/s) the temperature near the target surface is high. Figure 6 show that the oscillation of the jet velocity leads to wash away the heated spots after they appear above the heated surface with some delay. The average Nusselt number value at $t = \tau/8$ sec (V_j = 0.530 m/s) is higher that that at maximum velocity at $t = 8\tau/8$ sec, (V_j = 0.618 m/s).

Finally the effect of the Reynolds number on the periodic jet impingement cooling process is studied and the results are depicted on Figure 7. The range of the Reynolds number is selected to be in the laminar regime. Obviously increasing the Reynolds number by increasing the jet velocity leads to the increase in the average Nusselt number and reduce the friction coefficient as shown in Figure 7(a) and (b) respectively. It is observed that the oscillation of both the average Nusselt number and the average friction coefficient at different values of Re have small phase shift in the steady periodic oscillation as shown in Figure 7.

5. Conclusions

In the present study the periodic laminar jet impingement cooling of a horizontal surface is consider for numerical investigation. The periodic jet impingement cooling is generated when there is periodic oscillation of the jet inflow velocity. It has been shown that the Nusselt number oscillates as a result of oscillating jet inflow velocity. The results are presented to show the effects of the amplitude and the period of the jet velocity on the Nusselt number and friction coefficient in the steady periodic state. The results indicate that both the average friction coefficient and Nusselt number are oscillating following the jet velocity oscillation with a small phase change. The periodic average friction coefficient and the Nusselt number are found to follow the jet velocity function for high values of period τ. This is due to the fact that there is enough time for the momentum and heat transfer to follow the effect of the periodic variation of the jet velocity. The simulation results show that it is possible to enhance the cooling process for some combination of the Reynolds number with period and amplitude of the jet velocity. The combination of Re =200 with the period of the jet velocity between 1.5 sec and 2.0 sec and high amplitude (0.25 m/s to 0.3 m/s) gives average friction coefficient and Nusselt number higher than the respective steady-state values.

6. References

[1] E. M. Sparrow and T. C. Wong, “Impingement transfer coefficient due to initially laminar slot jets,” Int. J. Heat Mass Transfer, Vol. 18, pp. 597–605, 1975.

[2] S. Al-Sanea, “A numerical study of the flow and heat transfer characteristics of an impinging laminar slot-jet including crossflow effects,” Int. J. Heat Mass Transfer, Vol. 35, pp. 2501–2513, 1992

[3] Z. H. Lin, Y. J. Chou, and Y. H. Hung, “Heat transfer behaviors of a confined slot jet impingement,” Int. J. Heat Mass Transfer, Vol. 40, pp. 1095–1107, 1997.

[4] M. A. Rady, “Buoyancy effects on the flow and heat transfer characteristics of an impinging semi-confined laminar slot jet,” Int. J. Trans. Phenomena, Vol. 2, pp. 113–126, 2000.

[5] H. Chattopadhyay and S. K. Saha, “Simulation of laminar slot jets impinging on a moving surface,” J. Heat Transfer, Vol. 124, pp. 1049-1055, 2002.

[6] L. B. Y. Aldabbagh, I. Sezai, and A. A. Mohamad, “Three- dimensional investigation of a laminar impinging square jet interaction with cross flow,” J. Heat Transfer, Vol. 125, pp. 243–249, 2003.

[7] D. Sahoo and M. A. R. Sharif, “Numerical modeling of slot-jet impingement cooling of a constant heat flux surface confined by a parallel wall,” Int. J. Therm. Sci., Vol. 43, pp. 877–887, 2004.

[8] X. Li, J. L. Gaddis, and T. Wang, “Multiple flow patterns and heat transfer in confined jet impingement,” Int. J. Heat Fluid Flow, Vol. 26, pp. 746–754, 2005.

[9] V. A. Chiriac and A. Ortega, “A numerical study of the unsteady flow and heat transfer in a transitional confined slot jet impinging on an isothermal surface,” Int. J. Heat Mass Transfer, Vol. 45, pp. 1237–1248, 2002.

[10] Y. M. Chung, K. H. Lao, and N. D. Sandham, “Numerical study of momentum and heat transfer in unsteady impinging jets,” Int. J. Heat Fluid Flow, Vol. 23, pp. 592–600, 2002.

[11] C. Camci and F. Herr, “Forced convection heat transfer enhancement using a self-oscillating impinging planar jet,” J. Heat Transfer, Vol. 124, pp. 770–782, 2002.

[12] H. J. Poh, K. Kumar, and A. S. Mujumdar, “Heat transfer from a pulsed laminar impinging jet,” Int. Comm. Heat Mass Transfer, Vol. 32, pp. 1317–1324, 2005.T. Hayase, J. A. C. Humphrey, and R. Greif, “A consistently formulated QUICK scheme for fast and stable convergence using finite-volume iterative calculation procedures,” J. Comput. Phys., Vol. 98, pp. 108–118, 1992.

[14] H. K. Versteeg and W. Malalasekera, “Computational fluid dynamics: An introduction,” Longman, 1995.

[15] N. H. Saeid, “Periodic free convection from vertical plate subjected to periodic surface temperature oscillation,” Int. J. Therm. Sci., Vol. 43, pp. 569–574, 2004.

[16] N. H. Saeid, “Mixed convection flow along a vertical plate subjected to time-periodic surface temperature oscillations,” Int. J. Therm. Sci., Vol. 44, pp. 531–539, 2005.

Engineering, 2009, 1, 140-150
doi:10.4236/eng.2009.13017 Published Online November 2009 (http://www.scirp.org/journal/eng).

Multi-Area Unit Commitment Using Hybrid Particle Swarm Optimization Technique with Import and Export Constraints

S. R. P. CHITRA SELVI[1], R. P. KUMUDINI DEVI[2], C. CHRISTOBER ASIR RAJAN[3]
[1]*Department of Electrical Engineering, Anna University, Chennai, India*
[2]*Department of Electrical Engineering, Anna University, Chennai, India*
[3]*Department of Electrical Engineering, Pondicherry Engg.College, Pondicherry, India*
E-mail: *prakasini*2004*@yahoo.co.in, kumudinidevi@annauniv.edu, asir_*70*@hotmail.com*
Received January 10, 2009; *revised February* 21, 2009; *accepted February* 23, 2009

Abstract

This paper presents a novel approach to solve the Multi-Area unit commitment problem using particle swarm optimization technique. The objective of the multi-area unit commitment problem is to determine the optimal or a near optimal commitment strategy for generating the units. And it is located in multiple areas that are interconnected via tie lines and joint operation of generation resources can result in significant operational cost savings. The dynamic programming method is applied to solve Multi-Area Unit Commitment problem and particle swarm optimization technique is embedded for computing the generation assigned to each area and the power allocated to all committed unit**.** Particle Swarm Optimization technique is developed to derive its Pareto-optimal solutions**.** The tie-line transfer limits are considered as a set of constraints during the optimization process to ensure the system security and reliability. Case study of four areas each containing 26 units connected via tie lines has been taken for analysis. Numerical results are shown comparing the cost solutions and computation time obtained by using the Particle Swarm Optimization method is efficient than the conventional Dynamic Programming and Evolutionary Programming Method.

Keywords: Multi-Area Unit Commitment, Evolutionary Programming, Dynamic Programming Method, Particle Swarm Optimization Method

1. Introduction

In an interconnected system, the objective is to achieve the most economical generation that could satisfy the local demand without violating tie-line capacity constraints. Due to inter-area transmission constraints, multi-area unit commitment problems (MAUC) are very complicated when compared with single-area unit commitment problems. Research explores that the application of these existing single-area unit commitment to multi-area unit commitment problem is required [1–4].

Furthermore, unit commitment is treated, as separately from the economic dispatch, the linear fuel cost curve may be an expensive operation schedule or a violation of spinning reserve requirements. In multi-area systems, local generations are not equal to local load demands. Areas with lower fuel cost units may generate more power than their demand and export the excessive energy to the deficient areas; likewise, areas with higher fuel cost units will generate less power than their demand and import the additional energy from other areas with surplus capacity. So, the unit commitment of an area should comply with the local generation as well as the local load demand. References [5–11] provide comprehensive study on multi-area scheduling by relating unit commitment and economic dispatch with tie-line constraints. The following paragraph discusses some of the method, which is adopted in the multi-area unit commitment problem and their implications.

There are some drawbacks in implementing the simple priority list method for unit commitment. Although the technique was fast, the results are far from optimal, especially when there are massive on/off transitions. Another difficulty is in which did not deal with topological connections in a multi-area system as it considered export/import limitations, which would cause infeasible solutions in many applications. Another approach [6] overcame the previous difficulties. It considered the topological constraints and enhanced unit commitment with economic dispatch .The λ iteration method takes excessive time in finding the optimal solution in large-scale power systems and the speed of the algorithm required some improvement. In the iterative procedure between unit commitment and economic dispatch, there is a need to adjust the unit commitment according to the required area generation. If we use Dynamic Programming Sequential Combination (DP-SC) for unit commitment in a power pool, the search for an optimal solution is very time consuming. If we adopt the priority list method, there may be a solution gap between the resultant schedule and the actual economic operation schedule. If we repeat the process, we may reduce the operation cost, but it will demand a longer execution time. The DP-SC method is used for unit–commitment problem in an interconnected area and particle swarm optimization technique is embedded for assigning generation to each area and modifying the economic dispatch schedule.

In this paper, we propose a more efficient approach to the multi-area generation dispatch problem. The proposed technique is used to improve the speed and reliability of the optimal search process. Instead of using λ iteration method in assigning power generation to each area, we used particle swarm optimization to find the optimal allocation of power generation in each area and entire system. Using particle swarm optimization techniques in each area and entire system, we can save time in performing the economic dispatch and operating cost.

The meta-heuristic methods [12–19] are iterative techniques that can search not only local optimal solutions but also a global optimal solution depending on the problem domain and time limit. In the meta-heuristic methods, the techniques frequently applied to the UC problem are genetic algorithm (GA), tabu search (TS), evolutionary programming (EP), simulated annealing (SA), particle swarm optimization (PSO), etc. They are general-purpose search techniques based on the principles inspired from the genetic and evolution mechanisms observed in natural systems and populations of living beings. These methods have the advantage of searching the solution space more thoroughly. The main difficulty is their sensitivity to the choice of parameters.

In this paper, section one introduces that the mathematical model of the multi-area unit commitment problem. In the problem formulation, DP method is used for committing the unit in each area and λ iteration method is used for importing and exporting power to other area and minimizes the operating cost. Furthermore, tie-line transfer capacities and area spinning reserve requirements are also incorporated in order to ensure system security and reliability. The Reserve-sharing scheme is used to enable the area without enough capacity to meet its reserve demand. The objective of MAUC, constraints and conditions of optimal solution are also discussed in this section. Section 3 and 4 explains the EP and PSO algorithm adopted for importing and exporting power to other area. Section 5 gives the results of a case study each one based on a four-area system. A four-area IEEE test power system [6] is then used as an application example to verify the effectiveness of the proposed method through numerical simulations. A comparative study is also made here to illustrate the different solutions obtained based on conventional, EP and PSO methods. Conclusions are presented in the last section.

2. Problem Formulation

The cost curve of each thermal unit is in quadratic form

$$F({Pg_i}^k) = a_i^k ({Pg_i}^k)^2 + b_i^k ({Pg_i}^k) + c_i^k \text{ :\$/hr k=1 } N_A \tag{1}$$

The incremental production cost is therefore

$$\lambda = 2a_i^k {Pg_i}^k + b_i^k \tag{2}$$

or

$${Pg_i}^k = \lambda - b_i^k \;\; / 2a_i^k \tag{3}$$

The start up cost of thermal unit is an exponential function of the time that the unit has been off

$$S(X_{i,j}^{off}) = A_i + B_i (1 - e^{X_{i,j}^{off}}) \tag{4}$$

2.1. Multi-Area Unit Commitment

The objective function for the multi-area unit commitment is to minimize the entire power pool generation cost as follows:

$$\min_{I,P} \sum_{k=1}^{N_A} \sum_{j=1}^{t} \sum_{i=1}^{N_k} [I_{i,j}^k F_j^k (Pg_{i,j}^k) + I_{i,j} (1 - I_{i,j-1}) S_i (X_{i,j-1}^{off}) \tag{5}$$

and the following constraints are to be met for optimization

1) System power balance constraints

$$\sum_k Pg_j^k = \sum_k D_j^k + W_j ;\; j = 1.......t \tag{6}$$

where $\sum_k Pg_j^k \;=\; \sum_k Pg_{i,j}^k$

2) Spinning reserve constraints in each area

$$\sum_i \overline{Pg_i^k} \geq D_j^k + R_j^k + E_j^k - L_j^k \text{ ;j=1…t} \tag{7}$$

3) Generation limits of each unit

$$\underline{Pg}_j^k \leq Pg_{i,j}^k \leq \overline{Pg}_j^k \text{ ;i=1…}N_k\text{;j=1…t;k=1…}N_A \tag{8}$$

4) Minimum Up and Down time constraints

$$(X_{i,j-1}^{off} - T_i^{on}) * (I_{i,j-1} - I_{i,j}) \geq 0 \quad (9)$$

$$(X_{i,j-1}^{off} - T_i^{off}) * (I_{i,j-1} - I_{i,j}) \geq 0 \quad (10)$$

To decompose the problem in Equation (5), it is re-written as

$$\min_{P} \sum_{j=1}^{t} [F(Pg_{i,j})] \quad (11)$$

where

$$F(Pg_{i,j}) = \sum_{k=1}^{N_k} F^k (Pg_{i,j}^k) \quad (12)$$

subject to the constraints of Equation (6) and (8) and following constraints.

5) Export/Import constraints

$$\sum_i Pg_{i.j}^k \leq D_j^k + E_{j\max}^k \quad (13)$$

$$\sum_i Pg_{i,j}^k \geq \sum_k D_j^k - L_{j\max}^k \quad (14)$$

$$\sum_i E_j^k - \sum_k L_j^k + W_j = 0 \quad (15)$$

6) Area generation limits

$$\sum_i Pg_{i,j}^k \leq \sum_i \overline{Pg_i^k} - R_j^k \; ; k = 1 \ldots N_A \; ; \; j = 1 \ldots t \quad (16)$$

$$\sum_i Pg_{i,j}^k \geq \sum_i \underline{Pg_i^k} \; ; k = 1 \; N_A \; ; \; j = 1 \ldots t \quad (17)$$

Each $F^k(Pg_{i,j}^k)$ for $k = 1 \ldots, N_A$ is represented in the form of schedule tables, which is the solution of the mixed variables optimisation problem

$$\min_{I,P} \sum_i [I_{i,j}^k F_i^k (Pg_{i,j}^k) + I_{i,j}(1 - I_{i,j-1}) S_i (X_{i,j}^{off})] \quad (18)$$

Subject to constraints of Equation (7), (9-10) and initial on/off condition of each unit.

The multi-area unit commitment problem is solved by Dynamic Programming Sequential Combination (DP-SC) method to form the optimal generation scheduling approach. Among the available generating units in the interconnected multi-area system and the proposed method sequentially identifies, via a procedure that resembles bidding, the most advantageous units to commit until the multi-area system obligations are fulfilled and this method has been explained [13].

2.2. Multi-Area Economic Dispatch

The objective of Multi-area Economic Dispatch (MAED) is to determine the allocation of generation of each unit in the system and power exchange between areas so as to minimize the total production cost. The lamda–iteration method is implemented in the MAED to include area import and export constraints and tie-line constraints [15]

The objective is to select λ_{sys} every hour to minimize the operation cost.

$$Pg_j^k = D_j^k + E_j^k - L_j^k \quad (19)$$

where $Pg_j^k = \sum_{i=1}^{N_k} Pg_{i,j}^k$

Since the local demand D_j^k is determined in accordance with the economic dispatch within the pool , changes of P_{gj}^k will cause the spinning reserve constraint of Equation (7) to change accordingly and redefine Equation(18).

In this study, the iterative equal incremental cost method (λ method) was used to solve Equation (11) and serve as a coordinator between unit commitments in various areas. With the λ iteration, the system would operate at an optimal point if λ for each unit is equal to a system incremental cost λ_{sys} .Units may operate in one of the following modes when commitment schedule and unit generation limits are encountered:

1) Coordinate mode: The output of unit i is determined by the system incremental cost

$$\lambda_{\min,i} \leq \lambda_{sys} \leq \lambda_{\max,i} \quad (20)$$

2) Minimum mode: Unit i generation is at its minimum level.

$$\lambda_{\min,i} > \lambda_{sys} \quad (21)$$

3) Maximum mode: Unit i generation is at its maximum level.

$$\lambda_{\max,i} < \lambda_{sys} \quad (22)$$

4) Shut down mode: Unit i *is* not in operation, $Pg_i = 0$.

Besides limitations on individual unit generations, in a multi-area system, the tie-line constraints in Equation (9), (10) and (14) are to be preserved. The operation of each area could be generalized into one of three modes as follows:

Area coordinate mode

$$\lambda^k = \lambda_{sys} \quad (23)$$

$$D_j^k - L_{\max}^k \leq \sum_i P_{i,j}^k \leq D_j^k + E_{\max}^k \quad (24)$$

or

$$-L_{\max}^k \leq \sum_i Pg_{i,j}^k - D_j^k \leq E_{\max}^k \quad (25)$$

a. Limited export mode

When the generating cost in one area is lower than the cost in the remaining areas of the system, that area may generate its upper limit according to Equation (13) or (16), therefore,

$$\lambda^k < \lambda_{sys} \quad (26)$$

λ^k is the optimal equal incremental cost which satisfies the generation requirement in each area k.

b. Limited import mode

An area may reach its lower generation limit according to Equation (14) or (17), because of the higher generation costs.

$$\lambda_{\min}^k > \lambda_{sys} \quad (27)$$

The proper generation schedule in multi-area will result by satisfying tie-line constraints and minimizing the system generation cost.

2.3. Tie-Line Flow of Four Areas

An economically efficient area may generate more power than the local demand, the excess power will be exported to the other areas through the tie-lines. As shown in Fig. 1, assume area 1 has excess power, the line flows would have directions from area 1 to other areas, and the maximum power generation for area 1 would be the local demand in area 1 plus the sum of all the tie-line capacities connected to area 1. If we fix the area 1 generation at its maximum level, then the maximum power generation in area 2 could be calculated in a similar way to area 1.

Since tie-line imports power at its maximum capacity, this amount should be subtracted from the generation limit of area 2. According to the system power balance equation some areas must have a power generation deficiency, and require generation imports. The minimum generation level of these areas is the local demand, minus all the connected tie-line capacities. If any of these tie lines is connected to an area with higher deficiencies, then the flow directions should be reversed. The tie-line flow details of four area and directional matrix were presented in [9].

Directional matrix: It indicates power flow direction from one area to another area.

$D_{l,k} =$ [1 when line flows from l to k l >k [-1 when line flows from k to l

$D_{l,l} = 0, D_{l.k} = -D_{k,l}$ initial $D_{l.k}$ are zero

3. Evolutionary Programming Method

3.1. Introduction

EP is a mutation-based evolutionary algorithm applied to discrete search spaces. D. Fogel (Fogel, 1988)] extended the initial work of his father L. Fogel (Fogel, 1962) [15–18] for applications involving real-parameter optimization problems. Real-parameter EP is similar in prin

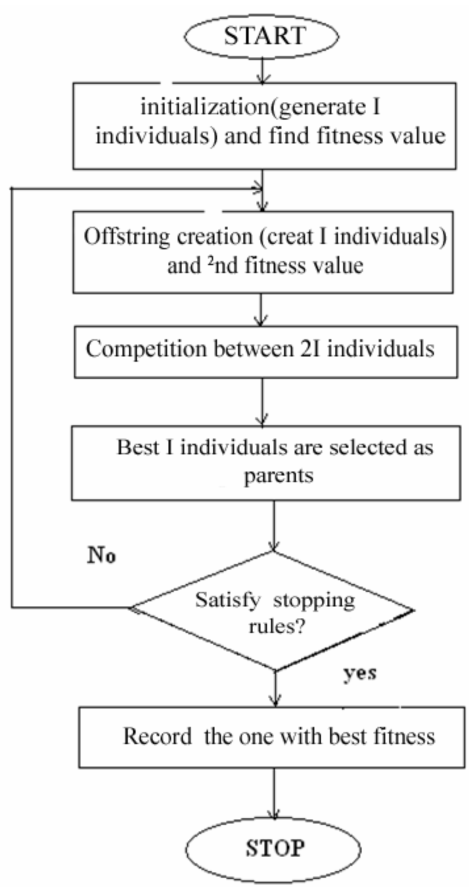

Figure 1. Flow chart for evolutionary algorithm.

ciple to evolution strategy (ES), in that normally distributed mutations are performed in both algorithms. Both algorithms encode mutation strength (or variance of the normal distribution) for each decision variable and a self-adapting rule is used to update the mutation strengths. Several variants of EP have been suggested (Fogel, 1992).

3.2. Evolutionary Programming Algorithm

The original Evolutionary Programming involved evolving populations of extending algorithms to develop artificial intelligence [17]. In this technique a strong behavioral link is sought between each parent and its offspring, at the level of the species.Fig.1 shows e general scheme of the EP algorithm.

3.3. Implementation of Evolutionary Algorithm for Multi-Area Unit Commitment Problem

Step (1): Read in unit data, tie-line data, demand profile.
Step (2): Perform the dynamic programming to get the initial commitment schedule for each area.

Step (3): Initialization of parent population. The initial parent population of size Np is randomly generated for committed unit in each area:

1) To generate the initial parent population

$$I_p = [(p_{g1}^{kp} ....p_{gN}^{kp})]; k = 1,2,3,4 \;\&\; p = 1,2...N_p ; \quad (28)$$

2) To calculate the fuel cost for each population using Equation (1)

$$FC_p^K = [(a(Pg_1^{kp})^2 + b(Pg_1^{kp}) + c); k = 1,2,3,4 \;\&\; p = 1,2...N_p \quad (29)$$

3) To calculate the start up cost for each population using Equation (4)

4) To calculate the production cost Production

$$\text{cost}= FC_p^k + SC_p^k \quad (30)$$

5) To calculate the fitness function for each parent of population

$$F_P = FC_P^K + SC_P^K + K(\sum_{i=1}^{Nk} PG_i^{kp} - D_j^k) \quad (31)$$

The values of the penalty factor is chosen such that if there are any constraints violations then the fitness function value corresponding to that parent will be ineffective.

Step (4): Mutation

1) To generate an offspring population Io of size from Np from each parent Ip

$$I_O = [(Pg_1^{ko} ....Pg_N^{ko}); k = 1,2,3,4; 0 = 1.....N_p \quad (32)$$

generated as

$$Pg_i^{KO} = Pg_i^{KO} + N(0,\sigma^2 Pg_i^K); i = 1,2......N$$

Similarly all Pg_i is generated for all areas subjected to

$$\mathrm{Pg}_i^{ko} = \mathrm{Pg}_{i,\min} \;;\ \text{if } \mathrm{Pg}_i^{ko} < \mathrm{Pg}_{i,\min}$$

$$\mathrm{Pg}_i^{ko} = \mathrm{Pg}_{i,\max} \;;\ \text{if } \mathrm{Pg}_i^{KO} > \mathrm{Pg}_{i,\max} \quad (33)$$

$N(0,\sigma^2)$ represents a normal random variable with zero mean and standard deviation

$$\sigma_{Pg_i} = \beta * (F_{pi} / F_{\max}) * (\sigma_{ij,\max} - \sigma_{ij,\min}) \quad (34)$$

where β is scaling factor, F_{pi} is the value of fitness function corresponding to I_i and $F_{\max}$ is the maximum fitness function value among parent population

2) To compute the fitness value corresponding to each offspring using Equation (31)

Step (5): (competition and selection). The 2*I* individuals compete with each other for selection using Equation (6). A weight value W_i is assigned to each individual as follows:

$$W_i = \sum_{t=1}^{I} W_t \quad (35)$$

$$W_t = \{1, if \quad u < (f_t / f_t + f_i)$$

$$W_t = \{0, otherwise \quad (36)$$

where f_t is the fitness of the i^{th} competitor randomly selected from 2*I* individuals and *u* is a uniform random number ranging over [0, 1].While computing the weight for each individual, it is ensured that each individual is selected only once from the combined population. Even though relative fitness values are used during the process of mutation, competition and selection, it leads to slow convergence. This is because the ratio $f_t /(f_t + f_i)$ is always around 0.5 without uniform distribution between 0 and 1.Hence, the following strategy is followed in this paper to assign weights:

$$W_t = \{1, if \quad f_t /(f_t + f_i) > 0.5 \quad (37)$$

$$W_t = \{0, otherwise$$

This weight assignment is found to yield proper selection and good convergence. When all the 2*I* individuals obtain their weights, they are ranked in descending order and the first *I* individuals are selected as parents along with their fitness values for next generation.

Steps (4) and Steps (5) are repeated until there is no appreciable improvement in the minimum fitness value.

Step (6): Optimum generation schedule is obtained for four areas using minimum fitness value. Check area generation with local demand

Step (7): Areas with lower fuel cost may export the excessive generation to other areas with higher fuel cost (deficiency areas) with tie line limit.

4. Particle Swarm Optimization

Particle swarm optimization (PSO) is inspired from the collective behavior exhibited in swarms of social insects [19]. It has turned out to be an effective optimizer in dealing with a broad variety of engineering design problems. In PSO, a swarm is made up of many particles, and each particle represents a potential solution (i.e., individual). A particle has its own position and flight velocity, which are adjusted during the optimization process based on the following rules:

$$V_i^{P+1} = \omega * V_i^P + C_1 * rand() * (P_{bi}^{KP} - P_i^{KP}) + C_2 * rand() * (P_{gi}^{KP} - P_i^{KP}) \quad (38)$$

$$P_i^{KP} = P_i^{KP} + V_i^{P+1} \quad (39)$$

where V_{t+1} is the updated particle velocity in the next iteration, V_t is the particle velocity in the current iteration, ω is the inertia dampener which indicates the impact of the particle's own experience on its next movement, $C_1 * rand$ represents a uniformly distributed number within the interval [0, *c*1], which reflects how the neighbours of the particle affects its flight, P_{bi}^{KP} is the neighbourhood best position, V_i^P is the current position of the particle and $C_2 * rand$ represents a uniformly distributed number within the interval [0, *c*2], which indicates how the particle trusts the global best position, P_{gi}^{KP} is the global best position, and V_i^{P+1} is the updated position of the particle. Under the guidance of these two updating rules, the particles will be attracted to move towards the best position found thus far. That is, the optimal solutions can be sought out due to this driving force.

The major steps involved in Particle Swarm Optimization approach are discussed below:

1) Initialization

The initial particles are selected randomly and the velocities of each particle are also selected randomly. The size of the swarm will be (Np x n), where Np is the total number of particles in the swarm and 'n' is the number of stages.

2) Updating the Velocity

The velocity is updated by considering the current velocity of the particles, the best fitness function value among the particles in the swarm. The velocity of each particle is modified by using Equation (28)

The value of the weighting factor ω is modified by following Equation (40) to enable quick convergence.

$$\omega = \omega_{\max} - (\omega_{\max} - \omega_{\min}) / iter_{\max} * iter \tag{40}$$

The term $\omega < 1$ is known as the "inertia weight" and it is a friction factor chosen between 0 and 1 in order to determine to what extent the particle remains along its original course unaffected by the pull of the other two terms. It is very important to prevent oscillations around the optimal value.

3) Updating the Position

The position of each particle is updated by adding the updated velocity with current position of the individual in the swarm

4.1. Algorithm of Particle Swarm Optimization

The step by step procedure to compute the global optimal solution is followed.

Step (1): Initialize a population of particles with random positions and velocities on d dimensions in the problem space.

Step (2): For each particle, evaluate the desired optimization fitness function in the variables.

Step (3): compare particles fitness evolution with particles $Pbest$. If current value is better then $Pbest$, then set $Pbest$ value equal to the current value, and the $Pbest$ location equal to the current location in the dimensional space.

Step (4): Compare fitness evaluation with the populations overall previous $Pbest$. If current value is better than $gbest$, then reset to the current particles array index and value.

Step (5): Change the velocity and position of the particle according to Equations (38) and (39) respectively.

Step (6): Loop to step 2 until a criterion is met, usually a sufficiently good fitness or a maximum number of iterations.

4.2. Implementation of Particle Swarm Optimization Algorithm for Multi-Area Unit Commitment

The various steps of the PSO algorithm are given below for solving multi area unit commitment problem:

Step (1): Read in unit data, tie-line data, load demand profile.

Step (2): Perform the dynamic programming to get the initial commitment schedule for each area.

Step (3): Initialization of particle .The initial particle of size Np is generated randomly for committed unit in each area :

1) Calculate the initial particle population

$$I_p = [(P_1^{kp} .....P_2^{kp}); k = 1, 2, 3, 4 : p = 1.....N_p \tag{41}$$

2) Calculate the fuel cost for each particle using Equation (1)

$$FC_p^k = [(a(P_1^{kp})^2 + b(P_1^{kp}) + c); k = 1, 2, 3, 4; p = 1, 2...N_p \tag{42}$$

3) Calculate start up cost of each particle using Equation (4)

4) Calculate the production cost Production

$$\text{Cost} = \mathrm{FC}_{\mathrm{p}}^{\mathrm{k}} + SC_p^k \tag{43}$$

5) Calculate the fitness function for each particle of population

$$F_p = \mathrm{FC}_{\mathrm{p}}^{\mathrm{k}} + SC_p^k + k(\sum_{i=1}^{N_k} P_i^{kp} - D_j^k) \tag{44}$$

6) To calculate the $Pbest$ by using fitness function values, If current value is better then previous $Pbest$,then set $Pbest$ value equal to the current value and compute $gbest$ if current value is.

Step (4): Updating the Velocity

The velocity is updated by considering the current velocity of the particles, the best fitness function value among the particles in the swarm using following Equation (45).

$$V_i^{P+1} = \omega * V_i^P + C_1 * rand() * (P_{bi}^{KP} - P_i^{KP}) + C_2 * rand() * (P_{gi}^{KP} - P_i^{KP}) \tag{45}$$

where ω is weight factor, The weight ω is computed using Equation (40)

Step (5): Updating the particle position

The position of each particle is updated by adding the updated velocity with current position of the individual in the swarm.

$$P_i^{KP} = P_i^{KP} + V_i^{P+1} \tag{46}$$

The steps described in sub Sections 3 to 5 are repeated until a criterion is met, usually a sufficiently good fitness the maximum generation count is reached. Step (6): Optimum generation schedule is obtained for four area using gbest particle. Check area generation with local demand.

Step (7): Areas with lower fuel cost may export the excessive generation to areas with higher fuel cost (deficiency areas) with tie line limit

5. Test System and Simulation Results

The proposed MAUC algorithm has been implemented in C++ environment and tested extensively. Test results of a multi-area system are presented in this section. All simulations are performed in a PC with Intel processor (1.953 GHz) and 1012 MB of RAM.

As shown in Figure 2, a sample multi-area system with four areas, IEEE reliability test system, 1996 data in [9], are used to test the speed of solving the multi-area UC and ED for a large-scale system with import/export capability and tie line capacity constraints. In the sample multi-area system, each area consists of 26 units. The total number of units tested is 104, and their characteristics are presented in [9]. There are some identical thermal units also located in each area. The system contains five tie lines four area interconnections as shown in Figure 4, and area one is the reference area. Figure 3 shows the modified same load demand profile forecast used in all four areas. The assumptions described in tie line capacity constraint are applied to the simulations.

The four areas have the same load demand profiles. As the 1oad demand is same in these four areas, the economical area will generate more power than expensive areas. Figure 3 gives the changes in area 1 power generation, committed unit capacities, unit commitment pattern of hour 7am and spinning reserve requirement of area 1 is 400MW, because the available unit capacities are not more than the power generation plus the spinning reserve. This phenomenon proves that the available capacity should comply with the area power generation instead of the local load demand.

The systems 1oad demand is 6800 MW, so area 1 generation increases steadily while that of area 2, 3 decreases. The incremental cost of area 2, 3 is higher than

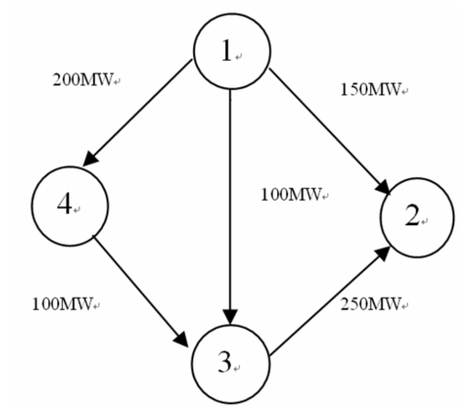

Figure 2. Topological connections of four areas.

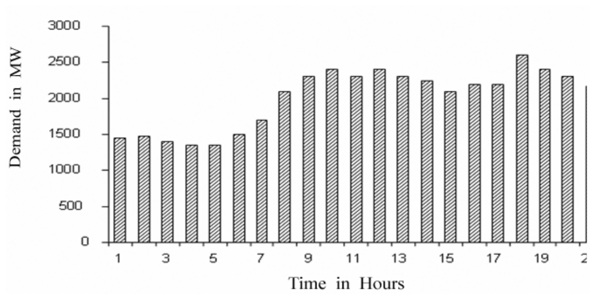

Figure 3. Load pattern for all four –area.

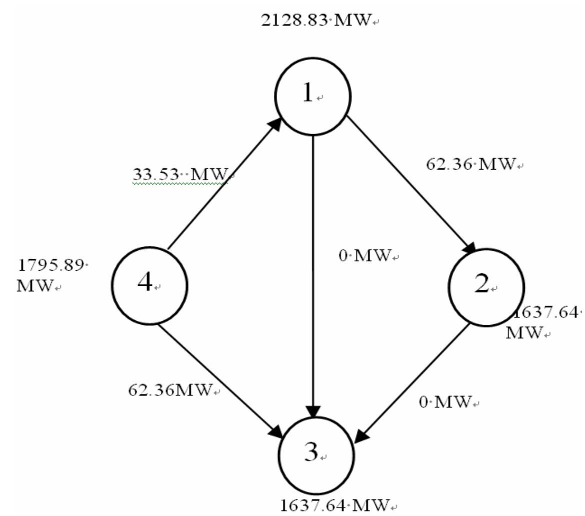

Figure 4.Tie-line flow pattern for 7am.

that of the other two areas since the tie flows to area 2, 3 are at their maximum capacities. This manifests that the proposed method considers tie-line limits effectively.

Table I shows that parameter used in EP and PSO method. Table 2, 3, 4 and Table V shows comparison result of DP and EP, PSO. Figure 4 and 5 shows the convergence characteristics for multi-area obtained using proposed methodology.

Table 2 shows that the total production cost is obta-

Table 1. Parameter used in EP & PSO.

Parameter	EP	PSO
Population size(p)	10	10
Mutation scaling factor(β)	0.03	-
Penalty factor(k1)	10000	10000
Maximum Generation	500	500
Learning factor(c1,c2)	-	2

Table 2. Operating cost of DP method.

Hours (24)	Area-1 (26 Unit)	Area-2 (26 Unit)	Area-3 (26 Unit)	Area-4 (26 Unit)
1	37115.33008	24115.52148	28331.22656	22042.12500
2	24747.96094	23137.63965	22994.89974	19289.81836
3	27995.10742	23137.63965	23701.25684	19175.97998
4	29576.86719	18274.32617	26151.83789	18397.77637
5	29347.66016	18329.32617	25595.42969	18698.77344
6	36118.03711	18329.32617	23799.50977	19705.58106
7	40483.16211	28104.14453	21999.59863	24891.27832
8	39248.85547	32917.46875	19852.85547	21117.69727
9	38728.73438	34865.23828	18245.37305	21253.34180
10	37215.33984	32205.37500	22093.59570	24255.43945
11	37193.46875	32205.37500	20244.08203	23298.57031
12	38310.47266	32205.37500	20992.89258	21298.69336
13	33225.35352	34149.02930	18152.82227	26442.17773
14	31623.27930	37085.82813	17146.93945	25955.68945
15	30595.62695	33172.86133	17991.47266	23682.43359
16	36312.25000	32989.65234	22492.57813	25305.94336
17	36925.17578	32989.65234	23769.58008	25383.72656
18	35682.32031	39459.62500	27589.75977	19501.75391
19	35682.32031	39903.05859	23860.84180	22304.66016
20	35682.32031	32114.94141	21973.39063	15999.40332
21	38042.47852	29387.71680	19907.53906	20248.24805
22	30190.89648	15095.17188	21115.43164	21807.76953
23	30923.70898	18398.08203	19966.21289	22309.07813
24	30202.21094	15198.78125	19815.61328	18294.49805
Total cost	821168.9375	677771.1563	527784.7312	520660.4566

ined by using conventional method. Table 3 and 4 shows that the total production cost is obtained for ten iterations by using EP and PSO method. Figure 4 gives the plot of EP average performance from 500 runs. Figure 5 gives the plot of number of iteration versus the time taken to complete those iterations and the maximum production cost obtained under each iteration using PSO method.

As we indicated in the paper, the PSO algorithm has also proved to be an efficient tool for solving the multi –area unit commitment with economic dispatch problem. There is no obvious limitation on the size of the problem that must be addressed, for its data structure is such that the search space is reduced to a minimum; no “relaxation of constraints” is required; instead, populations of feasible solutions are produced at each generation and throughout the evolution process. The main advantages of the proposed algorithm are speed.

The proposed PSO approach was compared to the related methods in the references indented to serve this purpose, such as the DP with a zoom feature, and the EP approaches. In addition, with the use of PSO method, the status is improved by avoiding the entrapment in local minima. By means of stochastically searching multiple points at one time and considering trial solutions of successive generations, the PSO approach gives global minima instead of entrapping in local optimum solutions. The PSO method obviously displays a satisfactory performance with respect to the quality of its evolved solutions and to its computational requirements.

The final result of PSO would save 0.12% $2865.4 is compared with the solution obtained by the conventional method but it would require 33 seconds to complete the computation .So, the EP method is reduced the operating cost by 0.08 % than the conventional method but it requires 36 seconds to complete this computation .From these results, the PSO method had less total cost and consumed also less CPU time compared to other method.

6. Conclusions

Application of PSO is a novel approach in solving the MAUC problem. Results demonstrate that PSO is a very competent method to solve the MAUC problem. PSO generates better solutions than the other methods, mainly because of its intrinsic nature of updates of positions and velocities. The reason is due to the hourly basis solution. This is somehow similar to the “divide and conquer” strategy of solving a problem. Owning to this

Table 3. Opearting cost of EP method.

Hour-s (24)	Area-1 (26 Unit)	Area-2 (26 Unit)	Area-3 (26 Unit)	Area-4 (26 Unit)
1	37112.33008	24093.52148	28311.22656	22002.12500
2	24741.96094	23127.63965	22964.89974	19259.81836
3	27988.10742	23127.63965	23681.25684	19151.97998
4	29566.86719	18254.32617	26121.83789	18367.77637
5	29337.66016	18309.32617	25572.42969	18678.77344
6	36108.03711	18309.32617	23789.50977	19683.58106
7	40473.16211	28084.14453	21975.59863	24861.27832
8	39238.85547	32897.46875	19822.85547	21087.69727
9	38718.73438	34841.23828	18215.37305	21223.34180
10	37202.33984	32185.37500	22063.59570	24205.43945
11	37183.46875	32185.37500	20224.08203	23278.57031
12	38296.47266	32185.37500	20972.89258	21268.69336
13	33212.35352	34129.02930	18132.82227	26412.17773
14	31607.27930	37063.82813	17126.93945	25920.68945
15	30578.62695	33152.86133	17981.47266	23642.43359
16	36281.25000	32969.65234	22462.57813	25286.94336
17	36919.17578	32969.65234	23749.58008	25353.72656
18	35662.32031	39439.62500	27569.75977	19471.75391
19	35662.32031	39893.05859	23839.84180	22274.66016
20	35662.32031	32094.94141	21943.39063	15969.40332
21	38032.47852	29365.7168	19887.53906	20218.24805
22	30177.89648	15065.17188	21073.43164	21797.76953
23	30913.70898	18387.08203	19946.21289	22279.07813
24	30182.21094	15168.78125	19796.61328	18254.49805
Total cost	820859.9375	677300.1562	527225.7396	519950.4565

Table 4. Operating cost of PSO method.

Hours (24)	Area-1 (26 Unit)	Area-2 (26 Unit)	Area-3 (26 Unit)	Area-4 (26 Unit)
1	37096.33008	24048.52148	28309.22656	21998.12500
2	24514.96094	23004.63965	22910.89974	19251.81836
3	27980.10742	23004.63965	23674.25684	19145.97998
4	29568.86719	18286.32617	26111.83789	18374.77637
5	29387.66016	18286.32617	25578.42969	18671.77344
6	35838.03711	18286.32617	23769.50977	19673.58106
7	40497.16211	28043.14453	21945.59863	24858.27832
8	39228.85547	32977.46875	19815.85547	21081.69727
9	38648.73438	34802.23828	18245.37305	21201.34180
10	37229.33984	32191.37500	22063.59570	24199.43945
11	37184.46875	32191.37500	20212.08203	23272.57031
12	38294.47266	32191.37500	20979.89258	21262.69336
13	33200.35352	34120.0293	18127.82227	26401.17773
14	31630.27930	37051.82813	17124.93945	25928.68945
15	30578.62695	33162.86133	17978.47266	23631.43359
16	36281.25000	32960.65234	22459.57813	25277.94336
17	36949.17578	32960.65234	23748.58008	25365.72656
18	35766.32031	39439.62500	27569.75977	19465.75391
19	35766.32031	39811.05859	23839.8418	22243.66016
20	35766.32031	32081.94141	21943.39063	15968.40332
21	38122.47852	29353.71680	19897.53906	20208.24805
22	30177.89648	15065.17188	21073.43164	21791.76953
23	31583.70898	18379.08203	19966.21289	22270.07813
24	29449.21094	15159.78125	19816.61328	18211.49805
Total cost	820740.9375	676860.1562	527162.7396	519756.4565

hourly solution, the complexity of the search is greatly reduced. The total objective function is the sum of objectives and constraints, which are fuel cost, start-up cost, spinning reserve, power demand, tie-line limit, and import and export constraints. For a better solution, generated powers by N unit of generators and K areas, tie –line limits are constantly checked so that feasible particles can meet the power demand .This reduces the pressure of

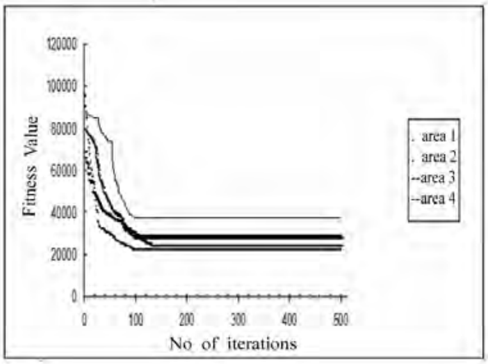

Figure 4. Convergence characteristics of EP method.

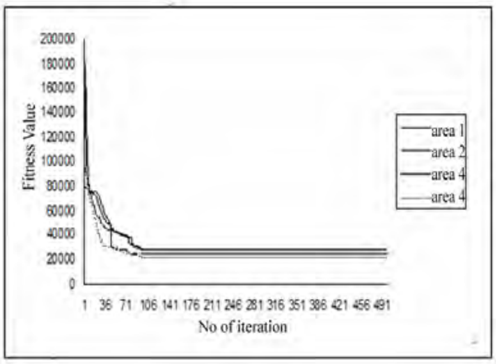

Figure 5. Convergence characteristics of PSO method.

Table 5. Comparison of DP, EP, PSO method.

Method	Area-1 (26)	Area-2 (26)	Area-3 (26)	Area-4 (26)	Total Cost ($)	Time (S)
DP	821168.9	677771.1	527784.7	520660.45	2547385.2	36.7
EP	820859.7	677300.1	527225.9	519950.19	2545336.2	35.1
PSO	820740.9	676860.1	527162.7	519756.45	2544519.3	34.2

the constraint violation of the total objective function. Finally, the result obtained from the simulation is most encouraging in comparison to the best-known solution so far. In the future work, the power flow in each area can be considered to further increase the system security. Other issues such as transmission losses, transmission costs, call and put options policies between and bilateral contract areas can also be considered to reflect more realistic situations in MAUC problems.

7. References

[1] S. Salam, "Unit commitment solution methods," Proceedings of World Academy of Science, Engineering and Technology, Vol. 26, December 2007.

[2] B. Lu and M. shahidehpour, "Short term scheduling of combined cycle units," IEEE Transaction on Power System, Vol. 19, pp. 1616–1625, August 2004.

[3] F. Gao, "Economic dispatch algorithms for thermal unit system involving combined cycle units," IEEE and Gerald Bushel IEEE Lowa State University Ames, IA, USA, IEEE Transaction on Power Systems, pp. 1066–1072, November 2003.

[4] E. Fan, X. H. Guan, and Q. Z. Zhai, "A new method for unit commitment with ramping con straints," IEEE Transaction on Power Systems, March 2001.

[5] H. T. Yang and C. L. Huang, "Evolutionary programming based economic dispatch for units with non-smooth fuel cost functions," IEEE Transactions on power system, Vol. 11, No. 2, pp. 112–118, 1996.

[6] Z. Ouyang and S. M. Shahidehpour, "Heuristic multi-area unit commitment with economic dispatch," IEEE Proceedings, Vol. 138, No. 3, pp. 242–252, 1991.

[7] C. L. Tseng, "Multi-area unit commitment for large scale power system," IEEE Proceedings - Generation and Distribution, Vol. 145, No. 41, pp. 415–421, 1999.

[8] C. Wang and M. Shahidehpour, "A decomposition approach to non-linear multi-area generation scheduling with tie-line constraints using expert systems," IEEE Transactions on Power System, Vol. 7, No. 4, pp. 1409 –1418, 1992.

[9] C. K. Pang, G. B. Sheble, and F. Albuyeh, "Evaluation of dynamic programming based methods and multiple area representation for thermal unit commitments," IEEE Transactions on Power Apparatus System, Vol. 100, No. 3, pp. 1212–1218, 1981.

[10] F. N. Lee, J. Huang, and R. Adapa, "Multi-area unit commitment via sequential method and a DC power flow network model," IEEE Transactions on Power System, Vol. 9, No. 1, pp. 279– 284, 1994.

[11] C. Yingvivatanapong, W. J. Lee, and E. Liu, "Multi-area power generation dispatch in competitive markets," IEEE Transactions on Power Systems, pp. 196–203, 2008.

[12] U. B. Fogel, "On the philosophical differences between evolutionary algorithms and genetic algorithms," IEEE Proceedindings in Second Annual Conference on Evolutionary Programming, pp. 23–29, 1993.

[13] T. Biick and H. P. Schwefel, "An overview of evolutionary algorithm for parameter optimization," Evolutionary Computation, Vol. 1, No. 1, pp. 1–24. 1993.

[14] C. C. Asir Rajan and M. R. Mohan, "An evolutionary programming-based tabu search method for solving the unit commitment problem," IEEE Transactions on Power System, Vol. 19, No. 1, pp. 577–585, 2004.

[15] D. Srinivasan, F. Wen, and C. S. Chang, "A survey of applications evolutionary computing to power systems," IEEE Proceedings, USA, pp. 35–41, 1996.

[16] J. Kennedy, "The particle swarm: Social adaptation of knowledge," Proceedings in International Conference on Evolutionary Computation, Indianapolis, pp. 303–308, 1997.

Appendix A

Nomenclature

D_j^k	Total load demand in area k at jth hour
L_j^k	Total import power to area k at jth hour
E_j^k	Total export power to area k at jth hour
$I_{i,j}^k$	Commitment state (1 on, 0 for off)
$Irlist$	List of committed units ascending priority order
i	Index for units
j	Index for time
λ_i	Lagrangian multiplier for unit
λ_{sys}	Lagrangian multiplier for entire system
N_A	Total number of areas
N_k	Total number of units in area K
O_{plist}	List of uncommitted units in descending order
Pg_j^k	Power generation of area k at jth hour
$\underline{Pg_i^k}$	Lower limit of power generation of unit i in area k
$\overline{Pg_i^k}$	Upper limit of power generation of unit i in area k
$Pg_{i,j}^k$	Power generation of unit i in area k at j th hour
R_j^k	Spinning reserve of area k at j th hour
S_j^k	Total commitment capacity for area k at j th hour
SD_j^k	Total system demand at j th hour t Total time span in hours
T_i^{on}	Minimum up time of unit i
T_i^{off}	Minimum down time of unit i
τ_i	Time constant in start up cost function for unit i
W_j	Net power exchange with outside systems
$X_{i,j}^{on/off}$	Time duration for which unit i has been on/off at j^{th} hour

Engineering, **2009, 1, 151-160**
doi:10.4236/eng.2009.13018 Published Online November 2009 (http://www.scirp.org/journal/eng).

Heat Distribution in Rectangular Fins Using Efficient Finite Element and Differential Quadrature Methods

ShahNor BASRI, M. M. FAKIR, F. MUSTAPHA, D. L. A. MAJID, A. A. JAAFAR
Department of Aerospace Engineering, University Putra Malaysia, Putra, Malaysia
E-mail: *shahnor@eng.upm.edu*
Received September 2, 2009; *revised September* 24, 2009; *accepted September* 28, 2009

Abstract

Finite element method (FEM) and differential quadrature method (DQM) are among important numerical techniques used in engineering analyses. Usually elements are sub-divided uniformly in FEM (conventional FEM, CFEM) to obtain temperature distribution behavior in a fin or plate. Hence, extra computational complexity is needed to obtain a fair solution with required accuracy. In this paper, non-uniform sub-elements are considered for FEM (efficient FEM, EFEM) solution to reduce the computational complexity. Then this EFEM is applied for the solution of one-dimensional heat transfer problem in a rectangular thin fin. The obtained results are compared with CFEM and efficient DQM (EDQM), with non-uniform mesh generation). It is found that the EFEM exhibit more accurate results than CFEM and EDQM showing its potentiality.

Keywords: Efficient Finite Element Method, Efficient Differential Quadrature Method, Heat Transfer Problem

1. Introduction

Presently there are many numerical solution techniques known to the computational mechanics community. FEM is one of those numerical solution techniques to solve structural, mechanical, heat transfer, and fluid dynamics which arise in problems of engineering and physical sciences [1–5]. Here, conventional FEM (CFEM) means the used elements are of same size and uniformly distributed. In its application to the solution of engineering problems, the finite element discretization has been implemented almost to the spatial problems. For dynamic or time dependent problems whose solutions as functions of time are of interest, a step by step procedure of finite difference is usually employed with computational complexity.

For heat transfer problems, rapid changes of heat/temperature distributions take place near the element boundary (and at the boundary). It is very important to know these temperature change behavior of an element prior to its use. Hence, to get an actual picture using FEM, the element is usually subdivided into very small sub-elements uniformly (conventional FEM, CFEM), which leads to huge amount of complexity, memory consumption and computational time [6]. Otherwise, error flow occurs with unreliable results [1,2,6].

On the other hand, to get a clear picture about the temperature changes near (and at) the element boundary, better to subdivide the elements into very small sub-elements at the boundary only, followed by relatively bigger elements gradually towards the mid-point of the element non-uniformly (efficient FEM, EFEM). This may serve the intended purpose without any additional burden and this is highlighted in this paper with improved accuracy (approximately 65%) compared to CFEM. Hence, here, focus is given to develop and apply efficient (non-uniform mesh density) nodal points distribution algorithm for automatic mesh (elements) generation to optimize CFEM solution.

DQM is another numerical solution technique to solve above mentioned problems efficiently [7–13]. The essence of the DQM is that the partial derivative of a function is approximated by a weighted linear sum of the function values at given discrete points. Bellman and Casti [7,8] developed this numerical solution technique in the early 1970s and since then, the technique has been successfully employed in a variety of problems in engineering and physical sciences. To make the DQM more efficient with less computational complexity, efficient DQM (EDQM) was proposed in [11–13] with non-uniformly distributed mesh points.

Hence, in this paper, one-dimensional (1-D) heat conduction problems in a thin rectangular fin are solved using EFEM by means of the accurate discretization and solver (code) and then the results are compared with

CFEM and EDQM to verify EFEM efficiency.

The paper is organized as follows. Section II presents the governing equation with efficient FEM rules, followed by simulation set-up and assumptions, results and discussions, and finally conclusion of the paper.

2. The One-Dimensional Efficient Finite Element Method

Here, the considered one dimensional (1-D) heat conduction problem is [2,3,14–18]

$$\frac{d}{dx}\left(k\frac{dT}{dx}\right)+Q=0 \quad (1)$$

with the boundary conditions $T\big|_{x=0}=T_0$ and $q\big|_{x=L}=h(T_L-T_\infty)$ as shown in Figure 1. Here, heat flux $q=-k\frac{dt}{dx}$. Figure 1 shows the 1-D element discretization in the x-direction. The temperature T at various nodal points are the unknowns except at node 1, where, $T_1=T_0$ with initial temperature T_0. Within a typical element '*ei or e*' the local node numbers are i and $i+1$ with coordinates x_i and x_{i+1} and element length, $l_{ei}=x_{i+1}-x_i$. For example, $e1$ whose local node numbers are 1.and 2 with coordinates x_1 and x_2, and element length $l_{e1}=x_2-x_1$ respectively.

An one-dimensional thin rectangular fin as shown in Figure 2 is considered here. Heat is transmitted along its length by conduction and dissipated from its lateral surfaces to the surroundings by convection. The governing equation for the temperature in the fin is given in Equation (1).

The parameter, M is given by $M^2=\frac{hp}{kA_C}$, where, p is the fin perimeter (meter) and Ac is the cross sectional area of the fin [meter^2]. Fin length, width and thickness are L, w and t respectively.

In this case, $q=h(T-T_\infty)=-k\frac{dT}{dx}$, $p=2(w+t)$, $A_C=w\times t$ and $\frac{p}{A_C}=\frac{2(w+t)}{w\times t}\approx\frac{2}{t}$. The convection heat loss in the fin is equivalent to negative heat source and can be expressed as follows:

$$Q=-\frac{(p\,dx)h(T-T_\infty)}{A_C dx}=-\frac{ph}{A_C}(T-T_\infty)$$

Now Equation (1) becomes

$$\frac{d}{dx}\left(k\frac{dT}{dx}\right)-\frac{ph}{A_C}(T-T_\infty)=0 \quad (2)$$

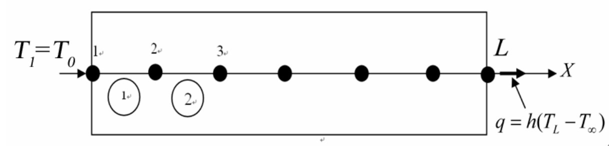

Figure 1. Boundary conditions for 1-D heat conduction.

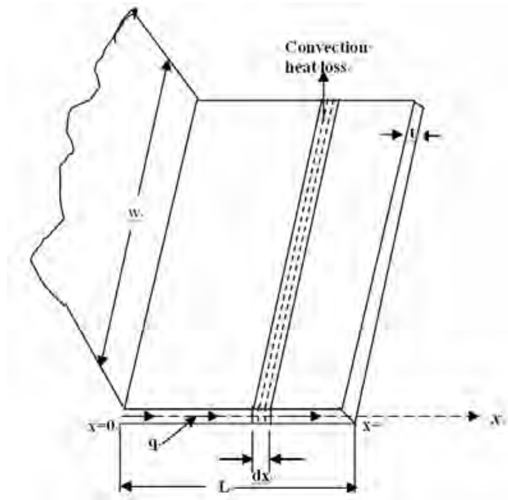

Figure 2. Thin rectangular fin.

To calculate the approximate solution *T*, the mathematical formulation using Galerkin's approach [2,3] is

$$\int_0^L \varphi\left[\frac{d}{dx}\left(k\frac{dT}{dx}-\frac{ph}{A_C}(T-T_\infty)\right)\right]dx=0 \quad (3)$$

where φ is a test function constructed from the same basis functions as those of *T*, with $\varphi(0)=0$.

Integrating by parts Equation (3) becomes,

$$\varphi k\frac{dT}{dx}\bigg|_0^L-\int_0^L k\frac{d\varphi}{dx}\frac{dT}{dx}dx-\int_0^L\varphi\frac{ph}{A_C}(T-T_\infty)dx=0 \quad (4)$$

The 1st term of Equation (4) is,

$$\varphi k\frac{dT}{dx}\bigg|_0^L=\varphi(L)k(L)\frac{dT}{dx}(L)-\varphi(0)k(0)\frac{dT}{dx}(0) \quad (5)$$

Since $\varphi(0)=0$ and $q=-k(L)\frac{dT}{dx}(L)=h(T_L-T_\infty)$, we get, $\varphi k\frac{dT}{dx}\bigg|_0^L=-\varphi(L)h(T_L-T_\infty)$

Equation (4) becomes

$$-\varphi(L)h(T_L-T_\infty)-\int_0^L k\frac{d\varphi}{dx}\frac{dT}{dx}dx-\int_0^L\varphi\frac{ph}{A_C}(T-T_\infty)dx=0 \quad (6)$$

A global virtual temperature vector is defined as $\psi=[\psi_1,\psi_2,\psi_3,...,\psi_L]^T$ then within each element, th test function becomes

$$\varphi(i) = N_i \psi_i \tag{7}$$

Here, N is the element shape function and $N_L = 1$ at the element boundary [2] (Figure 1). Therefore Equation (7) gives

$$\varphi(L) = [N\psi]_L = \psi_L \tag{8}$$

According to Reference [2], $\frac{dT}{dx} = \mathbf{B}_T \mathbf{T}^e$, we have $\frac{d\varphi}{dx} = \mathbf{B}_T \psi$

For matrix multiplication validity, we have $\left(\frac{d\varphi}{dx}\right)^T \times \left(\frac{dT}{dx}\right) = \left(\mathbf{B}_T^T \boldsymbol{\psi}^T\right)\left(\mathbf{B_T T}^{ei}\right)$ and

$$\mathbf{B}_T^{\mathbf{T}}\mathbf{B}_T = \frac{1}{x_{i+1} - x_i}\begin{bmatrix} -1 \\ 1 \end{bmatrix} \times \frac{1}{x_{i+1} - x_i}\begin{bmatrix} -1 & 1 \end{bmatrix} = \frac{1}{(x_{i+1} - x_i)^2}\begin{bmatrix} 1 & -1 \\ -1 & 1 \end{bmatrix} = \frac{1}{(l_{ei})^2}\begin{bmatrix} 1 & -1 \\ -1 & 1 \end{bmatrix}$$

The element conductivity matrix is

$$k_T = \frac{k_{ei}\, l_{ei}}{2}\int_{-1}^{1} \mathbf{B}_T^{\mathbf{T}}\mathbf{B}_T\, d\xi = \frac{k_{ei}}{l_{ei}}\begin{bmatrix} 1 & -1 \\ -1 & 1 \end{bmatrix} \tag{9}$$

where, ξ varies from -1 to $+1$ and $\xi = \frac{2}{x_{i+1} - x_i}(x - x_i) - 1 \quad with\ d\xi = \frac{2}{x_{i+1} - x_i}dx$.

The element heat rate vector due to the heat source is

$$\mathbf{R} = \mathbf{r}_Q = \frac{Q_{ei}\, l_{ei}}{2}\int_{-1}^{1} \mathbf{N}^{\mathbf{T}} d\xi = \frac{Q_{ei} l_{ei}}{2}\begin{bmatrix} 1 \\ 1 \end{bmatrix} \tag{10}$$

Now, Equation (2) can be transformed into

$$-\psi_l h(T_L - T_\infty) - \sum_{ei} \boldsymbol{\psi}^{\mathbf{T}}\left(\frac{k_{ei}\, l_{ei}}{2}\int_{-1}^{1} \mathbf{B}_T^{\mathbf{T}}\mathbf{B}_T\, d\xi\right)\mathbf{T}^e + \sum_{ei} \boldsymbol{\psi}^{\mathbf{T}} \frac{Q_{ei}\, l_{ei}}{2}\int_{-1}^{1} \mathbf{N}^{\mathbf{T}} d\xi = 0 \tag{11}$$

or

$$\boldsymbol{\psi}^{\mathbf{T}}\mathbf{K}_T\mathbf{T} + \psi_L h T_L = \boldsymbol{\psi}^{\mathbf{T}}\mathbf{R} + \psi_L h T_\infty \tag{12}$$

where, global matrices $\mathbf{K}_T$, $\mathbf{R}$, $\boldsymbol{\psi}^{\mathbf{T}}$ and $\mathbf{T}$ are respectively,

$$\mathbf{K}_T = \sum_{ei} \frac{k_{ei}\, l_{ei}}{2}\int_{-1}^{1} \mathbf{B}_T^{\mathbf{T}}\mathbf{B}_T d\xi = \begin{bmatrix} K_{11} & K_{12} & K_{13} & \dots & K_{1L} \\ K_{21} & K_{22} & K_{23} & \dots & K_{2L} \\ K_{31} & K_{32} & K_{33} & \dots & K_{3L} \\ \dots\dots & & & & \\ K_{L1} & K_{L2} & K_{L2} & \dots & K_{LL} \end{bmatrix} \tag{13}$$

$$\mathbf{R} = \sum_{ei} \frac{Q_{ei}\, l_{ei}}{2}\int_{-1}^{1} \mathbf{N}^{\mathbf{T}} d\xi = \begin{bmatrix} R_1 & R_2 & R_3 & \dots & R_L \end{bmatrix}^{\mathbf{T}} \tag{14}$$

$$\boldsymbol{\psi}^{\mathbf{T}} = \begin{bmatrix} 0 & 0 & 0 & \dots 0 & 0 \\ 0 & \psi_2 & 0 & \dots 0 & 0 \\ 0 & 0 & \psi_3 & \dots 0 & 0 \\ \dots\dots & & & & \\ 0 & 0 & 0 & \dots 0 & \psi_L \end{bmatrix} = \begin{bmatrix} 0 & 0 & 0 & \dots 0 & 0 \\ 0 & 1 & 0 & \dots 0 & 0 \\ 0 & 0 & 1 & \dots 0 & 0 \\ \dots\dots & & & & \\ 0 & 0 & 0 & \dots 0 & 1 \end{bmatrix} \tag{15}$$

and $\mathbf{T} = \begin{pmatrix} T_1 & T_2 & T_3 & \dots & T_L \end{pmatrix}^{\mathbf{T}}$ with $T_1 = T_0 =$ constant.

Finally, the global matrix is formed and the Equation (12) becomes

$$\begin{bmatrix} K_{21} & K_{22} & K_{23} & \dots & K_{2L} \\ K_{31} & K_{32} & K_{33} & \dots & K_{3L} \\ K_{41} & K_{42} & K_{43} & \dots & K_{4L} \\ \dots\dots & & & & \\ K_{L1} & K_{L2} & K_{L3} & \dots & K_{LL} + h \end{bmatrix} \times \begin{bmatrix} T_2 \\ T_3 \\ T_4 \\ . \\ T_L \end{bmatrix} = \begin{bmatrix} R_2 \\ R_3 \\ R_4 \\ . \\ R_L + hT_\infty \end{bmatrix} - \begin{bmatrix} K_{21}T_0 \\ K_{31}T_0 \\ K_{41}T_0 \\ . \\ K_{L1}T_0 \end{bmatrix} \tag{16}$$

This equation needs to be solved to obtain the 1-D FEM numerical temperature distribution in the considered rectangular fin.

Using Equations (11-16) and the efficient FEM (EFEM) algorithm, the approximate solution T has been obtained. The 1-D EFEM algorithm (rule) is depicted in terms of self-explanatory flow chart in Figure 3. The non-uniform and uniform mesh distribution scenarios are shown in Figures 4 and 5 respectively.

2.1. Example Problem 1: 1-D Insulated Tip Thin Rectangular Fin

When the base of the fin is held at constant temperature, T_0 and the tip of the fin is insulated, the boundary conditions are then given by

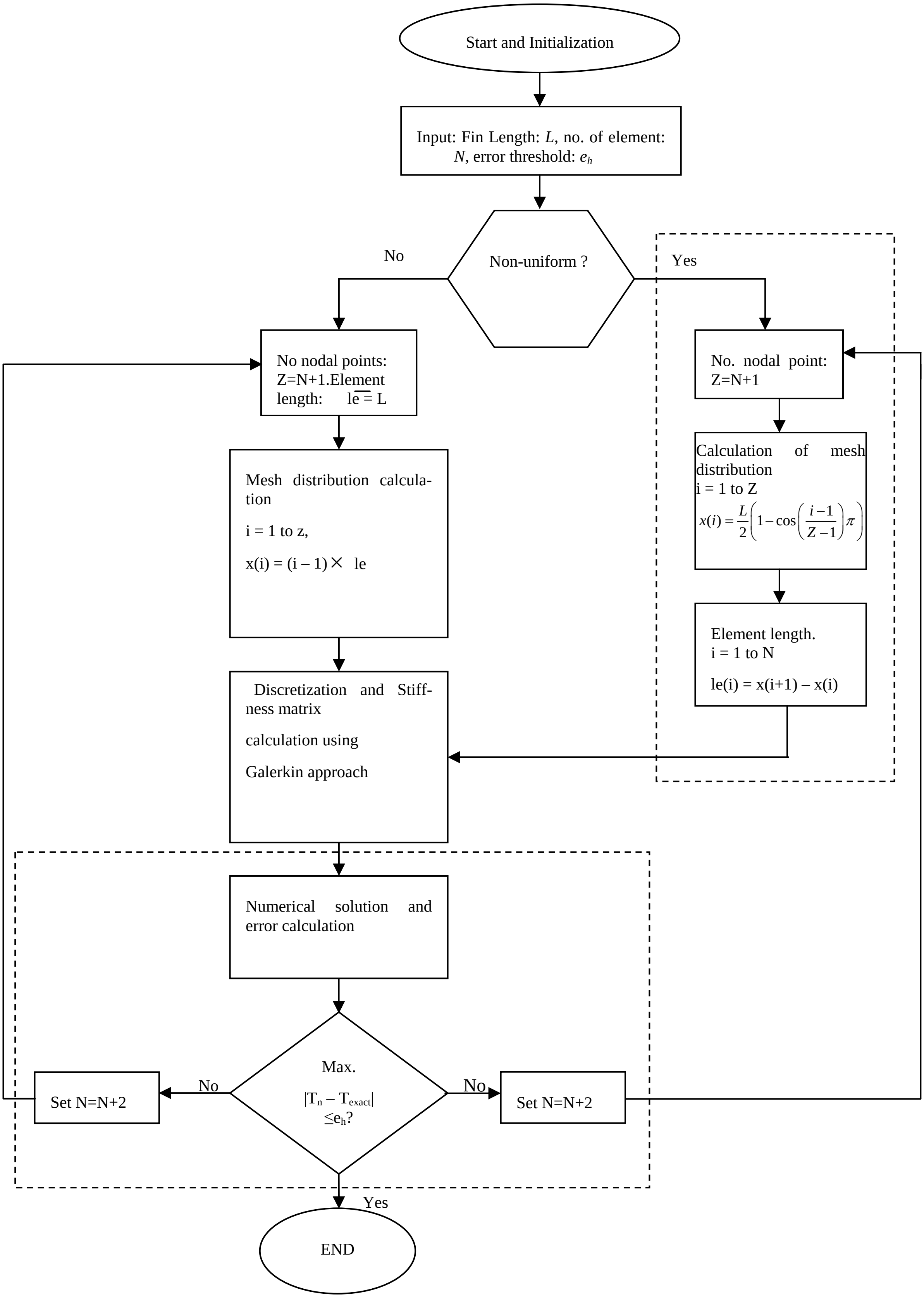

Figure 3. Efficient discretization and solution rule for 1-D FEM

$$T = T_0 \qquad \text{at} \quad x = 0$$

$q = 0$ at $x = L$, where L is the length of the fin.

In this case, the final form of the global matrix in Equation (16) becomes

$$\begin{pmatrix} A_{22} & A_{23} & \ldots\ A_{2L} \\ A_{32} & A_{33} & \ldots\ A_{3L} \\ \ldots & \ldots & \ldots\ \ldots \\ A_{L2} & A_{L3} & \ldots\ A_{LL} \end{pmatrix} \begin{pmatrix} T_2 \\ T_3 \\ \ldots \\ T_L \end{pmatrix} = \begin{pmatrix} R_{2\infty} \\ R_{3\infty} \\ \ldots \\ R_{L\infty} \end{pmatrix} - \begin{pmatrix} A_{21}T_0 \\ A_{31}T_0 \\ \ldots \\ A_{L1}T_0 \end{pmatrix} \quad (17)$$

Example of non-uniform and uniform mesh distributions and element lengths are depicted in Figures 4 and 5 respectively.

2.2. Example Problem 2: 1-D Convection Tip Thin Rectangular Fin

When the base of the fin is held at a constant temperature, T_0 and the tip of the fin is a convection surface, then the boundary conditions are $T=T_0$ at $x=0$

$$q = h\left(T_L - T_\infty\right) \qquad \text{at x=L}$$

And the final global matrix shown in Equation (16) becomes

$$\begin{pmatrix} A_{22} & A_{23} & \ldots\ A_{2L} \\ A_{32} & A_{33} & \ldots\ A_{3L} \\ \ldots & \ldots & \ldots\ \ldots \\ A_{L2} & A_{L3} & \ldots\ A_{LL} + h \end{pmatrix} \begin{pmatrix} T_2 \\ T_3 \\ \ldots \\ T_L \end{pmatrix} = \begin{pmatrix} R_{2\infty} \\ R_{3\infty} \\ \ldots \\ R_{L\infty} + hT_\infty \end{pmatrix} - \begin{pmatrix} A_{21}T_0 \\ A_{31}T_0 \\ \ldots \\ A_{L1}T_0 \end{pmatrix} \quad (18)$$

3. Simulation Set-up and Assumptions

Table 1 shows the considered parameters and their corresponding values used to obtain simulation results using FORTRAN 90 software. We used these values to obtain the temperature distribution for EFEM, CFEM, EDQM and exact methods.

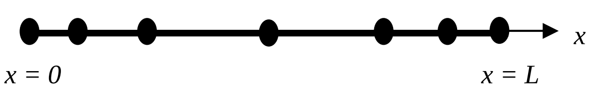

Figure 4: Example 1-D efficient mesh distribution and element lengths.

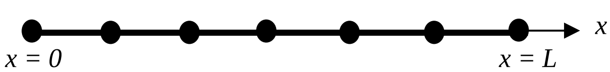

Figure 5. Example 1-D conventional mesh distribution and element lengths.

We considered, $M^2 = \frac{hP}{kA} = 1$ and the associated assumptions (in Table 1) to compare the obtained FEM results with DQM [13] and exact solution [18]. Here to mention that, to obtain 1-D DQM solutions, element material properties, fin-width and fin-thickness are not required (which is the shortcoming of the method). The errors in FEM and DQM solutions are computed compared to exact solution [18].

4. Results and Discussions

4.1. Results and Discussions of 1-D Insulated Tip Thin Rectangular Fin

The results of the present problem, shown in Figure 6, contain the maximum absolute percentage errors in the FEM and DQM solutions obtained with uniformly (conventional) and non-uniformly (efficient) distributed nodal (mesh) points. It is essential to know, how many mesh points (elements) are required to obtain a convergent FEM solution in the solution domain.

Hence, the comparison of convergence of fin-temperature in terms of maximum % error versus number of nodal (mesh) points for CFEM, EFEM and EDQM solutions is shown in Figure 6. Initially, all the solutions in terms of maximum % errors show a monotonic convergence with the increasing number of mesh points (shown $Z = 11$ to 104). It is apparent that EFEM results show bit less accuracy for $Z \le 30$ and similar accuracy for $Z \ge 30$ compared to EDQM, but yields result with higher accuracy, of one order of magnitude or more with increasing Z compared to CFEM. EDQM converge up to $Z = 100$ and then saturated, whereas the EFEM solutions converge smoothly for all N within the solution domain, showing best converging result at $Z = 100$ and 101. On the other hand, uniform FEM (CFEM) results converge slowly throughout the solution domain and then diverge without showing the best results like EFEM. It happens due to the mesh point distribution strategy of equally spaced and unequally spaced nodal points in the computational domain and the inherited complexity to compute the stiffness matrix for equally spaced nodal points. Hence, the efficiency of EFEM results is apparent.

Figure 7 shows the convergent numerical and exact solutions (fin temperature) and the corresponding percentage errors for $N = 100$ elements (FEM case) which is equivalent to $Z = 101$ mesh points (both FEM and DQM cases). These results are obtained at an interval of $\Delta x = 0.1$ along the fin length, $0 \le x \le 1$, using cubic

Table 1. Input parameters and assumptions for 1-d rectangular fin.

Input Parameters	Assumed value for Insulated-Tip Fin	Assumed value for Convection-Tip Fin
Boundary and other values:		
Initial temperature (T_0)	1 ^{O}C	1 ^{O}C
Ambient temperature (T_∞)	0 ^{O}C	0 ^{O}C
Heat flux (q)	0 at x = 1	Variable
% Error threshold (e_h)	0 - 0.1	0 - 0.1
Element Type (NNODE): Linear (for 1-D)	2	2
Element material properties:	Variable to make M = 1	7.03125 $W/(m\ ^{0}C)$
Thermal conductivity ($k_e = k$)	9 $W/m^2\ ^{0}C$	9 $W/m^2\ ^{0}C$
Convective heat transfer coefficient (h)	0 $W/m^3\ ^{0}C$	0 $W/m^3\ ^{0}C$
Heat source (Q)		
Element (Fin) dimension:		
length (L) along x-axis	1 m	1 m
width (w)	Variable to make M = 1	Variable to make M = 1
thickness (t)	0.001 m	Variable to make M = 1
Number of elements (N)	11 - 104	11 - 104

spline interpolation. It is seen that all the solutions are very close to exact solutions throughout the length of the fin with temperature variations $T_0 = 1^0 C$ at $x = 0\,m$ to $T_L = 0.648^0 C$ at $x = 1.0\,m$.

Figure 8 shows the percentage errors at the base of the fin ($x = 0$) are 0 for all solutions due to initial temperature $T_0 = 1^0 C$ (Figure 7). The percentages errors remain the same with EFEM except little bit increase (with maximum error 2.44×10^{-6}) at the middle of the fin due to nodal point distribution with maximum spacing there. Whereas, with CFEM, it increases gradually along the length of the fin with the maximum percentage error 1.9×10^{-4} at the fin-tip (x = 1). In other case, the oscillations (instability) of DQM results appear clearly compared to FEM results. The average percentage error in CFEM, EDQM [13] and EFEM are 1.2×10^{-4}, 2.24×10^{-6} and 1.12×10^{-6} respectively, which shows approximately 99% and 49% improvements in EFEM results demonstrating its superiority over CFEM and EDQM.

4.2. Results and Discussion of 1-D Convection Tip Thin Rectangular Fin

Here the results exhibit the same nature like insulated-tip fin but yield results with higher accuracy, of two order of magnitude or more with increasing Z due to different material properties and fin-thickness (as the FEM solution and its accuracy depend on fin dimension, materials used and associated boundary conditions).

In Figure 9, the comparison of convergence versus number of mesh points of exact, FEM and DQM solutions for convection-tip fin with uniform and non-uniform mesh distributions is shown. It is apparent that for all cases, the solutions converge smoothly for all Z within the solution domain. The comparison shows similar results as in Figure 6 except EFEM yields result with higher accuracy, of one order of magnitude or more with increasing Z (for $Z > 20$) compared to that with CFEM. Here, EFEM results converge from $Z = 80$ showing best result at $Z = 90$ to 101, EDQM [13] shows similar results with some oscillations, whereas CFEM does not exhibit any best convergence.

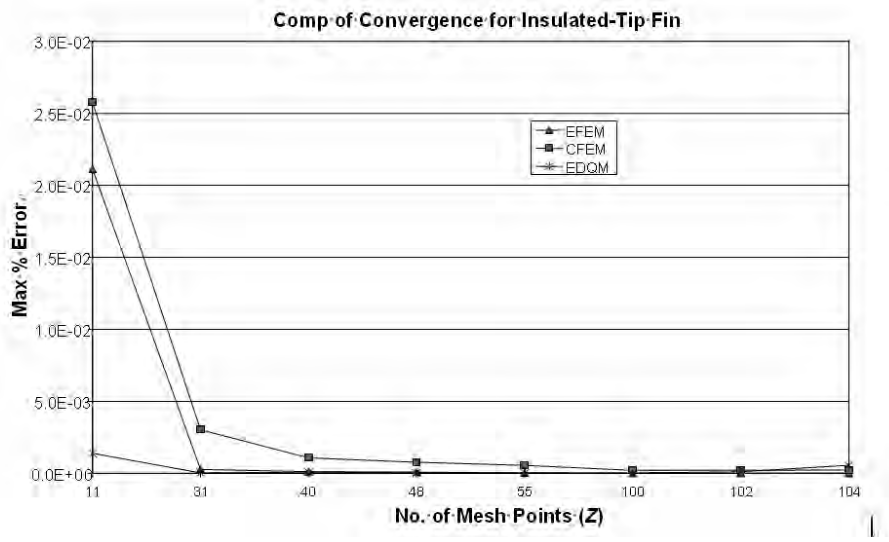

Figure 6. Comparison of convergence of insulated-tip fin-temperature in terms of maximum % error for CFEM, EFEM and EDQM solutions ($Z = 11$ to 104).

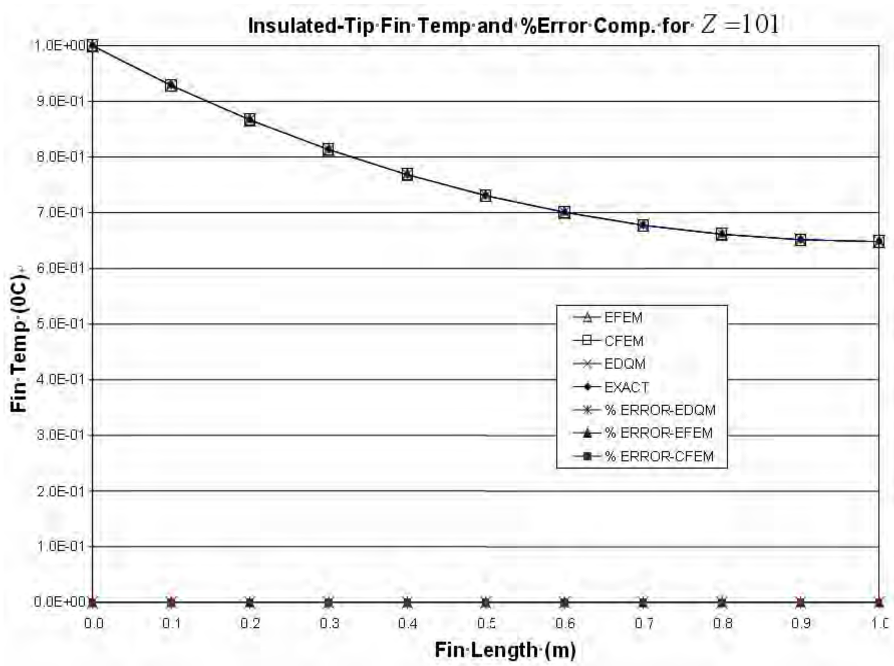

Figure 7. Insulated-tip fin-temperature distribution for exact, EFEM, CFEM and EDQM along with its respective % errors ($Z = 101$).

Figure 10 depict the comparison of CFEM, EFEM, EDQM [13] numerical and exact convection-tip fin temperatures and the corresponding percentage errors for conventional (uniform) and efficient (non-uniform) mesh point distribution respectively for 100 elements (i.e., $Z = 101$). Same as Insulated-tip fin, the results are obtained at an interval of $\Delta x = 0.1$ along the fin length, $0 \le x \le 1$, using cubic spline interpolation. Figure 10 shows that, all numerical solutions are very close to exact solutions throughout the length of the fin with temperature variations $T_0 = 1^0 C$ at base of the fin to $T_L = 0.328^0 C$ at the tip of the fin. Here the reduction of fin temperature is $0.32^0 C$ more compared to insulated-tip fin (Figure 7) as expected.

FEM versus DQM maximum % error comparison for convection-tip fin-temperature are shown in Figure 11. The comparison of CFEM, EFEM and EDQM [13] per-

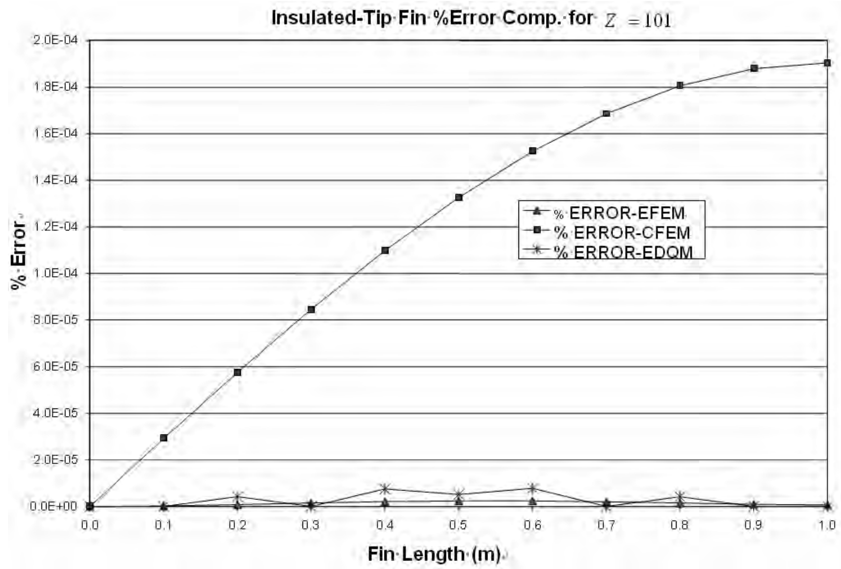

Figure 8. Percentage error comparison of EFEM, EDQM and CFEM for $Z = 101$ along the fin-length.

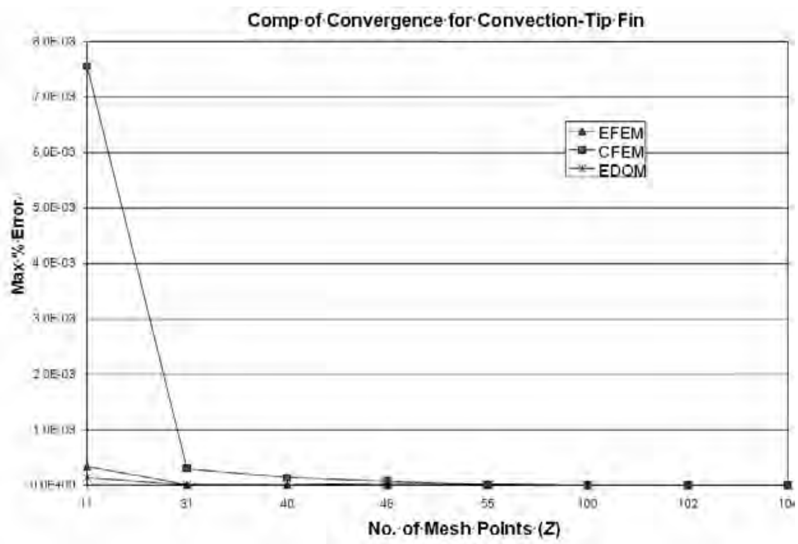

Figure 9. Comparison of convergence of convection-tip fin-temperature in terms of maximum % error for CFEM, EFEM and EDQM solutions ($Z = 11$ to 104).

centage errors for convection-tip fin is shown in Figure 11. There is no error at the base of the fin and it almost remain the same with EFEM and EDQM except negligible increase at the middle of the fin, whereas, with CFEM, it increases gradually along the length of the fin with the maximum percentage error 3.31×10^{-6} at the tip (x = 1). In this case the EDQM converges with oscillations throughout the solution domain. The average % error in CFEM, EDQM [13] and EFEM are 1.69×10^{-6}, 3.08×10^{-9} and 2.24×10^{-11} respectively. This shows nearly 100% and 99% improvements in EFEM results compared to CFEM and EDQM respectively demonstrating its superiority.

5. Conclusions

Here, the solutions of the temperature distribution in insulated-tip and convection-tip 1-D rectangular fin are computed numerically using FEM and the results are found to agree very well with the exact solution and show the efficiency of the method. Investigating the various mesh points distribution for equal and unequal spacing, it is found that, for FEM solution, unequally spaced mesh points distribution give better and more

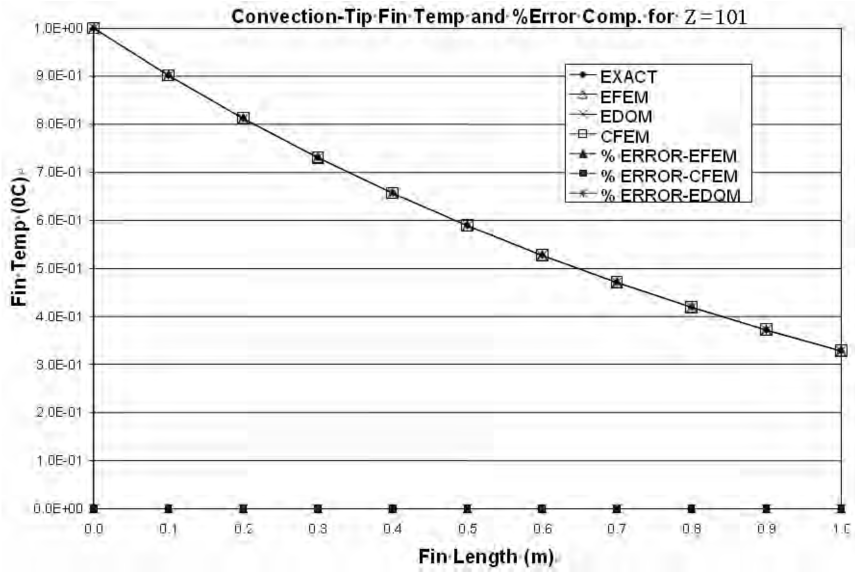

Figure 10. Convection-tip fin-temperature distribution for exact, EFEM, CFEM and EDQM along with its respective % errors ($Z = 101$).

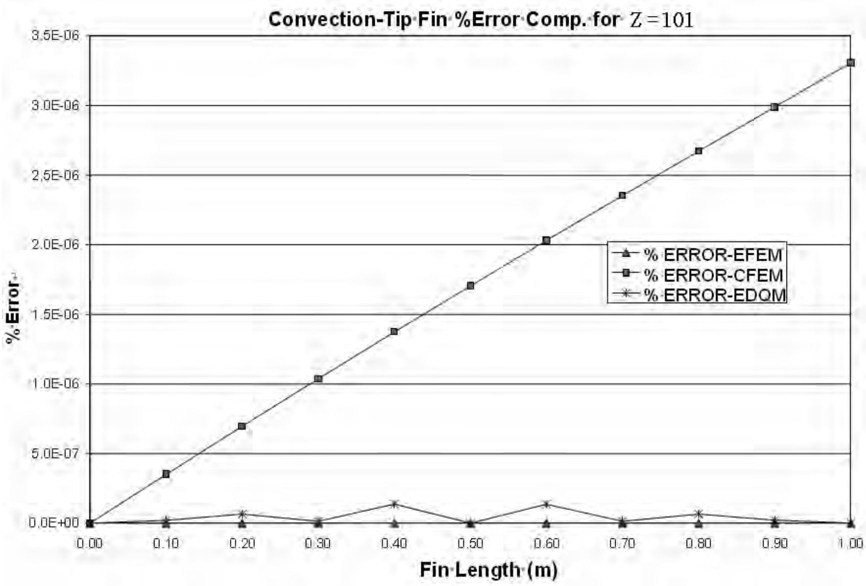

Figure 11. Convection-tip fin error comparison of EFEM, EDQM and CFEM for $Z = 101$ along the fin-length.

accurate results than equally spaced and the solution converges smoothly as the number of nodal points (or elements) is increased. In general, this study has improved the stability and accuracy of EFEM results for practical consideration and implementation.

Finally, the results of EFEM shows remarkable enhancement compared to CFEM and agree very well with EDQM with very small errors or difference showing its potentiality. Hence EFEM is suitable to test the temperature distribution scenario in any thin metal fin prior to its design and practical implementation.

7. References

[1] G. Strang and G. J. Fix, "An analysis of the finite element method," Prentice-Hall, Inc., 1997.

[2] R. Tirupathi and P. E. Chandrupatla, Introduction to finite elements in engineering, Prentice-Hall International, 1997.

[3] "Mathematics of finite element method," 2004, Available at: http://math.nist.gov/mcsd/savg/tutorial/ansys/FEM/ (Accessed on October 19, 2006).

[4] B. Li, "Numerical method for a parabolic stochastic partial differential equation," Chalmers Finite Element Center, 2004.

[5] F. Fairag, "Numerical computations of viscous, incompressible flow problems using a two-level finite element method," arXiv: Math.NA/0109109, Vol. 1, No. 17, September 2001.

[6] S. Park, "Development and applications of finite elements in time domain," PhD Thesis, Faculty of the Virginia Polytechnic Institute and State University, Virginia, December, 1996, Available in the Library, Virginia Polytechnic Institute and State University.

[7] R. Bellman and J. Casti, "Differential quadrature and long-term integration," J Math and Appl., Vol. 34, pp. 235–238, 1971.

[8] R. Bellman and J. Casti, "Differential quadrature: A technique for the rapid solution of nonlinear partial differential equations," J. Comput Phys, Vol. 10, pp. 40–52, 1972.

[9] C. W. Bert, S. K. Jang, and A. G. Striz, "Nonlinear bending analysis of orthotropic rectangular plates by the method of differential quadrature," J. Comput Mech, Vol. 5, pp. 217–226, 1989.

[10] C. W. Bert and M. Malik, "Fast computing technique for the transient response of gas-lubricated journal bearings," Proceedings of the U.S. National Congress of Applied Mechanics, Seattle, WA, pp. 298, June 26-July 1, 1994.

[11] C. Shu, W. Chen, H. Xue, and H. Du, "Numerical analysis of grid distribution effect on the accuracy of differential quadrature analysis of beams and plates by error estimation of derivative approximation," Int. Journal of Numer, Methods Engineering, Vol. 51, No. 2, pp. 159–179, 2001.

[12] M. M. Fakir, M. K. Mawlood, W. Asrar, S. Basri, and A. A. Omar, "Triangular fin temperature distribution by the method of differential quadrature," Journal Mekanikal, Malaysia, Vol. 15, pp. 20–31, 2003.

[13] M. M. Fakir, M. K. Mawlood, W. Asrar, S. Basri, and A. A. Omar, "Rectangular fin temperature distribution by the method of differential quadrature," The Journal of the Institute of Engineers, Malaysia (IEM), Vol. 63, No. 4, pp. 41–47, 2002.

[14] E. Hinton and D. R. J. Owen, "An introduction to finite element computations," Pineridge Press Limited, Swansea, U.K., 1985.

[15] S. Tiwari, G. Biswas, P. L. N. Prasad, and S. Basu, "Numerical prediction of flow and heat transfer in a rectangular channel with a built-in circular tube," ASME Journal of Heat Transfer, Vol. 125, No. 3, pp. 413–421, 2003.

[16] B. L. Wang, and Z. H. Tian, "Application of finite element-finite difference method to the determination of transient temperature field in functionally graded materials," Journal of Finite Elements in Analysis and Design, Vol. 41, pp. 335–349, 2005.

[17] S. H. Lo and W. X. Wang, "Finite element mesh generation over intersecting curved surfaces by tracing of neighbours," Journal of Finite Elements in Analysis and Design, Vol. 41, pp. 351–370, 2005.

[18] M. N. Ozisik, "Heat transfer: A basic approach," McGraw-Hill, 1985.

Engineering, 2009, 1, 161-166
doi:10.4236/eng.2009.13019 Published Online November 2009 (http://www.scirp.org/journal/eng).

Effect of Low Velocity Impact Damage on Buckling Properties

Ahmet YAPICI, Mehmet METIN
Mechanical Engineering Department, Mustafa Kemal University, Iskenderun, Turkey
E-mail: *ayapici@mku.edu.tr*
Received January 10, 2009; *revised February* 21, 2009; *accepted February* 23, 2009

Abstract

The work described herein consists of experimental measurement of the post-impact buckling loads of E-glass/epoxy laminates. Composite samples with stacking sequence of $[+45/–45/90/0]_{2s}$ were subjected to low-velocity impact loading at energy levels of 36, 56.13, 79.95, 110.31 and 144 J. The impact tests were conducted with a specially developed vertical drop weight testing machine. Impact parameters like peak load, absorbed energy, deflection at peak load and damage area were evaluated and compared. Damaged specimens were subjected to compressive axial forces and buckling loads of the specimens were obtained. The relation between energy levels and buckling loads is investigated.

Keywords: Low Velocity Impact, E-Glass/Epoxy, Composite, Buckling

1. Introduction

The fiber-reinforced composite plates as used in space vehicles, aircraft, modern vehicles and light weight structure are very susceptible to low velocity transverse impact damage such as matrix cracking, delamination and fiber breakage [1]. Low velocity impacts which may occur during manufacture, maintenance and by careless handling [2] are considered to be dangerous for a composite structure because the damage caused tends to be created on the back face or within the laminate and hence is difficult to detect [3,4]. The dynamic response of composite structures subjected to transient dynamic loading has been studied in terms of analytical, numerical [5,6] and experimental works [7–10]. Theoretically, many works have been developed with an aim of studying the behavior of composite targets under low-velocity impact.

Previous work with thin, impact damaged composite laminates [11–14] has shown that an important mechanism of strength reduction is buckling of delaminated plies. Buckled plies are unable to carry the same proportion of load as unbuckled ones, resulting in a reduced failure load for the complete laminate [15].

Composite materials normally dissipate a significant amount of energy by fracture mechanisms such as matrix cracks, delaminations, fiber fracture, fiber–matrix debonding and fiber pull-out not like more conventional materials (i.e. metals) where the impact energy is mainly absorbed by plastic deformation. Delamination is particularly harmful, since it can seriously degrade the compressive mechanical properties of the material and may propagate under subsequent loads leading to the unexpected failure of the component [16].

In this paper, the results of an experimental study are presented in which flat E-glass/epoxy laminated panels are subjected to low velocity impact and then to buckling force. The relation among energy levels, damage areas and buckling loads is investigated.

2. Experimental

2.1. Materials and Specimens

In this study unidirectional E-glass/epoxy composite plates were used. The panels were cut into specimens of 140 x 140 mm in dimension with an average thickness of 3 mm and stacking sequence of $[+45/-45/90/0]_{2s}$. The mechanical properties of a lamina are listed in Table 1 [17].

Table 1. Mechanical properties of the single layer.

Parameters	Values	Units
Longitudinal modulus E_L	42	(GPa)
In-plane transverse modulus E_T	9.5	(GPa)
Longitudinal tension X_t	690	(MPa)
Shear modulus G_{LT}	3.5	(GPa)
Major Poisson's ratio ν_{LT}	0.34	

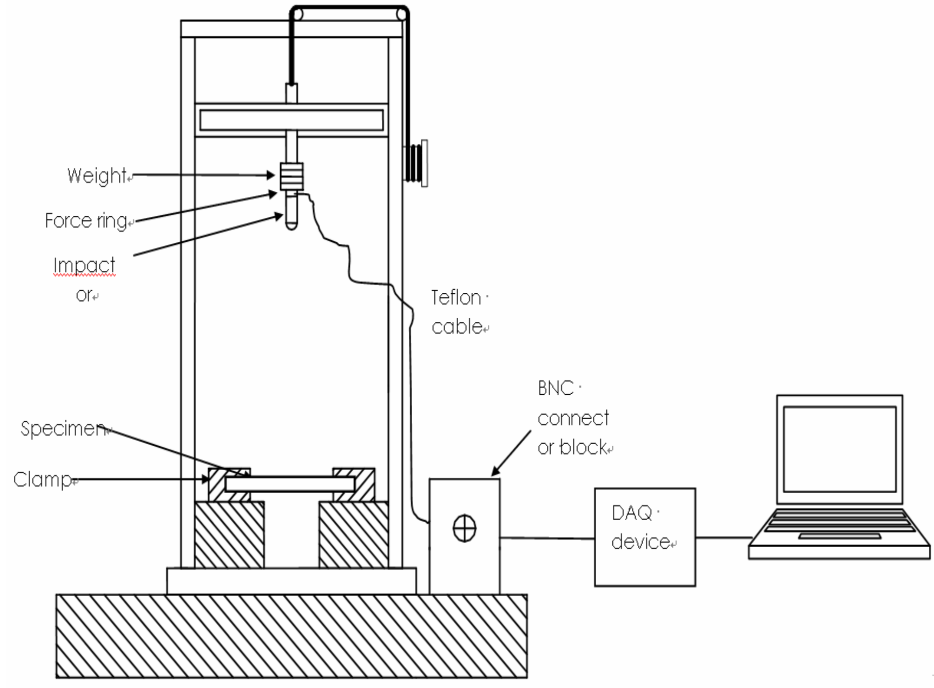

Figure 1. A schematic of drop tower impact machine.

The square specimens were clamped on all four edges to provide an impact area of 130 x 130 mm.

2.2. Low-Velocity Impact Testing

The impact equipment was used to conduct the low velocity impact tests. Figure 1 shows the rig used in this investigation.

Different energy levels can be applied to the clamped specimen by using the impact machine. This machine has three main parts; a drop weight tower, a base plate which holds the specimen and a control unit housing. When the weight released the cylindrical impactor with a hemispherical head (Figure 2) strikes the specimen, the data is recorded by the computer.

Figure 2. The weight and the impactor head.

The specimens were firmly fixed at all edges using clamps and were impacted producing damage up to perforation. The total mass, including impactor, load cell, carriage with linear roller bearings and add-on weights, was 18 kg. Five different energy levels were used for each panel configuration 36, 56.13, 79.95, 110.31 and 144 J to obtain 2.0, 2.5, 3.0, 3.5 and 4.0 m/s impact velocities, respectively. A sophisticated instrumentation is used to record the impact event.

National Instruments (NI) Signal Express data acquisition software is used to obtain the force and time data from the force sensor. The acceleration of the weight is calculated by using Newton's second law of motion. The first integration gives the velocity and the second integration gives the displacement as a function of time. The equation of motion can easily be integrated imposing initial conditions (see [9]). Time axis has its origin at the contact time, while the reference quote h which is at a fixed, known distance from the upper undeformed surface of the specimen. So, the impactor coordinate is $y(0)=0$ at time $t=0$. Considering the impactor as a free falling rigid body, the order of magnitude of its impact velocity at the contact time is obviously given by $v_0=\sqrt{2g\Delta h}$. Δh is defined as the height loss of the gravity center of the impactor mass with respect to the reference surface. This simple integration can be performed on the acceleration to obtain the velocities and, then, the coordinate of the impactor. By integration of the force vs. displacement, the energies time history during the evolution of the test can be evaluated. The formulations of kinematic analysis are given in [9].

Pictures of damaged areas were retrieved from Adobe PhotoShop. The damaged zones were colored and transferred to AutoCAD program and these values of areas were calculated by using spline and area commands, respectively.

2.3. Buckling Testing

Impact-induced delaminations can significantly reduce the compressive strength of the structure. A number of investigators studied the stability of laminated plates with impact-induced delaminations. Buckling and delaminations growth are thought to be the first steps in the compressive failure process. The question is how much load the damaged structure can withstand [18]. In the study the damaged specimen is placed between the plates of the tensile test machine without clamping and then compressive force is applied. Buckling load for different specimens was found.

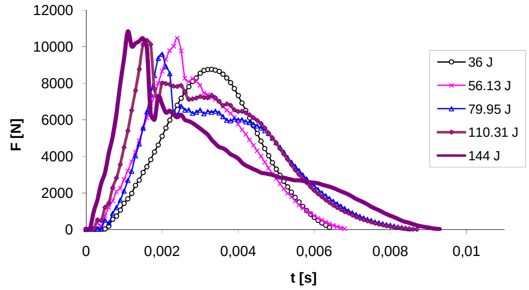

Figure 3. Impact force versus time for 36, 56.13, 79.95, 110.31 and 144 J.

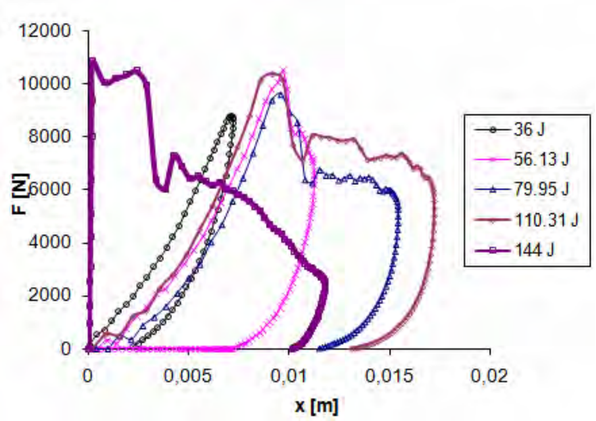

Figure 4. Impact force versus indentation for 36, 56.13, 79.95, 110.31 and 144 J.

3. Results and Discussions

Specimens were tested under five energy levels 36.00, 56.13, 79.95, 110.31 and 144 J. It was observed that the average peak load (Figure 3) at which the specimens failed is 8.758 kN at 36 J, 10.47 kN at 56.13 J, 9.58 kN at 79.95 J, 10.12 kN at 110.31 J and 10.83 kN at 144 J. This shows that there was an increase in the peak load as the energy levels were increased but at 79.95 J there is a drop in force because of the begining of the perforation. The absorbed energy at 36.00, 56.13, 79.95, 110.31 and 144 J was 25.4, 45.8, 76.7, 105.9 and 141.9 J respectively. Absorbed energy is the energy at the peak load deducted from the total energy. As the composite materials are generally brittle in nature, it is assumed here that the energy up to the peak load is absorbed through elastic deformation and all the energy that is absorbed beyond that is assumed to be absorbed through the creation of damages.

Figure 4 shows the relation between the instant impact force (F) and deflection of the specimen (x). The work done on the sample was calculated from the area under the force- displacement curve. Deflection at peak load for 36, 56.13, 79.95, 110.31 and 144 J is 7.11, 9.67, 9.56, 9.12 and 0.22 mm, respectively. After the begining of the perforation (at 79.95 J) the deflection decreases. Because some of the energy is used to perforate the laminate.

The impact energy is defined as a sum of absorbed and rebound energies. Matrix cracking, delamination and fiber breakage is caused by this absorbed energy. The damage areas of the specimens for 36, 56.13, 79.95, 110.31 and 144 J are 278, 499.19, 683.75, 655.24 and 558 mm^2 (Figure 5). It is seen that the damage area is increasing by increasing the energy level until the perforation starts. After the perforation by increasing the energy level the damage area is decreasing. Becasue at this stage absorbed energy is used for fiber breakage. Figure 5 also shows front and back surface of the laminates. Because of the moment, on the back surface tensile and on the front surface compressive stress is taken place. On the back surface of the laminates diagonal debonding is greater than the front surface.

After the impact tests the specimens placed between the clamp of tensile test machine as free ends and then compressive force applied to the specimens. Table 2 shows the relation between impact energy and buckling load of the specimens.

It is seen that the buckling load decreases while the impact energy increases until the beginning of the perforation but after the perforation because of the increase in velocity the damaged area decreases (absorbed energy is used to create a hole by fiber breakage) and buckling load increases. This means that bigness of the damaged area is more critical than the hole for a specimen.

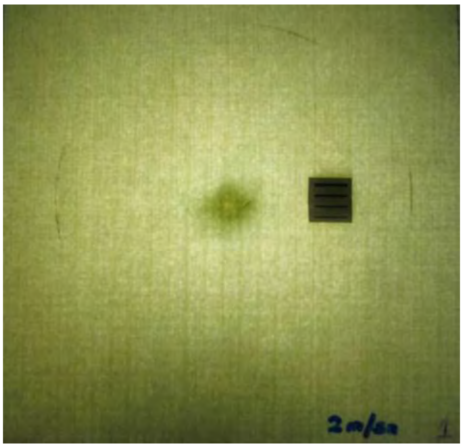

(a) Front surface for 36 J.

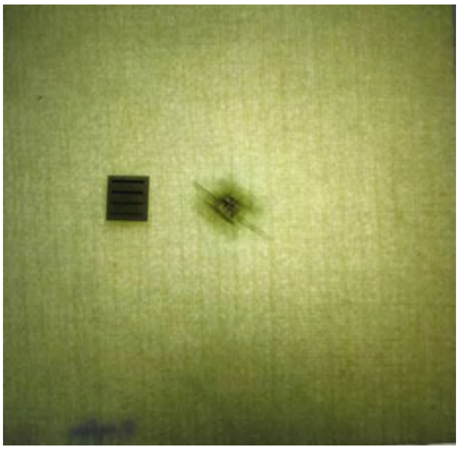

(b) Back surface for 36 J.

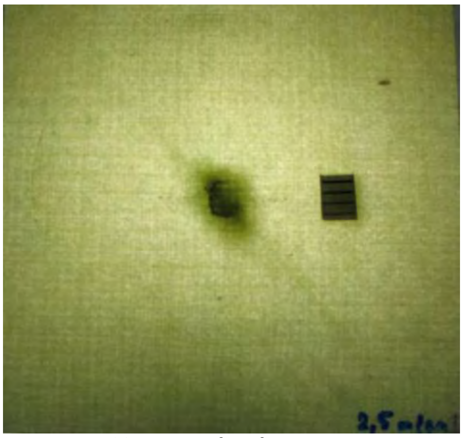

(c) Front surface for 56.13 J.

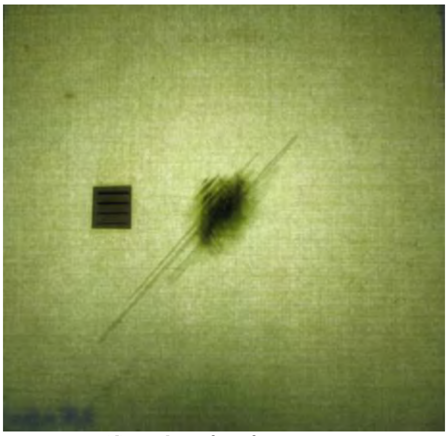

(d) Back surface for 56.13 J.

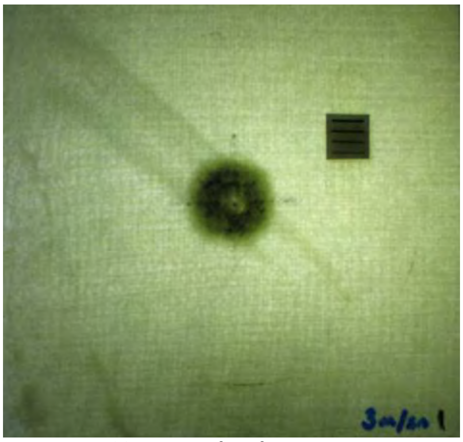

(e) Front surface for 79.95 J.

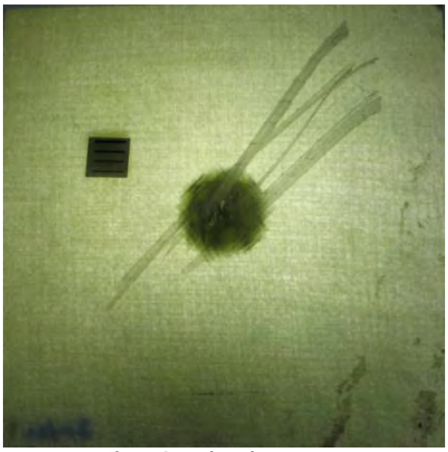

(f) Back surface for 79.95 J.

In other words, sum of matrix cracking, delamination decreases the buckling strength more than a hole (fiber-breakage). Also it is seen that 36 J not perforated and 144 J perforated impact energy has the same effect on buckling properties.

4. Conclusions

The composite plates were subjected to low velocity impact. The relation between the force-time and force-deflection was found. It is seen that while the energy

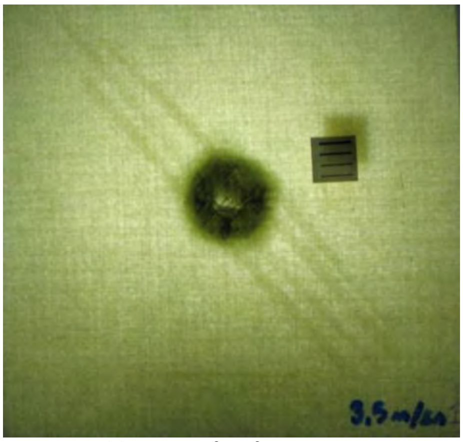

(g) Front surface for 110.31 J.

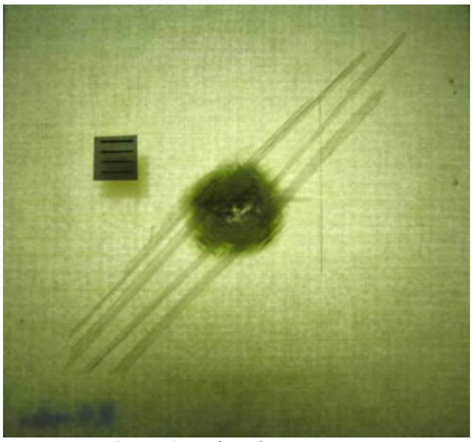

(h) Back surface for 110.31 J.

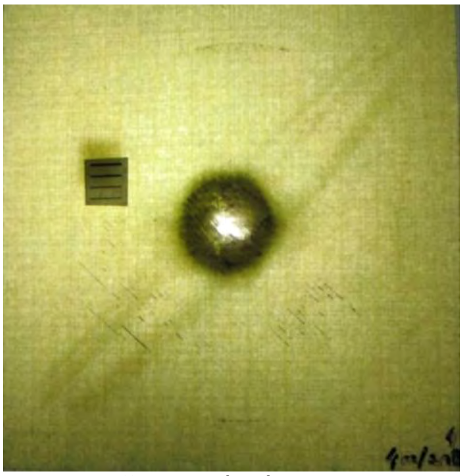

(i) Front surface for 144 J.

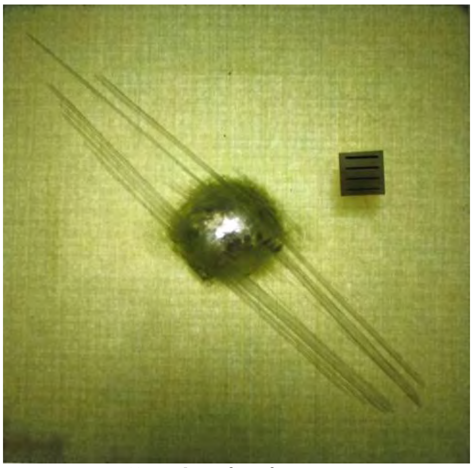

(j) Back surface for 144 J.

Figure 5. Damage areas of impacted specimen.

Table 2. Buckling load for 36, 56.13, 79.95, 110.31 and 144J.

	Impact Energy [J]	Buckling Force [kN]
	0	13
Not perforated	36	10
	56.13	9
	79.95	6.5
Perforated	110.31	8
	144	10

(impact velocity) increases the peak in force increases but there is a drop at the beginning of the perforation.

The total energy is used for matrix cracking, delamination, fiber breakage and elastic energy to make the indenter jump (other unimportant energy loss can be neglected). It is seen that when the impact energy increases the damaged area also increases and buckling load decreases until the beginning of the perforation. For 110.31 J, because of the increase in velocity (3.5 m/s), perforation is occur and the part of the energy, used for matrix cracking and delamination, is used for fiber breakage thus the damage area decreases. When the damage area starts to decrease the buckling load starts to increase after the perforation.

5. References

[1] R. Tiberkak, M. Bachene, S. Rechak, and B. Necib, "Damage prediction in composite plates subjected to low velocity impact," Composite Structures, Vol. 83, No. 1, pp. 73–82, 2008.

[2] C. Bert, "Recent advances in dynamics of composite structures," Composite Structures IV, Damage Assess Mater Eval., Vol. 2, pp. 1–17, 1987.

[3] W. Cantwell and J. Morton, "Detection of impact damage in CFRP laminates," Composite Structures, Vol. 3, pp. 241–57, 1987.

[4] A. R. Chambers, M. C. Mowlem, and L. Dokos, "Evaluating impact damage in CFRP using fibre optic sensors," Composites Science and Technology, Vol. 67, pp. 1235–1242, 2007.

[5] C. F. Li, N. Hu, Y. J. Yin, H. Sekine, and H. Fukunaga, "Low-velocity impact damage of continuous fiber reinforced composite laminates," Part I, An FEM Numerical Model, Composites: Part A, Vol. 33, pp. 1055–62, 2002.

[6] C. F. Li, N. Hu, Y. G. Cheng, H. Fukunaga, and H. Sekine, "Low-velocity impact-induced damage of continuous fiber-reinforced composite laminates," Part II Verification and Numerical Investigation, Composites: Part A, 33, pp. 1063–72, 2002.

[7] Z. Aslan, R. Karakuzu, and B. Okutan, "The response of laminated composite plates under low-velocity impact loading," Composite Structures, Vol. 59, pp. 119–27, 2003.

[8] F. Mili and B. Necib, "Impact behavior of cross-ply laminated composite plates under low velocities," Composite Structures, Vol. 51, pp. 237–44, 2001.

[9] M. Uyaner and M. Kara, "Dynamic Response of Laminated Composites Subjected to Low-velocity Impact," Journal of Composite Materials, Vol. 41, No. 24, pp. 2877–2896, 2007.

[10] B. Whittingham, I. H. Marshall, T. Mitrevski, and R. Jones, "The response of composite structures with pre-stress subject to low velocity impact damage," Composite Structures, Vol. 66, pp. 685–698, 2004.

[11] G. Clark, "Modelling of impact damage in composite laminates," Composites, Vol. 20, pp. 209–14, 1989.

[12] Y. Xiong, C. Poon, P. V. Straznicky, and H. Vietinghoff, "A prediction method for the compressive strength of impact damaged composite laminates," Composite Structures, Vol. 30, pp. 357–67, 1995.

[13] M. J. Pavier and M. P. Clarke, "Finite element prediction of post impact compressive strength in carbon fibre composites," Composite Structures, Vol. 36, pp. 141–53, 1996.

[14] M. de Freitas and L. Reis, "Failure mechanisms of composite specimens subjected to compression after impact," Composite Structures, Vol. 42, pp. 365–73, 1998.

[15] G. J. Short, F. J. Guild, and M. J. Pavier, "Post-impact compressive strength of curved GFRP laminates," Composites: Part. A, Vol. 33, pp. 1487–1495, 2002.

[16] F. Aymerich, C. Pani, and P. Priolo, "Effect of stitching on the low-velocity impact response of $[0_3/90_3]_s$ graphite/epoxy laminates," Composites: Part. A, Vol. 38, pp. 1174–1182, 2007.

[17] M. Metin, "The effect of low-velocity impact damage on buckling behavior of E-glass/epoxy laminated composites," M. S. Thesis in Mechanical Engineering, Selcuk University Konya, Turkey, 2008.

[18] S. Abrate, "Impact on composite structure," Cambridge University Press, NY, USA, 1998.

Engineering, 2009, 1, 167-176
doi:10.4236/eng.2009.13020 Published Online November 2009 (http://www.scirp.org/journal/eng).

Detection and Quantification of Structural Damage of a Beam-Like Structure Using Natural Frequencies

Saptarshi SASMAL, K. RAMANJANEYULU
Structural Engineering Research Centre, Council of Scientific and Industrial Research (CSIR), Chennai, India
E-mail: *saptarshi@sercm.org, sasmalsap@gmail.com*
Received January 10, 2009; *revised February* 21, 2009; *accepted February* 23, 2009

Abstract

Need for developing efficient non-destructive damage detection procedures for civil engineering structures is growing rapidly. This paper presents a methodology for detection and quantification of structural damage using modal information obtained from transfer matrix technique. Vibration characteristics of beam-like structure have been determined using the computer program developed based on the formulations presented in the paper. It has been noted from reported literature that detection and quantification of damage using mode shape information is difficult and further, extraction of mode shape information has practical difficulties and limitations. Hence, a methodology for detection and quantification of damage in structure using tranfer matrix technique based on the changes in the natural frequencies has been developed. With an assumption of damage at a particular segment of the beam-like structure, an iterative procedure has been formulated to converge the calculated and measured frequencies by adjusting flexural rigidity of elements and then, the intersections are used for detection and quantification of damage. Eventhough the developed methodology is iterative, computational effort is reduced considerably by using transfer matrix technique. It is observed that the methodology is capable of predicting the location and magnitude of damage quite accurately.

Keywords: Frequency, Mode Shape, Transfer Matrix, Damage Detection, Quantification

1. Introduction

The need for development of an efficient procedure for non-destructive structural damage detection is increasing in order to assess the integrity and serviceability of existing structures. This has led to continued research to develop methods that could identify changes in vibration characteristics of a structure. These methods are based on the fact that modal parameters (notably frequencies and mode shapes, and modal damping) are functions of the physical properties of the structure (mass, damping, and stiffness). Any change in the physical properties, such as reduction in stiffness resulting from cracking or loosening of a connection, will cause detectable change in the modal properties. Various methods have been employed by researchers all over the world for damage detection of structural systems, in frequency domain.

Perhaps, the first research article on damage detection using vibration measurements was by Lifshitz and Rotem [1] where the change in the dynamic moduli was related to the frequency shift and proposed as indicator of damage in particle-filled elastomers. Cawley and Adams [2] are the first researchers to give a formulation for damage detection based on change in frequency of an undamaged and damaged state of a structure. The systematic use of mode shape information was proposed in [3] for localizing of structural damage without the use of a prior finite element model (FEM) by using the modal assurance criteria (MAC) to determine the level of correlation between modes from the test of an undamaged space shuttle orbiter body flap. Yuen [4] examined changes in the mode shape and mode-shape-slope parameters to simulate the reduction of stiffness in each structural element and compared predicted changes with the measured changes to determine the damage location. Ismail *et al.* [5] demonstrated that the frequency drop caused by an opening and closing crack is less than that caused by an open crack. This property is a potentially large source of error that is considered by few of the researchers using frequency changes. A simple and easy method for one-dimensional structures by representing crack using a spring that connects the two half components was presented by [6]. The natural frequencies were expressed as functions of the crack depth and location. Hearn and Testa [7] developed a damage detection method using frequency shift of a structure due to damage. The frequency sensitivity method combined with internal-state-variable theory to detect damage in composites was used in [8]. They presented a damage indicator which is capable of detecting damage due to 1) extensional stiffness changes caused by matrix micro-cracking and 2) changes in bending stiffness caused by transverse cracks in the 90-degree plies. An experimental study on the sensitivity of the measured modal parameters of a shell structure was conducted in [9] to damage in the form of a notch. A method for the detection of the existence and location of structural damage using the identified eigen solution together with properties of the eigenvalue problem was proposed in [10].

Slater and Shelley [11] presented a method based on frequency-shift measurements to detect damage in a smart structure by using the theory of modal filters to track the frequency changes over time. Narkis [12] deduced a closed-form solution for the crack position, as function of the frequency shift of two modes of the same mechanical model and located the crack from measuring either bending or axial frequencies of two modes only. A transfer matrix technique was used in [13] to detect damage for beam like structures. Ratcliffe [14] developed a technique for identifying the location of structural damage in a beam using modified Laplacian Operator on mode shape data. A sensitivity- and statistical- based method to localize structural damage by direct use of incomplete mode shapes was presented in [15] and [16]. A numerical study of damage detection using the relationship between damage characteristics and the changes in the dynamic properties was presented by [17]. It was found that the rotation of mode shape is a sensitive indicator of damage localisation. Another damage localisation method based on changes in uniform load surface (ULS) curvature was developed by Wu and Law [18]. A procedure using gap smoothing method was proposed in [19] wherein local features in vibration curvature shapes were extracted using a localized curve fit (i.e., smoothing). Alvandi and Cremona [20] reviewed usual vibration-based damage identification techniques for structural damage evaluation. With the help of a simply supported beam with different damage levels, the reliability of these techniques was investigated by using only few mode shapes and/or modal frequencies of the structure that can be easily obtained by dynamic tests and concluded that broadly the detection judgement depends on a threshold level of damage.

1.1. Detection of Damage Using Mode Shape Information

From the review of literature, it is found that the vibration data such as frequency and mode shape are very important parameters for detecting the damage in structures and a number of research works was carried out on detection of damage using frequency or mode shape. But, there is no confirmation on superiority of any method over the others. Though, changes in mode shape are much more sensitive to local damage compared to changes in frequency, use of mode shape information is restricted because 1) lower modes (usually measured from vibration tests of large structure) may not significantly reflect the local damage, 2) extracted mode shapes are prone to environmental noise and 3) number of sensors and the choice of sensor location may have a crucial effect on accuracy of damage detection. So, a detailed investigation has been carried out by the authors to assess the influence of location and degree of damage on mode shape. It is found that 1) displacement mode shapes are sensitive to damage and the mode shape changes with damage, 2) though higher modes are more predominant in showing the shift in mode shape displacements due to damage in the structure, lower modes may not significantly reflect the damage, 3) shift in mode shape largely depends on the location of damage and the mode considered. Higher mode will magnify the shift in mode shape, if the damage location does not fall near the zero-displacement points, 4) any shift in mode shape of a damaged structure with respect to the mode shape of undamaged structure may lead to an interpretation of damage in that location, and in most of the cases, it may go wrong. Further, for higher modes, if the damage is located at a location where zero displacement occurs in that particular mode, shift in mode shape will be reflected in place other than the place where damage has really taken place, 5) Shift in mode shape is predominant in higher modes than in the lower modes. It may show a number of locations with shift in mode shape with respect to undamaged mode shape which may lead to misinterpretation of location of damage. So, it can be stated that mode shape information alone can not provide correct information on detection of damage in the structure unless it is treated otherwise, and 6) it is very difficult to quantify damage accurately from mode shape information alone. Further studies can be seen elsewhere [21,22].

Though significant damage might cause very small changes in natural frequency (particularly for large structures), natural frequencies are easy to be measured and are less influenced by environmental noise. The choice of using the natural frequency as a basic vibration characteristic for damage detection is the most attractive one due to the fact that the natural frequencies of a structure can be measured at one single location in the structure, thus rendering a means for a rapid and global technique. Further, it is observed that studies related to the extension of transfer matrix method for detection of damage are very few. Hence, in this study, a methodology for detection of damage in structures using transfer matrix technique has been proposed based on change in natural frequency. The extent of research work carried out towards quantification of damage is considerably less compared to studies on localisation of damage. In view of this, a methodology has been developed in this study for detection and quantification of damage using transfer matrix method based on modal frequencies obtained from a damaged structure. Transfer matrix method [23] is used in this study because of its versatility and ease with which it can be applied to a structure of either uniform or non-uniform cross section and under a variety of boundary conditions such as simple support, cantilever support, and even for beam on elastic foundation. Moreover, for a methodology based on an iterative algorithm, as proposed in this study, transfer matrix method is very useful and easy to handle compared to FE formulation. Theoretical developments of the methodology for detection and quantification of damage are presented first, followed by detailed numerical studies to demonstrate the efficacy of the proposed method.

2. Transfer Matrix Method for Obtaining Modal Parameters

For computing plane flexural vibrations of a straight beam using transfer matrix method, the beam section is modelled by discrete uniform structural elements interconnected at the nodal points. Using the conventional assumption of a mass-less beam, the inertia effects of the beam element are dynamically represented by two lumped masses at both ends of the element (as shown in Figure 1).

Each individual beam is considered to be of individual homogenous material property and geometry which can be represented by area moment of inertia and Young's modulus of that particular element. Two displacements, viz., vertical deflection (η) and rotation (φ) and the corresponding forces viz., shear force (V) and bending moment (M) are considered for describing the state array variables at each section and the sign convention of the state array variables is shown in Figure 2.

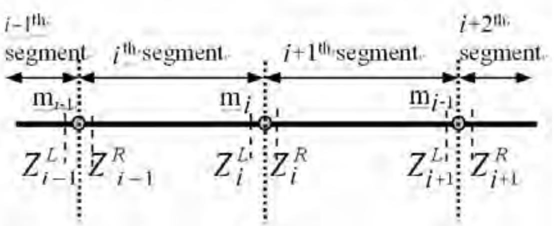

Figure 1. Beam with concentrated masses.

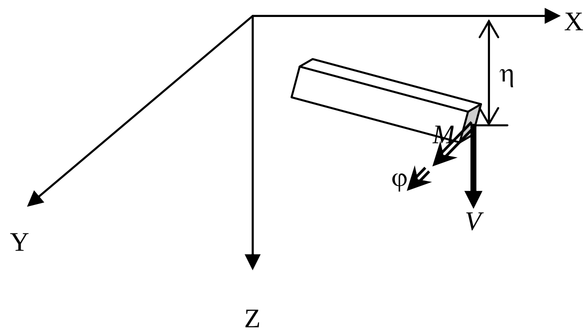

Figure 2. Sign convention for state array variables of beam element.

The equilibrium between sections *i* and *i*-1 of an element will be maintained by

$$V_i^L - V_{i-1}^R = 0 \tag{1}$$

$$M_i^L - M_{i-1}^R - V_i^L l_i = 0 \tag{2}$$

where the superscript L and R stands for left and right side of a section respectively.

Two more equations that are required for solving the problem can be obtained from compatibility conditions and the final equations can be expressed as

$$\eta_i^L = \eta_i^R + l_i\phi_{i-1}^R + \frac{l_i^2}{2(EI)_i}M_{i-1}^R + \frac{l_i^3}{6(EI)_i}V_{i-1}^R \tag{3}$$

$$\phi_i^L = \phi_{i-1}^R + \frac{l_i}{(EI)_i}M_{i-1}^R + \frac{l_i^2}{2(EI)_i}V_{i-1}^R \tag{4}$$

$$M_i^L = M_{i-1}^R + l_i V_{i-1}^R \tag{5}$$

$$V_i^L = V_{i-1}^R \tag{6}$$

and can be expressed in matrix form as,

$$\begin{bmatrix} -\eta \\ \phi \\ M \\ V \end{bmatrix}_i^L = \begin{bmatrix} 1 & l & \frac{l^2}{2EI} & \frac{l^3}{6EI} \\ 0 & 1 & \frac{l}{EI} & \frac{l^2}{2EI} \\ 0 & 0 & 1 & l \\ 0 & 0 & 0 & 1 \end{bmatrix}_i \begin{bmatrix} -\eta \\ \phi \\ M \\ V \end{bmatrix}_{i-1}^R \tag{7}$$

So, from Equation (7), the field matrix ($\mathbf{F}_i$) connecting Z_i^L with Z_{i-1}^R can be expressed as

$$Z_i^L = \mathbf{F}_i Z_{i-1}^R \tag{8}$$

The point matrix ($\mathbf{P}_i$) connecting Z_i^R with Z_i^L is found by using continuity of deflection, slope and moment across the concentrated mass m_i,

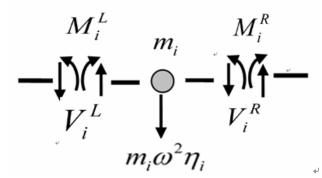

Figure 3. Free-body diagram of mass m_i.

$$\eta_i^R = \eta_i^L \ ; \quad \phi_i^R = \phi_i^L \quad \text{and} \quad M_i^R = M_i^L \tag{9}$$

The vibrating mass, however, introduces the inertial force which causes discontinuity in shear. The free-body diagram shown in Figure 3 yields a relation from simple equilibrium considerations as:

$$V_i^R = V_i^L \pm m_i\omega^2\eta_i \tag{10}$$

(in formulation, a particular sign convention has been followed)

Equations (9) and (10) can be expressed in matrix form as:

$$\begin{vmatrix} u_{12}^n & u_{14}^n \\ u_{32}^n & u_{34}^n \end{vmatrix} \begin{bmatrix} -\eta \\ \phi \\ M \\ V \end{bmatrix}_i^R = \begin{bmatrix} 1 & 0 & 0 & 0 \\ 0 & 1 & 0 & 0 \\ 0 & 0 & 1 & 0 \\ m_i\omega^2 & 0 & 0 & 1 \end{bmatrix}_i \begin{bmatrix} -\eta \\ \phi \\ M \\ V \end{bmatrix}_i^L \tag{11}$$

$$Z_i^R = \mathbf{P}_i Z_i^L \tag{12}$$

By combining both field and point matrices, relation between the state vectors of adjacent ends (i and i-1) can be obtained as

$$Z_i^R = \mathbf{P}_i\mathbf{F}_i Z_{i-1}^R \tag{13}$$

2.1. Transfer Matrix for Frequency Determinant

The transfer matrix method can be applied to solve more complicated problems by considering a beam that is made up of piecewise uniform mass-less elements, with masses concentrated at discrete points. If a structural element is made up of n segments (between the ends 0 to n), relationship between the state vectors at the extreme ends (0 and n) of the beam can be obtained as

$$Z_n = \mathrm{F_n P_{n\text{-}1} F_{n-1}} \ldots\ldots\ldots \mathrm{P_4F_4P_3F_3P_2F_2P_1F_1}Z_0$$

$$Z_n = \mathbf{U}Z_0 \tag{14}$$

Equation (14) can be written in full, as

$$\begin{bmatrix} -\eta \\ \phi \\ M \\ V \end{bmatrix}_n = \begin{bmatrix} u_{11}^n & u_{12}^n & u_{13}^n & u_{14}^n \\ u_{21}^n & u_{22}^n & u_{23}^n & u_{24}^n \\ u_{31}^n & u_{32}^n & u_{33}^n & u_{34}^n \\ u_{41}^n & u_{42}^n & u_{43}^n & u_{44}^n \end{bmatrix}_i \begin{bmatrix} -\eta \\ \phi \\ M \\ V \end{bmatrix}_0 \tag{15}$$

where the coefficients u_{11}^n to u_{44}^n are functions of circular frequency ω. Boundary conditions can be applied to the equations formulated from Equation (15) to arrive at the frequency determinant. For example, a beam (consists of n segments) with simply supported ends can besolved as follows:

The boundary conditions at simply supported ends are $\eta_n = 0$, $M_n = 0$, $\eta_0 = 0$, and $M_0 = 0$;

By substituting these boundary conditions in Equation (15), the following relation can be obtained

$$u_{12}^n\phi_0 + u_{14}^n V_0 = 0 \tag{16a}$$

And,

$$u_{32}^n\phi_0 + u_{34}^n V_0 = 0 \tag{16b}$$

where u_{ij}^k is element of i^{th} row and j^{th} column of the transfer matrix which can be obtained by using Equation (15) and superscript k denotes the number of segments. The normal modes can be found for the system using the following procedure.

For a nontrivial solution of Equations (16a) and (16b), the determinant of the coefficients must be zero, that is

$$\begin{vmatrix} u_{12}^n & u_{14}^n \\ u_{32}^n & u_{34}^n \end{vmatrix} = 0 \tag{17}$$

The same procedure can be followed for other boundary conditions also. Since, the elements u_{ij} are functions of the circular frequency ω, this determinant serves to compute the natural circular frequencies. In view of the fact that a beam which possesses n segments will have n-1 discrete masses, the expansion of the frequency determinant leads to an equation of n-1 degree in ω^2.

2.2. Numerical Procedure for Solution of Frequency Equation

In the preceding section, the matrix multiplications have been made by treating ω^2 as a free parameter. After applying the boundary conditions the resulting frequency equations are solved for ω^2. For complicated systems, the algebraic solution would become complicated and furthermore, it would be very cumbersome to extract the roots. In such cases, it is advantageous to replace algebraic solution with numerical computation. For system with 'n' segments with simply supported ends, the frequency determinant (as described in Equation 17) would become

$$\Delta = \begin{vmatrix} u_{12}^n & u_{14}^n \\ u_{22}^n & u_{24}^n \end{vmatrix} = 0 \tag{18}$$

If the matrix multiplication is carried out algebraically, then the coefficients u_{12}^n, u_{14}^n, u_{22}^n and u_{24}^n and consequently the frequency condition would be complicated functions of ω^2. The procedure adopted in practice, however, is to choose certain values for ω^2 and compute the corresponding values of the frequency determinant $\Delta(\omega)$. The value of the determinant Δ is then plotted against ω, the zero values of Δ occur at the natural circular frequencies of the system. This procedure has been adopted in the study for tracking of frequencies.

3. Determination of Frequency of a Structure Using Transfer Matrix Method

In this study, a computer program called FREQ has been developed based on the formulation presented in the preceding sections and the flow-chart of the program for obtaining frequencies of a structure, is shown in Figure 4. The formulations and the computer program have been validated by comparing the results of this study with those obtained using Finite Element Analysis (FEA). Table 1 gives the comparison of frequencies obtained by using transfer matrix method and FEA. From this table, it can be seen that the results of this study are in good agreement with those obtained using satndard FEA package. For the validation study, a beam with 90 elements have been considered with Young's modulus (E)= 25×10^6 kN/m^2, moment of inertia (I)= 0.001333 m^4 and cross sectional area (A) = 0.1 m^2.

As discussed in the preceding section, the determinant for the whole beam after incorporating the boundary conditions is computed for an assumed (initial) natural frequency. Then, an iterative procedure has been carried out by incrementing natural frequency to get the determinant of the transfer matrix. The frequency for which the determinant value is nearly zero, has been assigned as the natural frequency of the beam. The variation of the determinant of the transfer matrix for different modes of the beam is shown in Figure 5. For clarity, the determinant value (Δ) has been scaled down suitably after reaching a particular frequency. For example, for first, second and third natural frequencies, the determinant (Δ) of the transfer matrix is scaled down to 1/10th, 1/100th

Table 1. Comparison of frequency obtained using transfer matrix method and FEA.

Modes	Frequency (ω) in Hz
First mode	5.648 (5.670)
Second mode	22.564 (22.557)
Third mode	50.478 (50.306)
Fourth mode	88.108 (88.352)
Note: Results obtained from FEA are presented in brackets	

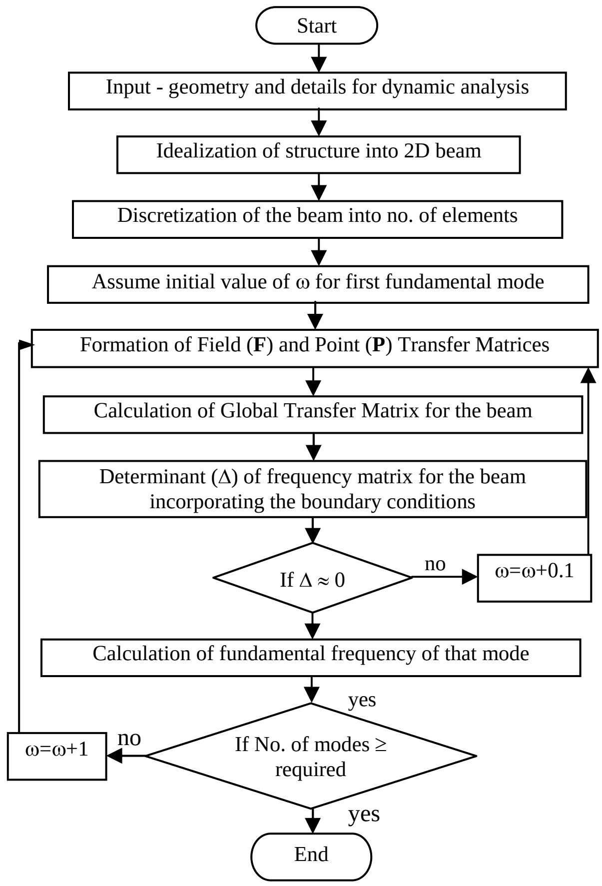

Figure 4. Flow-chart of computer program (FREQ).

and 1/500th respectively. The frequencies corresponding to zero values of the determinant (Δ) represent the natural frequencies (ω) of the beam for different modes (as shown in Figure 5).

The central philosophy of detection of damage of beam like structure using transfer matrix formulation presented here, is to determine the reduction in flexural rigidity of one or more elements of the beam which would signify the existence of damage in the structure. In this context, question may arise that how far the frequencies of a structure are influenced by the damage in a particular element(s), in other words, what is the change in the determinant of transfer matrix with the change in flexural rigidity in one or more elements of the beam. In view of this, a study has been carried out to evaluate the frequency determinant by changing the magnitude and locations of the damaged element(s) to evaluate the influence of location and magnitude of damage on frequency of a structure. It is noticed that the frequencies corresponding to higher modes are influenced predominantly by change in flexural rigidity of one or more elements of the beam. For clarity, the changes in determinant values for the first two frequencies are shown in Figure 6. It is observed from the figure that by reducing

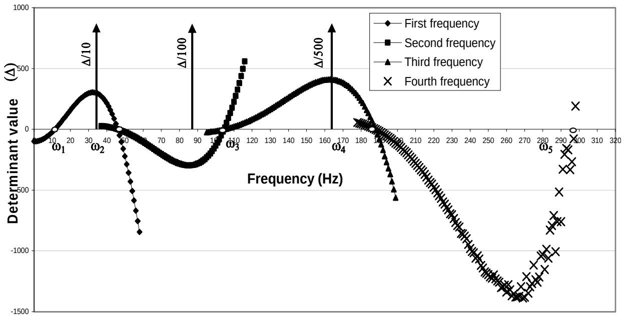

Figure 5. Variation of determinant of transfer matrix for different modes.

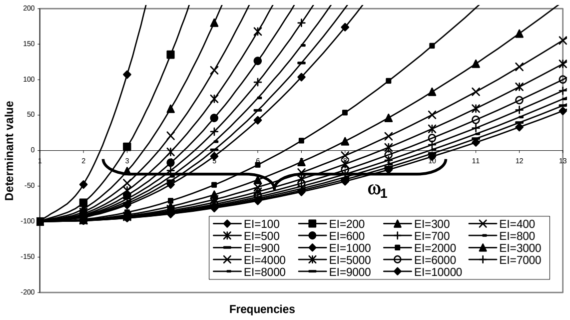

(a) For first fundamental frequency.

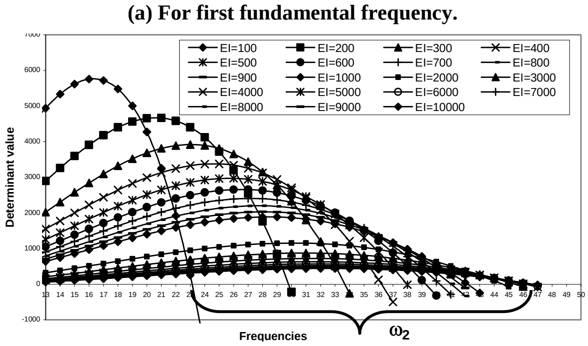

(b) For second fundamental frequency.

Figure 6. Variation of determinant with degree of damage (EI in kNm^2).

flexural rigidity of a particular element of the beam considered in this study, frequency of the second mode varies over a wider range than that of the first mode. This signifies that the shift in frequency of second mode due to damage is more predominant than that in the first mode frequency. It is also noted from the study that this phenomenon is valid for next higher modes.

4. Results and Discussions

Though the transfer matrix technique can easily be applied to any type of structure with appropriate boundary conditions, a beam like structure with simply supported ends is considered in this study to demonstrate the efficacy of the methodology and its accuracy. The material

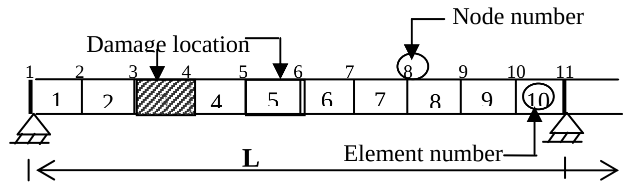

Figure 7. A typical beam like structure with elements and node numbers.

and sectional properties of the beam considered in this study are same as that mentioned for validation study. It is true that a finer division of a structure would lead to a more precise result, but for demonstrating the methodology proposed in this study, a beam like structure with 10 elements (as shown in Figure 7) has been considered for better representation, faster computation and clarity. Another reason behind considering less number of elements in this study is that for single-spread damage case, coarser mesh can occupy maximum amount of damage in minimum number of elements which would reduce the computation time without sacrificing the efficiency.

4.1. Solution Procedure for Detection of Damage Using Change in Frequencies.

The methodology proposed in this study, uses natural frequency information obtained from the transfer matrix formulations, for detection, quantification and localization of damage. A beam with known location and magnitude of damage has been analysed for extracting the natural frequencies. The existence of orthogonal damage in a beam structure can be simulated numerically via a change in flexural rigidity (EI) in a particular beam element. Such changes or reduction in flexural rigidity would result in change or decrease in the natural frequencies of the system. Through the measurement of the system natural frequencies of the structure, the location and magnitude of the damage can be determined. Assuming that flexural rigidity of all the segments of the system are known, the dynamics of the system can be obtained by the numerical model described in the preceding section.

When damage has occurred in a certain beam segment, it can be detected through the changes in the system natural frequencies. For the system containing damage, the iterative procedure starts with an assumption that the damage is located at the first beam element. The corresponding flexural rigidity of the element is adjusted until the first natural frequency of the system is matched with the measured one. The process is then continued with the second segment of the structure and the first natural frequency of the system is again matched by adjusting the flexural rigidity of the second element. The process is repeated for all the segments of the structure. The same technique is followed for other modes which can be measured through vibration testing. The location and magnitude of the damage of the structure can be identified by the intersection of various rigidity-versus- damaged beam element location curves. The intersection of the curves obtained for different modes represent damage locations and magnitudes (flexural rigidity) which caused the changes in the system natural frequencies. Flow-chart of the computer program developed in this study based on the formulation described above for detection and quantification of structural damage is shown in Figure 8.

4.2. Case Study

For a numerical simulation, a beam is considered where the geometric and material properties are same as that mentioned for validation study. It is significant to mention that, in this study, 1) single damage does not represent only one damage (one crack) in the entire structure which is not practical in real structure too. As the formulation states, an element in the structure can be chosen to take a considerable length of the structure. The proposed methodology would show the location and magnitude of damage in an element considering all the damages occurred in that particular element which can be used for further discretisation, if required, to arrive at more particular locations. 2) It is also noticed that the most of the reported methodologies for damage detection perform well when degree of damage is very severe. But, in real practice, when large damages are already included in the structure, a sophisticated methodology for damage detection is not required, rather it can be located either by visual observation or simple inspection techniques. So, in this study, low levels of damages are considered to illustrate the methodology and to check its acceptability. 3) For all the case studies presented here, frequencies corresponding to only first four modes are considered because more number of modes may not be available from the field experiments. It is always a challenging problem to detect and quantify damage from less number of modes. Further, consideration of more number of modes is computationally expensive too.

Three levels of damage in two different locations have been studied separately, i.e, a beam with 10%, 20% and 30% damage in an element near support (3rd element as shown in Figure 7) and near centre (5th element as shown in Figure 7) respectively. These studies have been considered to examine the performance of the proposed methodology because it is known that the change in frequency with damage (reduction in flexural rigidity) of a structure greatly depends on the degree and location of damage.

Using the proposed methodology and computer program developed based on the flow-chart shown in Figure 8, iterative study has been carried out for satisfying the frequencies corresponding to different modes of a damaged beam. Final flexural rigidities of each element along the length of the beam are obtained from the computer program and plotted for the cases mentioned above. It is observed that the true location and magnitude of the damage are identified by the intersection of the various rigidity versus element location curves. Cases with damage of 10% (remaining flexural rigidity of 29993 kNm^2) in 3rd and 5th element are shown in Figure 9 and Figure 10 respectively. It is observed from Figures 9 and 10 that intersections of curves for different modes correctly indicate the damage locations (in 3rd and 5th element) with a remaining flexural rigidity of 30000 kNm^2.

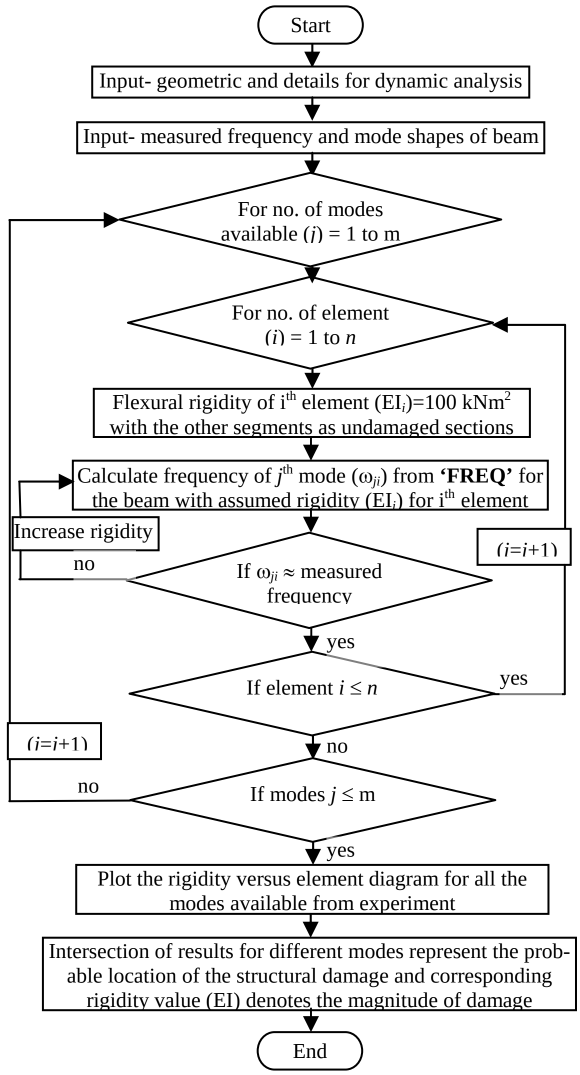

Figure 8. Flow chart for detection and localisation of structural damage.

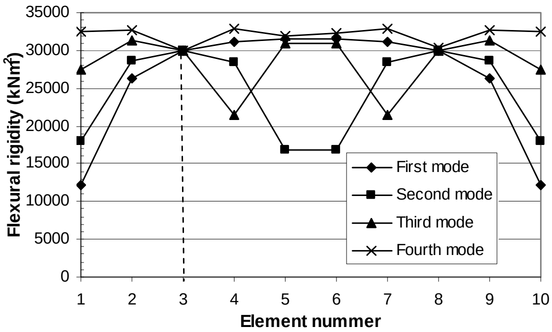

Figure 9. Flexural rigidity versus element diagram for 10% damage in 3rd element.

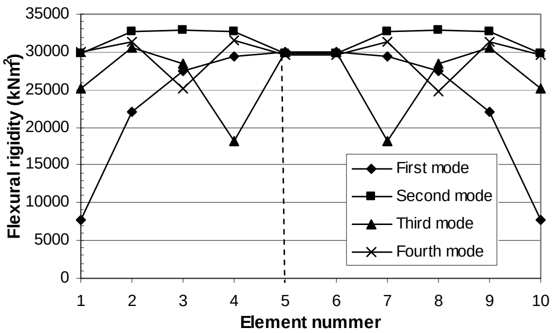

Figure 10. Flexural rigidity versus element diagram for 10% damage in 5th element.

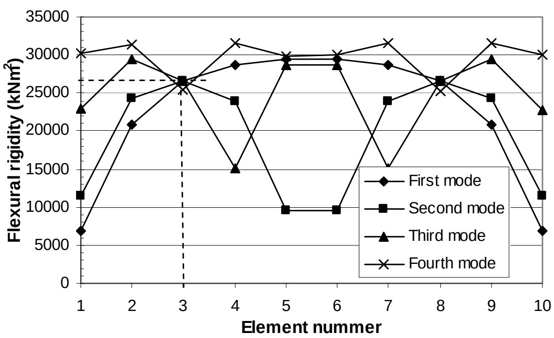

Figure 11. Flexural rigidity versus element diagram for 20% damage in 3rd element.

Similarly, Cases with damage of 20% (remaining flexural rigidity of 26660 kNm2) and 30% (remaining flexural rigidity of 23328 kNm^2) in 3rd and 5th element are shown in Figures 11-12 and Figure 13-14 respectively which indicate damage in the correct elements with a magnitude of 26500 kNm^2 (as shown in Figure 11 and Figure 12) and 23500 kNm^2 (as shown in Figure 13 and Figure 14), respectively.

It is important to note that the evaluated magnitudes of damage are quite close to the actual values.

In these studies discussed above, known degrees and locations of damages have been considered for validating

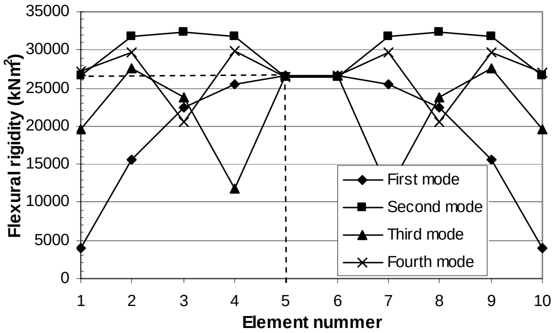

Figure 12. Flexural rigidity versus element diagram for 20% damage in 5th element.

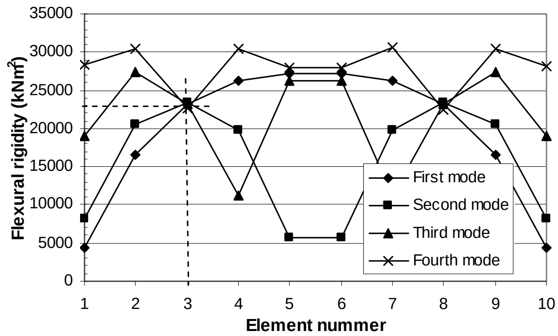

Figure 13. Flexural rigidity versus element diagram for 30% damage in 3rd element.

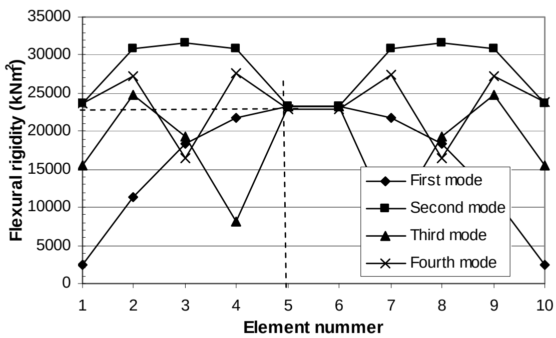

Figure 14. Flexural rigidity versus element diagram for 30% damage in 5th element.

the methodology for detection and localisation of damage. It is found that the procedure is able to identify the location and magnitude of damage. Hence, this procedure can be adopted for detection and quantification of damage of structures using measured frequencies of first few modes. In this study, the problems are selected in such a way that both strengths and limitations of the proposed methodology can be examined. From the results shown in Figures 9-14, a few observations can be made as: 1) frequency based methodology proposed in this study can be used for localisation as well as quantification of damage, 2) since, the proposed methodology is based on only frequency information, structures with symmetrical boundary condition would always show two possible locations of damage, and, 3) it is desirable to obtain the lowest measured frequency of a damaged structure with maximum possible accuracy to get an improved and more accurate estimation.

During the study, it is further observed that the proposed methodology is able to provide information about the state of damage and its location in a damaged structure, but the accuracy and reliability of the results (both localisation and quantification) also depends on correctness of information on the undamaged state. So, the proposed methodology would perform satisfactorily with a condition of availability of information (flexural rigidity) in its undamaged state. Hence, the study is further being extended to formulate a procedure which can be used for identification of damage when information about the undamaged state of a structure is not available, and it is being explored to check the efficacy and the suitable solutions (if any) for the proposed methodology with various levels of noise in modal data.

5. Concluding Remarks

The present paper addresses the methodology for detection, localisation and quantification of damage based on the formulations made using transfer matrix technique. First, the formulations and the computer program have been developed for obtaining the vibration characteristics of beam-like structures. The computer program has been validated by comparing the results of this study with those obtained using Finite Element Analysis (FEA) package. The results of this study are in good agreement with those obtained using standard FEA package. From the existing studies, it is noted that displacement mode shapes are sensitive to damage and higher modes show predominant shift in mode shape displacements due to damage in the structure. But, shift in mode shape largely depends on the location of damage and the mode considered and it is difficult to quantify damage from mode shape information. Hence, a methodology for detection, localisation and quantification of damage in structures has been proposed based on change in natural frequency obtained from transfer matrix technique. The existence of orthogonal damage in a beam structure can be simulated numerically through change in flexural rigidity (EI) in a particular beam element. For the system containing damage, an iterative procedure has been adopted by adjusting the flexural rigidity of the element such that computed frequency matches with the measured values. The location and magnitude of the damage of the structure can be identified by the intersection of the various rigidity-versus-element location curves. Studies have been presented by considering single spread-damage cases with different degrees and locations of damage to validate the accuracy, reliability and to identify the possible limitation of the proposed methodology. It is found that the proposed methodology can localise and quantify damage in a structure with considerable accuracy.

6. Acknowledgements

This paper is being published with the kind permission of the Director, Structural Engineering Research Centre, Chennai, India.

7. References

[1] J. M. Lifshitz and A. Rotem, “Determination of reinforcement unbonding of composites by a vibration technique,” Journal of Composite Materials, Vol. 3, pp. 412–423, 1969.

[2] P. Cawley and R.D. Adams, “The locations of defects in structures from measurements of natural frequencies,” Journal of Strain Analysis, Vol. 14, No. 2, pp. 49–57, 1979.

[3] W. M. West, “Illustration of the use of modal assurance criterion to detect structural changes in an orbiter test specimen,” Proceedings in Air Force Conference on Aircraft Structural Integrity, 1984.

[4] M. M. F. Yuen, “A numerical study of the eigenparameters of a damaged cantilever,” Journal of Sound and Vibration, Vol. 103, No. 3, pp. 301–310, 1985.

[5] F. Ismail, A. Ibrahim, and H.R. Martin, “Identification of fatigue cracks from vibration testing,” Journal of Sound and Vibration, Vol. 140, No. 2, pp. 305–317, 1990.

[6] P. F. Rizos, N. Aspragathos, and A.D. Dimarogonas, “Identification of crack location and magnitude in a cantilever beam from the vibration modes,” Journal of Sound and Vibration, Vol. 138, No. 3, pp. 381–388, 1990.

[7] G. Hearn, and R. G. Testa, “Modal analysis for damage detection in structures,” Journal of Structural Engineering, ASCE, Vol. 117, No. 10, pp. 3042–3063, 1991.

[8] D. Sanders, Y. I. Kim, and R.N. Stubbs, “Nondestructive evaluation of damage in composite structures using modal parameters,” Experimental Mechanics, Vol. 32, pp. 240–251, 1992.

[9] M. G. Srinivasan and C. A. Kot, “Effects of damage on the modal parameters of a cylindrical shell,” Proceedings of the 10th International Modal Analysis Conference, pp. 529–535, 1992.

[10] H. Baruh and S. Ratan, “Damage detection in flexible structures,” Journal of Sound and Vibration, Vol. 166, No. 1, pp. 21–30, 1993.

[11] G. L. Slater and S. Shelley, “Health monitoring of flexible structures using modal filter concepts,” Proceedings of the North American Conference on Smart Structures and Materials, Albuquerque, New Mexico, pp. 997–1007, 1993.

[12] Y. Narkis, “Identification of crack location in vibrating simply supported beams,” Journal of Sound and Vibration, Vol. 172, No. 4, pp. 549–558, 1994.

[13] F. K. Choy, R. Liang, and P. Xu, "Fault identification of beams on elastic foundation," Computers and Geotechnics, Vol. 17, No. 2, pp. 157–176, 1995.

[14] C. P. Ratcliffe, "Damage detection using a modified laplacian operator on mode shape data," Journal of Sound and Vibration, Vol. 204, No. 3, pp. 505–517, 1997.

[15] S. S. Law, Z. Y. Shi, and L. M. Zhang, "Structural damage detection from incomplete and noisy modal test data," Journal of Engineering Mechanics, ASCE, Vol. 124, No. 11, pp. 1280–1288, 1998.

[16] Z. Y. Shi, S. S. Law, and L. M. Zhang, "Damage localization by directly using incomplete mode shapes," Journal of Engineering Mechanics, ASCE, Vol. 126, No. 6, pp. 656–660, 2000.

[17] M. A.-B. Abdo and M. Hori, "A numerical study of structural damage detection using changes in the rotation of mode shapes," Journal of Sound and Vibration, Vol. 251, No. 2, pp. 227–239, 2002.

[18] D. Wu and S. S. Law, "Damage localization in plate structures from uniform load surface curvature," Journal of Sound and Vibration, Vol. 276**,** No. 1–2, pp. 227–244, 2004.

[19] M. K. Yoon, D. Heider, J. W. Gillespie, C. P. Ratcliffe, and R. M. Crane, "Local damage detection using the two-dimensional gapped smoothing method," Journal of Sound and Vibration, Vol. 279, No. 1–2, pp. 119–139, 2004.

[20] A. Alvandi and C. Cremona, "Assessment of vibration-based damage identification techniques," Journal of Sound and Vibration, Vol. 292, No. 1–2, pp. 179–202, 2006.

[21] S. Sasmal, K. Ramanjaneyulu, and N. Lakshmanan, "Transfer matrix method for identification of damage in structures using vibration characteristics," SERC Research Report, No. RCS-RCS-MLP10741-RR-2005-2, 2005.

[22] V. Srinivas, S. Sasmal, and K. Ramanjaneyulu, "Studies on methodological developments in structural damage identification," Structural Durability and Health Monitoring, Vol. 5, No. 2, pp. 133–160, 2009.

[23] E. G. Pestel and F. A. Leckie, Matrix Methods in Elasto-Mechanics, McGraw Hill Book Company Inc., New York, 1963.

Engineering, 2009, 1, 177-187
doi:10.4236/eng.2009.13021 Published Online November 2009 (http://www.scirp.org/journal/eng).

Condition-Based Diagnostic Approach for Predicting the Maintenance Requirements of Machinery

C. I. UGECHI[1], E. A. OGBONNAYA[2], M. T. LILLY[1], S. O. T. OGAJI[3*], S. D. PROBERT[3]
[1]*Department of Mechanical Engineering, Rivers State University of Science and Technology, Port Harcourt, Nigeria*
[2]*Department of Marine Engineering, Rivers State University of Science and Technology, Port Harcourt, Nigeria*
[3]*School of Engineering, Cranfield University, Bedfordshire, U K*
E-mail: *yagangzhang@gmail.com*
Received January 10, 2009; *revised February* 21, 2009; *accepted February* 23, 2009

Abstract

Wise maintenance-procedures are essential for achieving high industrial productivities and low energy expenditure. A major part of the energy used in any production process is expended during the maintenance of the employed equipment. To ensure plant reliability and equipment availability, a condition-based maintenance policy has been developed in this investigation. In particular, this project explored the use of vibration parameters in the diagnosis of equipment failure. A computer-based diagnostic tool employing an artificial neural-network (ANN) was developed to analyse the ensuing machinery faults, their causes and consequences. For various categories of this type of machinery, a vibration-severity chart (ISO 12372 / BS 4675: 1971) appropriately colour coded according to defined mechanical faults, was used in training of the ANN. The model was validated using data obtained from a centrifugal pump on full load and fed into the program written in Visual Basic. The results revealed that, for centrifugal pumps within 15 to 300kw power range, vibration-velocity amplitude of between 0.9 and 2.7mm/s was within acceptable limits. When the values rose to between 2.8 and 7.0mm/s, closer monitoring and improved understanding of the equipment condition was needed. The evolved diagnostic and prognostic model is applicable for other rotary equipment that is used within the same power limits.

Keywords: Condition Based, Diagnostic Model, Predictive Maintenance, Machinery, Centrifugal Pumps

1. The Challenge

Maintenance, although requiring the expenditure of significant amounts of energy, is usually required in order to keep (or restore) facilities at an acceptable operational standard [1]. For most plants, maintenance practice is predominantly based on routine-scheduled prevention as well as previously unanticipated reactions to overcome faults. Predictive maintenance (PdM) procedures, such as that devised in this project, are evolving and results in less wasted effort. According to Ogbonnaya [2], Contreras *et al*. [3] and Salva *et al*. [4] condition monitoring (CM) an aspect of PdM is defined as the use of appropriate technologies to determine the operational state of the considered machinery. For instance, it may involve vibration measurements, infrared thermography, and/or oil analyses etc.

For decades, conventional wisdom suggested that the best way to optimise the performance of physical assets was to overhaul or replace them at fixed interval (PM). This was based on the premise that there is a direct relationship between the amount of time (or number of cycles) equipment spends in service and the likelihood that it will fail. Moubray [5], stated that this relationship between running time (age) and failure is true for some failure modes, but that it is no longer very productive as equipment are now much more complex than it was even fifteen years ago. He pointed out that fixed interval overhaul ignores the fact that overhauls are extraordinarily invasive undertakings that massively upset stable systems. As such, they are likely to induce infant mortality, and so cause the very failure, which they seek to prevent.

This has led to startling changes in the patterns of equipment failure. Unless there is a dominant age-related failure mode, fixed interval overhauls or replacements do little or nothing to improve the reliability of rotary equipment [5]. There is no gain in overhauling a machine that has nothing wrong with it [6]. Moubray [5] concluded that “in the absence of any evidence to the contrary, it is more realistic to develop maintenance strategies which will assume that equipment failure can occur at any time and not at fixed amount of time in service”.

2. Maintenance Management

Direct on-line real-time continual monitoring and analysis of machinery behavior is the most reliable way to achieve a high productivity [3]. If an abnormal situation can be detected early, when defects are minor and have not affected machine output, with the cause of the fault diagnosed while the machine is still running, then the downtime for associated repairs can be reduced and other attendant advantages achieved.

Figure 1 shows the various maintenance methods/ techniques/strategies. Reactive maintenance is usually only implemented following an unforeseen event leading to a partial or total failure of the system. Preventive maintenance (PM) is initiated according to a predetermined time-schedule in order to try to avoid the occurrence of failure. Predictive maintenance (PdM) is laun- ched as a result of behaviour of the equipment/ machinery before total failure, whereas proactive maintenance may require redesigning and/or modification of the adopted maintenance-procedure where necessary.

Each of these techniques has merits and frailties, but PdM is the most advantageous [7]; it combines the advantages of preventive and proactive strategies. Its basic

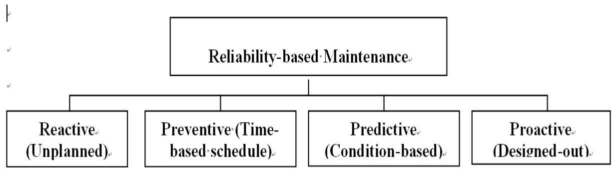

Figure 1. Maintenance procedures.

concept is shown in Figure 2. Predictive maintenance is summarized as involving actions taken to improve one or more of the following machinery characteristics: availability, reliability, maintainability, safety, efficiency etc as well as reduce energy waste and environmental pollution [4]. As a result, the implementation of PdM usually enables one to have sufficient lead-time to plan, schedule and make necessary repairs before the equipment would otherwise fail. So major breakdowns and costly downtime can then be avoided.

2.1. Condition Monitoring

This has long been practiced by maintenance personnel who relied on their innate senses of hearing, touch and sight, but the judgment and conclusions were often not reliable. All physical structures and machinery, that are associated with rotating components, give rise to vibration. The vibrations so generated by machinery have become a well-utilized parameter for assessment in CM. It is one of the most versatile techniques, which is capable of detecting about 70% of common mechanical faults associated with rotating machinery [6].

Machinery vibrations are complex, but can be measured, processed and their interpretation simplified in order to facilitate the implementation of recommended action [8]. According to Okah-Avae [9], rotating machinery produce vibration patterns, which repeat periodically and so have been found to be amenable to analysis.

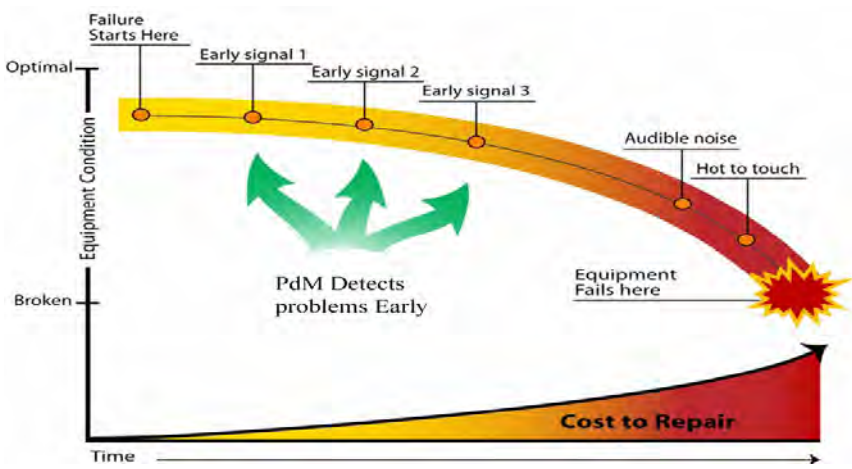

Figure 2. Basic behaviour of a failing system (machinery) [5].

2.2. Vibration Monitoring and Analysis

Even though the wise maintenance of industrial equipment may require the monitoring of additional parameters, such as temperature, pressure, flow, voltage, electric current, horsepower, torque, etc, vibration data usually contain more information about a machine's health and operating characteristics than any other parameter – see Table 1. This informed the choice of vibration monitoring and analysis over other condition monitoring techniques in this research.

Measurements of vibration parameters are important in many industrial applications. The parameters desired may be displacement, velocity, or acceleration; in time or frequency domain. These quantities are useful in predicting the fatigue failure of a particular component of machine and play important role in analysis, which are used to reduce equipment vibration [8]. According to Ralph [10], when measurement of both amplitude and frequency are available, diagnostic methods can be used to determine the magnitude of a problem and its probable cause.

Vibration severity is a function of displacement and frequency of rotation of the component. Measurements of vibration-velocity take into account both displacement and frequency: "vibration-velocity amplitude is a direct measure of vibration severity" [11]. Vibration-velocity gives an indication of vibration severity over a wide range of frequencies and hence is extensively applied in condition monitoring [9].

Each mechanical defect generates vibration in its own unique way [11]. This makes it possible to identify a mechanical problem by measuring and noting its vibration signature. When vibration measurements and analysis are performed systematically and intelligently, they will not only allow determination of machine health but also permit the prediction of the mechanical fault and when such condition most likely will have reached unacceptable levels [12].

Vibrations occurring in the 600 to 60,000 cpm frequency range are generally described and measured by their vibration-velocity amplitudes [11]. In practice, the following relationships apply:

Displacement of vibrating component

$$(x) = a / (2\pi f)^2 \tag{1}$$

Velocity of vibrating component

$$(v) = a / 2\pi f \tag{2}$$

Acceleration of vibrating component

$$(a) = 2\pi f v \tag{3}$$

3. Research Methodology

The identification of incipient faults in a machine, in order to diagnose an impending problem and locate the fault while the machine is still running, through an interpretation of its unique vibration characteristic (i.e. signature) is the main aim of PdM [13]. A good vibration survey program sets different limits for different machines, as well as different limits for different regions of the frequency domain spectra for the same machine.

The delineation of severity limits for good and bad bearing conditions are best determined by "comparison" or "trending" methods [11]. In establishing a program for checking the spike energy conditions of rolling element bearings; a "comparison method is used. The spike energy levels of similar machines are measured and any level which significantly departs from the average are singled out for further analysis of potential bearing problems. This method has led to the establishment of criteria levels which distinguished good and bad bearings.

Table 1. Parameters indicating the occurrence of faulty conditions in a rotating machine.

PARAMETER MEASURED → / DETECTED CONDITION ↓	TEMPERTURE OF MACHINE	PRESSURE OF PROCESS FLUID	FLOW OF FLUID	OIL ANALYSIS	SPIKE ENERGY OF BEARING	VIBRATION OF MACHINE
OUT- OF - BALANCE						X
MISALIGNMENT	X					X
BENT SHAFT	X					X
BALL-BEARING DAMAGE	X			X	X	X
JOURNAL-BEARING DAMAGE	X	X	X	X		X
GEAR DAMAGE				X		X
MECHANICAL LOOSENESS						X
MECHANICAL RUBBING					X	X
NOISE						X
CRACKING						X

Various ranges of vibration velocity amplitude and spike energy were represented with colour codes for corresponding level of vibration severity: green for good/normal condition, blue for acceptable condition, yellow for fair condition/ improvement required, and red for unacceptable condition. The use of a real-time recurrent simulation was therefore adopted in this investigation in order to develop an artificial neural-network (ANN) for the analysis of the vibration data [4].

3.1. Artificial Neural-Networks (Anns)

Ogbonnaya [8] showed that ANN is a promising tool to articulate and analyze the numerous data associated with catastrophic failures in rotating machinery. According to Agbese and Mohammed [14], since ANN, a branch of Artificial Intelligence (AI), are modelled after the biological neurons of the human brain, they hold considerable promise as building blocks in actualising the ultimate aim of AI systems. Out of the various architecture with which ANN is conveyed; the back propagation algorithm has proved most promising and accurate for analyzing machine vibration data [8]. Also of important is training the neuron of the network on the basis of pattern recognition; especially when there are large amount of data to handle.

Simulated neural networks are software models designed through suitable interpretation of the structure and basic function of the biological neuron of the human brain. Therefore the more physiology of the brain is understood the better the ability to design ANNs that will handle more complex problems. According to Carlton *et al* [15]; Agbese and Mohammed [14], the artificial neuron is called the processing elements or nodes, which are capable of handling information in response to external input. It has many input parts and combines the input

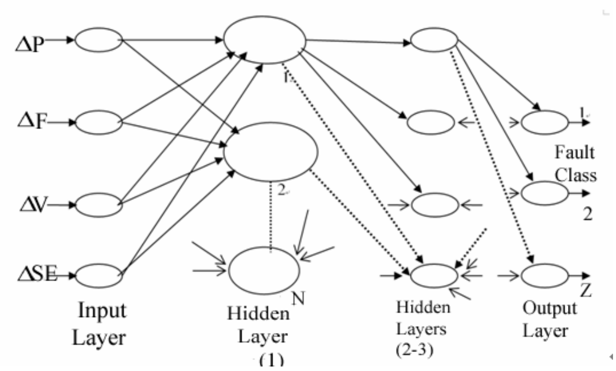

Legend: ΔP – change in active power of driver; ΔF – change in equipment's frequency; ΔV – change in equipment's vibration-amplitude; ΔSE – change in spike energy of bearing

Figure 3. Triple hidden-layer network.

values it receives usually by summation. The combined input is then modified by a transfer function, which can be chosen to suit a particular application. This new value becomes the output and can be connected to the inputs of other processing elements through weighting functions, which correspond to the synaptic strength of biological neural connection [15,16].

As in the biological brain, the neural network learns by altering the value of its weights. In a simulated neural network, the weights are altered as to reduce the error between the outputs the network produces in relation to a particular input pattern and the actual required outputs [15]. This is an iterative process, carried out as the patterns to be learnt are presented; an algorithm calculates the error and changes the value of the weights accordingly.

Typically, an engineering application of ANN technology consists of a set of input nodes that forms the input layer and one or more hidden layers. This type of ANN is called a multilayer perceptron, and usually a popular back-propagation algorithm is used to train the network [17].

The triple-hidden layer ANN shown in Figure 3 was designed with 4 nodes in the input layer. Hidden layer 1 is to be used for processing of the measured values; the summation is then passed to hidden layer 2 for exact fault-classification, while hidden layer 3 is designed to issue task specifications for achieving possible solutions. The output layer is therefore able to determine and display the nature of the exact fault and provide a solution for the fault to be overcome, thereby optimizing the use of energy and human resources.

A vibration-severity chart for various classes of machinery, as illustrated in Table 2, was used in the training of the network. Its inputs were vibration-velocity amplitude, motor power, equipment frequency and spike energy of the equipment. A computer program in Visual Basic (VB) was developed from the flowchart shown in Appendix 1. Further details of it are available from the authors. The faults considered included misalignment, imbalance, bent shaft, mechanical looseness, and poor-bearing condition.

The diagnostic model is programmed according to various colour codes for corresponding pump conditions, diagnosed faults and appropriate task instructions on how to avert catastrophic failure of the vibrating equipment (in the considered case, a pump). The software flagged up defined information once the vibration values were within a specified range. The solutions obtained from the diagnostic model were used to determine how unwanted vibration problems could be eliminated or reduced to allowable limits.

When analysing vibration severity of a machine to pinpoint particular problem, it is essential to know the

Table 2. Ranges of vibration severity for various classes of machinery (iso 12372 or bs 4675: 1971).

<table>
<tr><th colspan="2">Range of Vibration Severity</th><th colspan="2">Maximum Values</th><th colspan="4" rowspan="2">Class of Vibration of Machine</th></tr>
<tr><th rowspan="2">Range Classification</th><th rowspan="2">Effective Velocity: RMS (mm/s)</th><th rowspan="2">Vibration Velocity (mm/s)</th><th rowspan="2">Vibration Displacement (μm)</th></tr>
<tr><th>Class I</th><th>Class II</th><th>Class III</th><th>Class IV</th></tr>
<tr><td>0.28</td><td>0.28</td><td>0.4</td><td>1.25</td><td rowspan="3">Good</td><td rowspan="4">Good</td><td rowspan="5">Good</td><td rowspan="6">Good</td></tr>
<tr><td>0.45</td><td>0.45</td><td>0.63</td><td>2</td></tr>
<tr><td>0.71</td><td>0.71</td><td>1.0</td><td>3.15</td></tr>
<tr><td>1.12</td><td>1.12</td><td>1.6</td><td>5</td><td rowspan="2">Acceptable / Allowable</td></tr>
<tr><td>1.8</td><td>1.8</td><td>2.5</td><td>8</td><td rowspan="2">Acceptable / Allowable</td></tr>
<tr><td>2.8</td><td>2.8</td><td>4.0</td><td>12.5</td><td rowspan="2">Improvement Required</td><td rowspan="2">Acceptable / Allowable</td></tr>
<tr><td>4.5</td><td>4.5</td><td>6.3</td><td>20</td><td rowspan="2">Improvement Required</td><td rowspan="2">Acceptable / Allowable</td></tr>
<tr><td>7.1</td><td>7.1</td><td>10</td><td>31.5</td><td rowspan="6">Not Acceptable</td><td rowspan="2">Improvement Required</td></tr>
<tr><td>11.2</td><td>11.2</td><td>16</td><td>50</td><td rowspan="5">Not Acceptable</td><td rowspan="2">Improvement Required</td></tr>
<tr><td>18.0</td><td>18</td><td>25</td><td>80</td><td rowspan="4">Not Acceptable</td></tr>
<tr><td>28.0</td><td>28</td><td>40</td><td>125</td><td rowspan="3">Not Acceptable</td></tr>
<tr><td>45.0</td><td>45</td><td>63</td><td>200</td></tr>
<tr><td>71.0</td><td></td><td></td><td></td></tr>
</table>

Legend:
Class I: Small machines; electric motors up to 15kW power.
Class II: Medium-size machines; electric motors of 15 to 300kW power.
Class III: Large prime-movers or machines on rigid foundations; electric motors of above 300kW power.
Class IV: Large prime-movers and other machines, Turbo Machines.
Good: Colour coded green.
Acceptable/Allowable: Colour coded blue.
Improvement Required: Colour coded yellow.
Not Acceptable: Colour coded red.

vibration frequency. Knowing the frequency helps in identifying the exact nature of the problem and the location of the faulty machine-component. Although all of the frequencies in a complex vibration signal can be of concern for analyzing machinery problems, the *fundamental and dominant* frequencies are of special importance. The fundamental frequency is equal to the speed of rotation of the rotating element – *first harmonic* (1* RPM). The dominant frequency is the frequency at which the largest vibration amplitude occurs. The fundamental and the dominant frequencies are not always the same. Where the dominant frequency differs from 1* RPM (fundamental frequency), the dominant frequency is usually more indicative of the trouble.

Therefore, during the analysis of the vibration data, interest was devoted primarily to measuring the dominant vibration amplitudes and determining the frequencies at which they occurred. This helped in the identification of the problem and isolation of the faulty machine component. High vibration amplitudes occurring at integral multiples of the machine's fundamental frequency (e.g. 2* RPM, 3* RPM, 4* RPM, etc.) are associated to different failure modes.

3.2. Instrumentation

In undertaking this investigation, the following instruments were used: Vibration Data Collector (Model: IRD 880); Vibration Pick-Up Pen / Ear Piece; Laser Alignment Tools; Balancing Machine; Strobe Light; and a Computer System.

The vibration analyser performs the function of meters

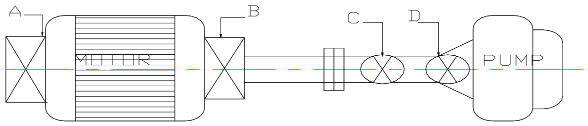

Legend: → = Measurement Locations/Points, i.e. A, B, C and D
✕ = Plain bearing
⊗ = Anti-friction bearing

Figure 4. The tested pump assembly and location measuring points.

and monitors, and is capable of carrying out more complex operations. Vibration meters, monitors and analysers, uses vibration transducers. This is often referred to as vibration sensors or pick-up. The heart of the measurement system is the transducer; it is a sensing device which converts one form of energy to another. The vibration transducer converts mechanical vibration energy into electrical signal. The sensitivity of a velocity transducer is constant over a wide range of operating frequencies [11], but there are few limitations, which are above the scope of this work. The data collector is used in acquiring vibration-velocity, spike energy at variable frequencies. The rated power and frequency of the driver are used in the analysis as power at full load and fundamental frequencies. The data were collected manually and fed into the computer model for analysis.

4. Results and Discussions

Interpretation of the field-vibration data and the subsequent diagnosis of the failure mode, constituted the most difficult tasks in running the vibration-based program. Much depended on the experience and skill of the analyst. In undertaking maintenance, the need to avoid costly mistakes, minimize energy expenditure and achieve the benefits of PdM, led to the model developed for this investigation.

Vibration-velocity data, presented as root means square (RMS) values were collected, with the pump at full load - see Figure 4 and Table 3. The numerical values in Table 3 and trends on the associated graphs in Figure 5 displayed high axial and radial vibrations at locations D_7 and $\mathbf{C}_5$ respectively, suffered by the pump bearings. Bearings A and B (see Figure 4) for the electric motor also experienced significant vibrations; although of lower amplitudes. Significant vibrations of the motor bearings could be transmitted through the shaft from bearings C and D. Points A to D shown on Table 3 are the location points where vibration values were taken, while positions 1 to 8 represent the sequence in which data were collected on the same equipment at different frequencies.

Results of the analysis of data presented in Table 3 using the software model were displayed on the computer screen as in Figure 6. This indicated significant vibration amplitudes (depicted by the red and yellow colours). The program then proceeded to the second phase of the analysis in order to reveal the fault classifycations and task instructions, as shown in Figure 7. The analysis indicated the presence of high axial and radial vibrations at 1RPM, 2RPM, and 3RPM, which suggests misalignment, while the high spike energy at B was indicative of a defective bearing.

The misalignment originating at the driven end of the pump assembly was seen as the source of the failure because the vibration amplitude was largest there. The misaligned shaft and bearings at C and D led to the damage of the bearing at B

Table 3. Vibration-analysis data sheet for unit 1800-01A pump.

						PUMP MAKE: GIABBIONETA	
						POWER: 36.5kW	
						RPM: 2950 / 2945	
						DATE: 09/10/06	
						ANALYZER MODEL: IRD 880	
MS/L	MS/S	Frequency cpm	Velocity (VH) mm /sec (RMS)	Velocity (VV) mm/sec (RMS)	Velocity (VA) mm/sec (RMS)	Spike Energy g-SE	Multiple of Fundametal Frequency (cpm/2950)
C	**5**	3,012	8.2	1.1	1.0	0.0967	1 * RPM
D	**7**	3,066	4.7	1.6	9.8	0.076	1 * RPM
B	**3**	3,834	3.7	1.1	1.3	0.557	1 * rpm
A	**1**	5,946	7.5	0.9	1.2	0.094	2 * rpm
D	**8**	8,007	3.0	2.7	0.9	0.1117	3 * rpm
C	**6**	12,730	1.9	3.6	1.1	0.1313	4 * rpm
A	**2**	13,686	1.9	1.1	1.3	0.097	5 * rpm
B	**4**	33,676	2.0	1.0	1.6	1.38	11 * rpm

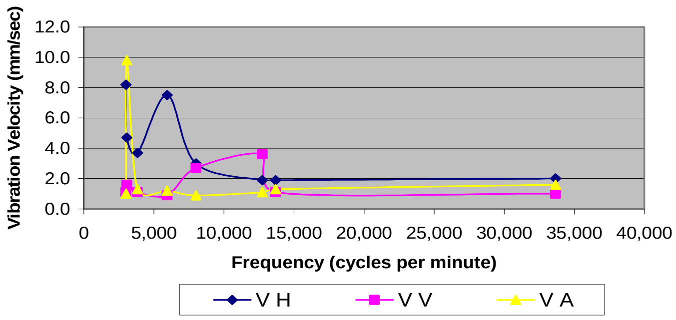

Figure 5. Vibration velocities for the 1800-01A pump.

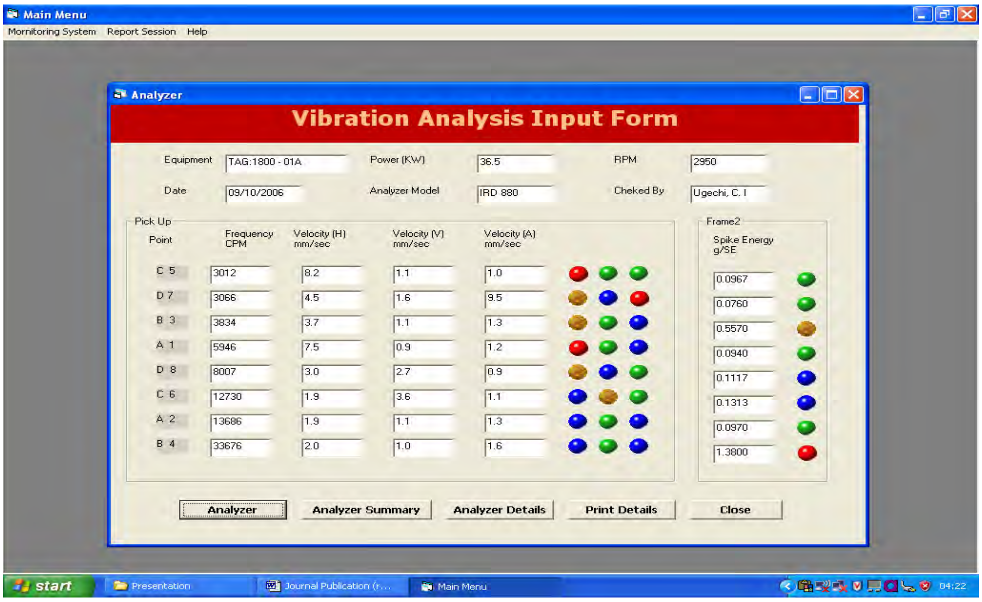

Figure 6. Computer screen presentation for1st phase of the analysis.

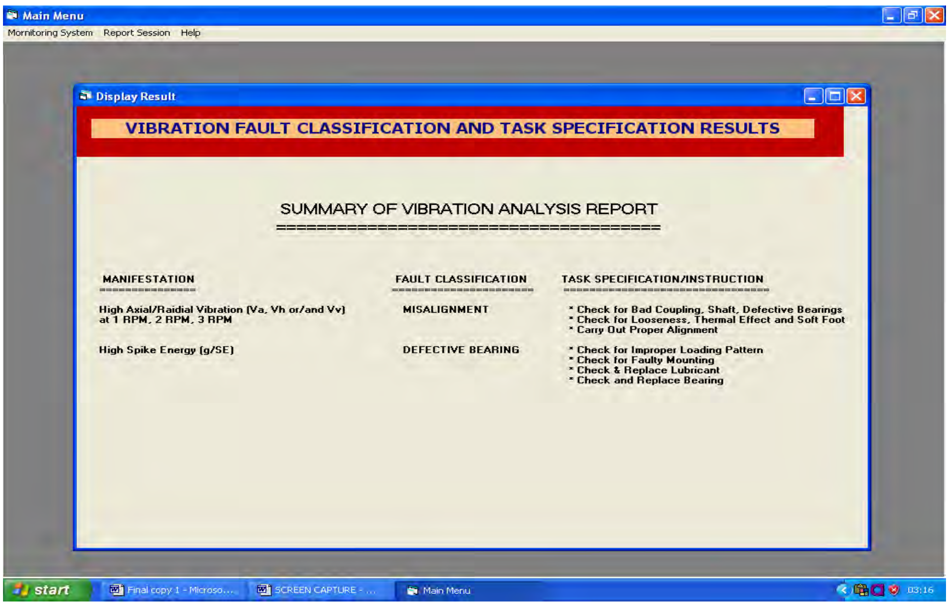

Figure 7. Computer screen presentation for 2nd phase of the analysis.

Table 4. Vibration-analysis data sheet for unit 1800-01A pump (AFE).

							PUMP MAKE: GIABBIONETA POWER: 36.5kW RPM: 2950 / 2945 DATE: 17/10/06 ANALYZER MODEL: IRD 880
MS/L	MS/S	Frequency cpm	Velocity (VH) mm /sec (RMS)	Velocity (VV) mm/sec (RMS)	Velocity (VA) mm/sec (RMS)	Spike Energy g-SE	Multiple of Fundametal Frequency (cpm/2950)
A	**1**	1,500	2.5	2.6	1.3	0.07	0.5*RPM
B	**2**	2,945	2.4	2.1	1.3	0.117	1 * RPM
B	**3**	6,020	2.6	2.3	1.5	0.11	2 * RPM
C	**4**	9,000	2.3	2.3	1.2	0.15	3 * RPM
D	**5**	12,200	2.3	2.6	1.1	0.04	4 * RPM
D	**6**	15,170	2.4	2.6	1.1	0.43	5 * RPM

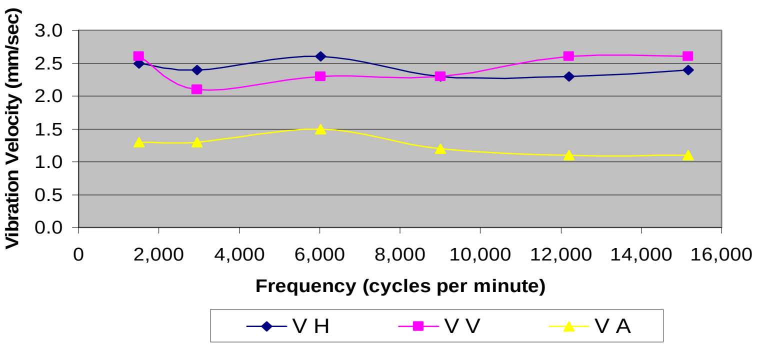

Figure 8. Vibration velocities for the 1800-01A pump (AFE).

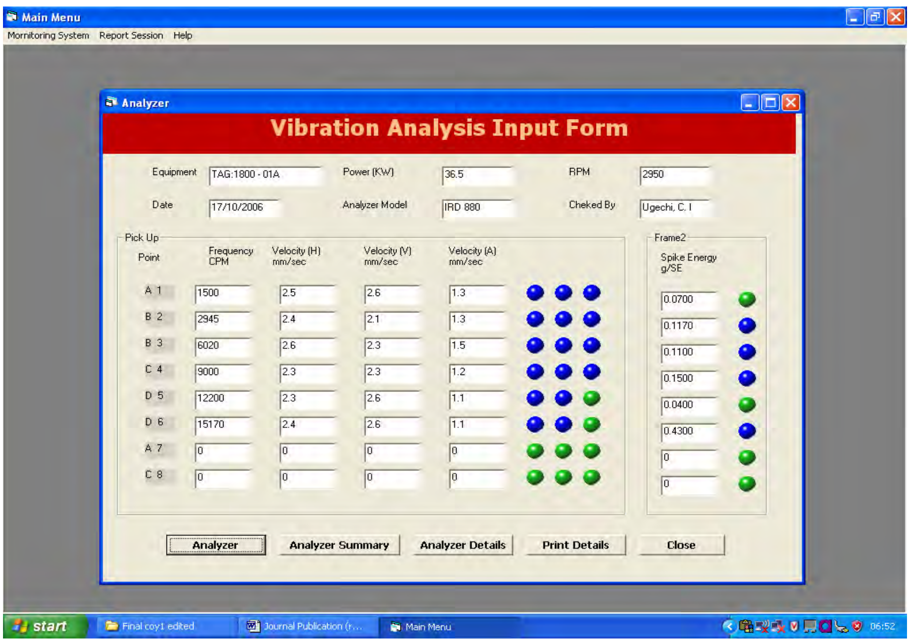

Figure 9. Computer screen presentation for the analysis after fault elimination (AFE).

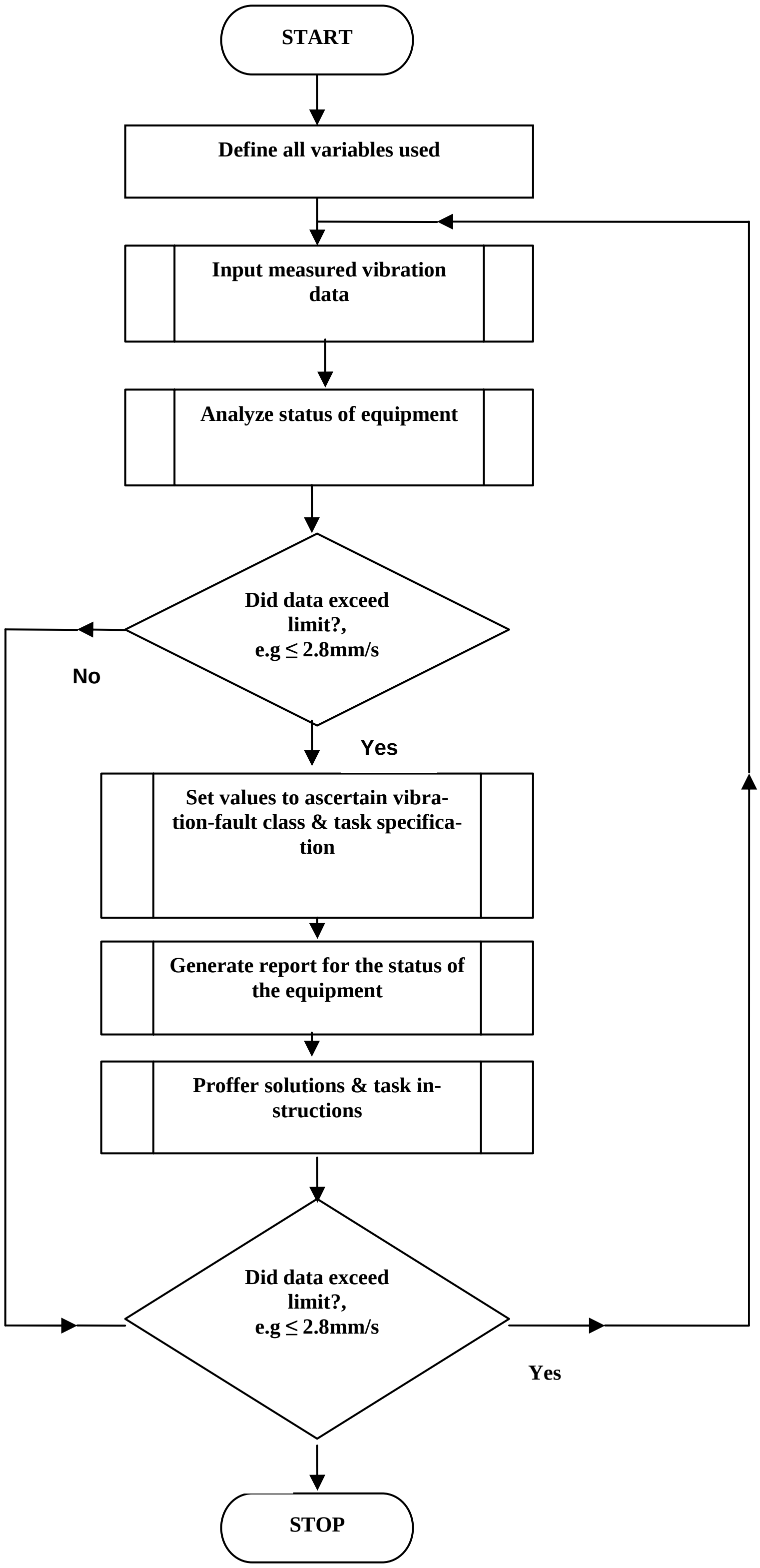

Appendix 1. predictive maintenance program flow-chart.

The task instructions were executed and the data collected after the fault elimination shown in Table 4. The associated graph (i.e. Figure 8) showed almost smooth trends with a maximum of 2.6mm/sec radial vibration velocity amplitude and 1.5mm/sec amplitude in the axial direction, which suggested an acceptable working condition, had been achieved.

Results of the analysis of these data are shown in Figure 9 and confirmed that the condition of the pump was within acceptable range. This is evident in the displayed green and blue colours. Therefore the program did not proceed to a second phase of the analysis. Also comparing the data in Table 4 with specified maximum vibration-level of 3.0mm/sec for the pump, as recommended by the manufacturer, showed that the vibration values were within the acceptable range.

5. Conclusions

A diagnostic condition-based model that can be used for the PdM of rotary equipment has evolved from this study. The complexities involved in the analysis of vibration data have been simplified for the vibration analyst and PDM personnel. The high level of human error associated with the analysis of vibration data could also be reduced through this procedure. Faults of the rotating machine, identified through this analysis of its vibration characteristics, can be displayed numerately and graphically.

The results obtained from the model, which was developed using an ANN, revealed that the approach is well suited to the diagnosis of vibration-based faults in centrifugal pumps. Though the model was validated using vibration data obtained from a centrifugal pump, it can be used to analyze vibration faults in other categories of rotating equipment. The model can also therefore be used for continuous real-time on-line condition monitoring.

6. References

[1] L. R. Higgins, "Maintenance engineering handbook," McGraw-Hill Book Company, New York, USA, pp. 22–35, 1995.

[2] E. A. Ogbonnaya, "Condition monitoring of a diesel engine for electricity generation," M. Tech. Thesis, Department of Marine Engineering, Rivers State University of Science and Technology, Port Harcourt, Nigeria, p. 68, 1998.

[3] L. R. Contreras, C. Modi, and A. Pennathur, "Integrating simulation modelling and equipment condition diagnostics for predictive maintenance strategies–A case study," Proceedings of the 2002 Winter Simulation Conference, University of Texas, El Paso, USA, pp. 1–7, 2002.

[4] M, Salva, R. Hernandez, and C. Sanz, "Proposed of a method for implementing infrared-scanning inspection programs in merchant vessels," Marine Technology and Sname News, Vol. 41, No. 1, pp. 1–6, 2004.

[5] J. M.Moubray, "Maintenance management: A new paradigm, strategic technologies," Inc., Aladon Ltd, UK, pp. 7–11, 2000. [Online] Available: http://www.maintenanceresources.com/RCM/Maintparadigm, July 29, 2006.

[6] A. Veltkamp, "Vibration introduction course: SKF condition monitoring, in computerized maintenance management system and enterprise resource planning," Nigerian Society of Engineers, Lagos, Nigeria, pp. 1.1–4.5, 2001.

[7] S. Jeff, PDM, "Secrets revealed: How to improve your PDM program or start one from scratch," 1st Edition, Allied Reliability, Inc., Tulsa, Oklohoma, [Online] Available: http://www.alliedreliability.com, pp. 4–35, June 6, 2006.

[8] E. A. Ogbonnaya, "Modelling vibration-Basic faults in rotor shafts of a gas turbine," PhD Thesis, Department of Marine Engineering, Rivers State University of Science and Technology, Port Harcourt, Nigeria, p. 251, 2004.

[9] B. E. Okah-Avae, "The science of industrial machinery and systems maintenance," Spectrum Books Ltd, Lagos, Nigeria, pp. 19–105, 1996.

[10] W. P. P. Ralph, "Maintenance management and control," in Handbook of Industrial Engineering: Technology and Operations Management, 3rd Ed., Inc. New York, USA, pp. 1611–1615, 2001.

[11] IRD Mechanalysis, "Vibration monitoring and analysis handbook," IRD Mechanalysis, Inc., Columbus, USA, pp. 1.7–5.7, 1993.

[12] J. T. Broch, "Mechanical vibration and shock measurement," 2nd Ed., K. Larsen & Son A/S, Denmark, pp. 197–199, 1980.

[13] K. A. Oladejo and A. O. Oke, "Condition monitoring of a centrifugal pump," in Pump Maintenance, Arcedem Seminar Paper, Ibadan, Nigeria, pp. 6–10, 2005.

[14] E. P. Agbese and A. Mohammed, "Artificial neural network and their applications," Proceedings of First National Conference of the Department of Mechanical Engineering on Manufacturing Technology and Engineering in a Developing Economy, University of Uyo, Nigeria, May 2–3, pp 51–55, 2001.

[15] J. S. Carlton, C. G. Holland, M. J. Newbury, D. Rhoden, and D. A. Triner, "Recent operational experience and research relating to marine machinery condition monitoring," Trans IMarE, Vol. 109, No. 1, pp. 75–95, 1997.

[16] E. A. Ogbonnaya, K. D. H. Bob-Mannual, I. E. Douglas, and H. I. Hart, "Application of artificial neural networks to gas turbine rotor shaft faults diagnosis," Journal of Science and Technology Research, Vol. 3, No. 1, pp. 12–15, 2004.

[17] K. Farhad, A. P. Mehmet, and M. Ehsan, "A new generation motion-control system for twin-hull vessels using a neural optimal controller," Marine Technology and Sname News, Vol. 40, No. 3, pp. 168–180, 2003.

Appendix

Abbreviations and Nomenclature

AFE After fault elimination
AI Artificial Intelligence
ANN Artificial neural-network
a vibration acceleration
BS British Standard
CM Condition monitoring
cpm Cycles per minute
f vibration frequency
G Large machines having electric motors of above 300kW power
g-SE Unit of spike energy
ISO International Standards Organization
K Small machines having electric motors of up to 15kW power
M Medium machines having electric motors of between 15 and 300kW power
MS/L Measurement location
MS/S Measurement sequence
N Number of hidden layers
PdM Predictive maintenance
PM Preventive maintenance
RMS Root mean square
RPM Revolutions per minute
T Turbo machines
VA Vibration velocity in axial direction (mm/sec)
VB Visual Basic
VH Vibration velocity in horizontal direction (mm/sec)
VV Vibration velocity in vertical direction (mm/sec)
v vibration velocity (mm/sec)
x vibration displacement (mm)
Z Number of output layers
ΔF Change in vibration frequency
ΔP Change in active power
ΔSE Change in equipment spike energy
ΔV Change in vibration velocity amplitude
μm Micrometre

Glossary:

Dominant frequency: Frequency at which the largest vibration-amplitude occurs.
Field vibration-data: Measured vibration data collected from running machines.
Fundamental frequency: Basic repetition of the rotating equipment; i. e. the first harmonic.

Engineering, **2009, 1, 188-195**
doi:10.4236/eng.2009.13022 Published Online November 2009 (http://www.scirp.org/journal/eng).

Energy Analysis of Pid Controlled Heat Pump Dryer

Ilhan CEYLAN
Mechanical Education Department, Technical Education Faculty, Karabuk University, Karabuk, Turkey
E-mail: *ilhancey@gmail.com*
Received September 2, 2009; *revised September* 18, 2009; *accepted September* 23, 2009

Abstract

In this experimental study, a heat pump dryer was designed and manufactured, in which drying air temperature was controlled PID. Manufactured heat pump dryer was tested in drying kiwi, avocado and banana from among tropical fruits and energy and exergy analyses were made. Drying air temperature changed between 40 ^{o}C - 40.2 ^{o}C while drying the tropical fruits. Before the drying process in heat pump dryer, initial moisture contents were determined as 4.31 g water / g dry matter for kiwi, 1.51 g water / g dry matter for avocado and 4.71 g water / g dry matter for banana. Then tropical fruits were dried separately in heat pump dryer. Drying air temperature was kept unchanged with the error of +0.2 ^{o}C. Drying air velocity changed between 0.3 and 0.4 m/s in a period of 310 min. COP_{ws} of the heat pump dryer was calculated as 2.49 for kiwi, 2.47 for banana and 2.41 for avocado during the experiments. EUR changed between 13 % and 28 % for kiwi, 18% and 33% for avocado and 13% and 42% for banana in heat pump dryer.

Keywords: Tropical Fruit, Drying, Heat Pump Dryer, PID Control

1. Introduction

Drying is extracting liquids in a matter. In technical drying, external interference is applied to the drying process and the moisture in the matter is extracted through various methods. Thus, drying is described as the reduction of product moisture to the required dryness values at a definite process. All of the units that enable the product to reach the drying values at the definite process and which consist of various units (heating, dehumidifying) are described as the drying system [1].

The systems used at the drying process are applied at many industrial branches (such as food, paper, cement, timber and chemistry). The drying applied to the foodstuff serves a number of aims, the most important of which is to prevent the product from breaking down during the long storage. During the long storage, the drying process helps product remain without breaking down by reducing the moisture of the product to the level, which is enough to limit microbial development or other reactions. Besides, with the reduction of the moisture content, the conservation of the characterizations of quality such as the value of aroma and food is realized. The other aim of drying process is to reduce the product volume, thus increasing the efficiency during the storage and transportation of the essential components of the foodstuff.

In the literature, there are a lot of studies about heat pump drying systems. However, there have been no studies interested in PID controlled heat pump dryer. In this study, the energy balance of PID controlled heat pump dryer has been achieved successfully. The purpose of this paper is an understanding of energy and exergy analysis of PID controlled heat pump dryer. With the PID control over drying air temperature in the dryer the tropical fruits such as kiwi, avocado and banana were dried.

Fatouh *et al*. dried herbs using a heat pump dryer [2]. Ogura *et al*. made energy and cost estimation for application of chemical heat pump dryer [3]. Queiroz *et al*. determined the drying kinetics of tomato by using electric resistance and heat pump dryers [4]. Chua and Chou made performance analysis two stage heat pump system for drying [5]. Achariyaviriya *et al.* presented mathematical model development and simulation of heat pump fruit dryer [6]. Chua *et al*. investigated recent developments and future trends for heat pump drying [7]. Hawlader *et al*. used a different drying method by using a heat pump dryer for the drying of guava and papaya [8].

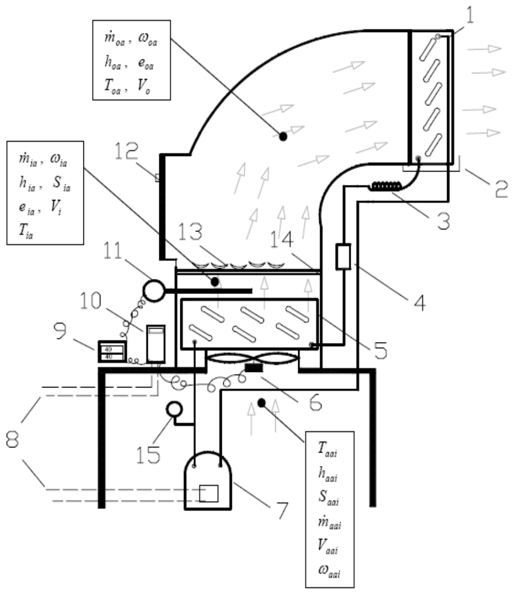

1. Evaporator 2. Condensated water 3. Capillary tube 4. Dryer filter 5. Condenser 6. Axial fan 7. Compressor 8. Power supply 9. Process control equipment 10. Invertor (AC variable speed drive) 11. Thermocouple (T, pt-100) 12. Lid 13. Sliced 14. Shelf 15. Manometer

Figure 1. Schematic diagram of the experimental setup.

2. Experimental Setup

Heat pump dryer, which was analyzed in the experimenttal drying of tropical fruits, was shown in Figure 1. Dryer consists of the heat pump system, axial fan, thermocouple, process control equipment, invertor and drying chamber. Heat delivered in condenser is re-extracted from evaporators at the exit of the drying chamber. In this way, thermal balance of the heat pump system is achieved. PID controlled heat pump dryer adjusts the cycle of the axial fan according to the temperature value which is set in process control device. If the set value is higher than the temperature which is measured with the thermocouple, the flow of the air which is blown from the axial fan decreases. Thus, lower flow outer air is passed through the condenser so as to ensure that the temperature reaches the set value. If the set value is less than the temperature which is measured with the thermocouple, air velocity of the air blown from the axial fan will increase. Thus, fresh air with a bigger flow is passed through the condenser so that the temperature which is measured with the thermocouple reaches the set value.

When the temperature, which is measured by the thermocouple, reaches the set value; in other words, drying air temperature is equated with the set value, fan adjusts the air velocity by means of the invertor according to the measured temperature value. In heat pump dryer process, temperature control device is set to 40 ^{o}C and aims to keep the drying air temperature at the set value.

3. Experimental Procedure

Before the experiments launched in the heat pump dryer, the tropical fruits namely, kiwi, avocado and banana were peeled off and the following preparations were made.

1) Peeled off fruits were sliced at the thickness of 5 mm.

2) The fruits sliced at the thickness of 5 mm were dried in a drying oven at 70 $\pm 3\,^{o}$C.

3) During the drying period of 5 hours, weight measurement was made once an hour. At the end of two consecutive measurements, absolute dry weight was considered to be achieved on the condition that the weight changed less than 1%. 1% accurate digital weight measurement instrument (METTLER TOLEDO) was used for weight measurement.

Initial moisture content of the fruits was calculated from Equation (1).

$$MC_{db} = \frac{M_i - M_d}{M_d} \cdot 100 \tag{1}$$

Tropical fruits were placed in the heat pump dryer which was on the shelf in the drying chamber and drying process started. During the drying process, drying air temperature was determined to be 40 ^{o}C and it was set on process control device. PID control flow diagram for heat pump dryer is presented in Figure 2.

4. Energy Analysis

In first and second law analyses of thermodynamics, the drying process was considered as a steady flow process.

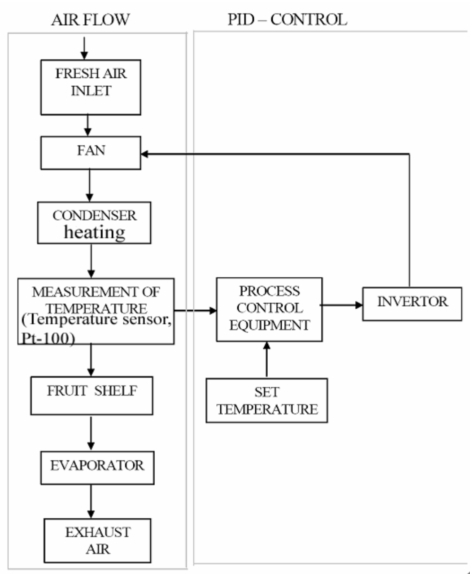

Figure 2. The systematic diagram of PID control system and air flow.

The main basis of these analyses is the phenomena of thermodynamics of humid air. Within the scope of the first law of thermodynamics, energy analysis of heat pump dryer of tropical fruits is performed to find out more about the energy aspects and behaviour of drying air throughout the heat pump dryer. Actually, the air conditioning processes can be modeled as steady flow processes which are analyzed by employing steady flow conservation of mass (for both dry air and moisture) and conservation of energy principles [9].

For energy and exergy analyses of the single-layer drying process, the following equations are generally employed to compute the mass conservation of drying air and moisture, energy conservation, and the exergy balance rate of the process [9,10]:

The overall performance of a HPD may be characterized by several criteria. Among them, the coefficient of performance (COP) and the specific moisture extraction rate (SMER) have been used by Jia *et al.* [11]. For an ideal refrigeration system operating between a condenser temperature of T_C and an evaporator temperature of T_E, the maximum heating coefficient of performance, $COP_{c,h}$ was obtained from the Carnot cycle as Table 1 and Equation 10 [12].

The SMER can be defined as the energy required to remove 1 kg of water and may be related to the power input to the compressor ($SMER_{hp}$) or to the total power to the dryer including the fan power and the efficiencies of the electrical devices ($SMER_{ws}$), as given by Jia *et al.* [11], Schmidt *et al.* [13], Hawlader *et al.* at Table 1 and Equation 12 [14].

5. The Second Law Analysis: Exergy Analysis

In the scope of the second law analysis of thermodynamics, total exergy inflow, outflow and losses of the heat pump dryer were estimated. The basic procedure for exergy analysis of the chamber is to determine the exergy values at steady-state points and the reason of exergy variation for the process [9,15]. The exergy values are calculated by using the characteristics of the working medium from a first law energy balance at Table 1 equation 13 [16].

There are variations of this general exergy equation. In the analyses of many systems, some, but not all, of the terms shown in Equation (13) are used. Since exergy is energy available from any source, the terms can be de-

Table 1. The equations of energy and heat pump dryer performance.

General equation of mass conservation of drying air	$\sum \dot{m}_i = \sum \dot{m}_o$	(2)
General equation of mass conservation of moisture	$\sum\left(\dot{m}_{wi} + \dot{m}_{mp}\right) = \sum \dot{m}_{wo}$	(3)
General equation of mass conservation of moisture	$\sum\left(\dot{m}_{ia} \cdot \omega_i + \dot{m}_{mp}\right) = \sum \dot{m}_{oa} \cdot \omega_o$	(4)
General equation of energy conservation	$\dot{Q}_{Cd} - \dot{W} = \sum \dot{m}_{ia} \cdot \left(h_{oa} - h_{ia} + \frac{V_o^2 - V_i^2}{2}\right)$	(5)
Heat used during moisture extraction in drying chamber	$\dot{Q}_{Dc} = \dot{m}_{ia}\left(h_{ia} - h_{oa}\right)$	(6)
The heat delivered in the condenser ($\dot{Q}_{Cd}$) was estimated using the experimental values [11].	$\dot{Q}_{Cd} = \dot{m}_{ia} \cdot C_{p,air} \cdot (T_{ia} - T_{aai})$	(7)
	$\dot{m}_{ia} = \rho_{ia} \cdot \dot{V}_i$	(8)
Energy utilization ratios of chamber	$EUR_{dc} = \frac{\dot{m}_{ia} \cdot \left(h_{ia} - h_{oa}\right)}{\dot{m}_{ia} \cdot C_{p,air} \cdot \left(T_{ia} - T_{aai}\right)}$	(9)
The coefficient of performance	$COP_{c,h} = \frac{T_C}{T_C - T_E}$	(10)
The system COP	$COP_{ws} = \frac{\dot{Q}_{Cd}}{\dot{w}_F + \dot{w}_C}$	(11)
Specific moisture extraction rate (SMER)	$SMER_{hpd} = \frac{\dot{m}_d}{\dot{w}_F + \dot{w}_C}$	(12)

veloped using electrical current flow, magnetic fields, and diffusional flow of materials. One common simplification is to substitute enthalpy for the internal energy and *P*V terms that are applicable for steady-flow systems. Equation (13) is often used under conditions where the gravitational and momentum terms are neglected. In addition to these, the pressure changes in the system are also neglected because of $V \cong V_\infty$.

In this case, Equation (13) is derived Equation (14).

The inflow and outflow of exergy can be found depending on the inlet and outlet temperatures of the shelf and the HPD chamber.

Applying Equations (17-21), the inflow, and outflow of exergy can be found depending on the inlet and outlet temperatures of the drying chamber. Hence, the exergy loss is determined by Table 2 and Equation (19).

The quantity of the exergy loss is calculated by applying Equations (14-21). The exergetic efficiency can be defined as the ratio of the product exergy to exergy inflow for the dryer chamber. However, it is explained as the ratio of exergy outflow to exergy inflow for the chamber. Thus, the general form of exergetic efficiency is written as Table 2 and Equation 21 [16,17].

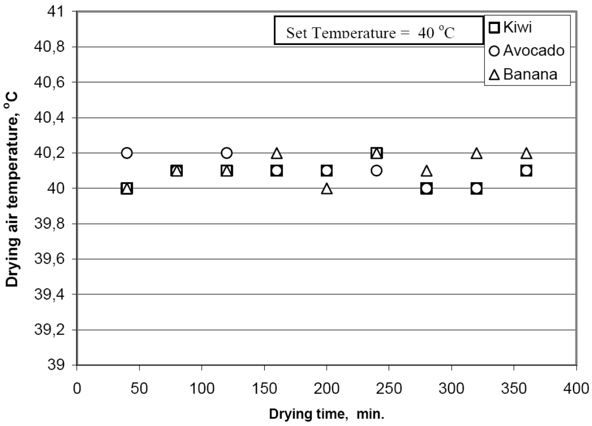

Figure 3. Variation of drying air temperature with drying time.

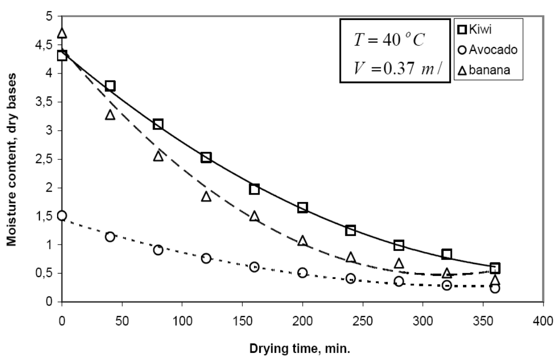

Figure 4. Variation in moisture content as a function of drying time.

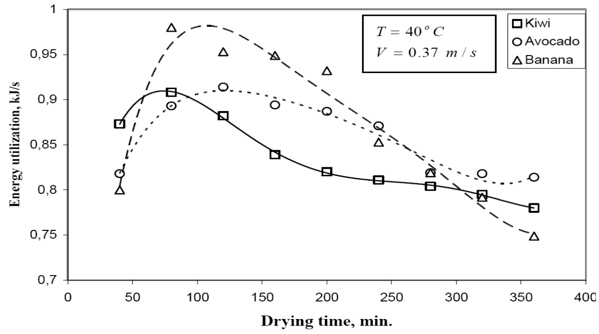

Figure 5. Variation in energy utilization as a function of drying time for the tropical fruits.

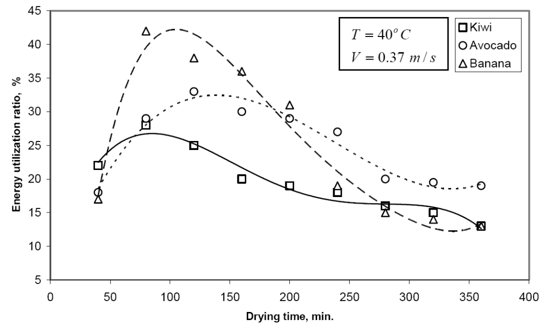

Figure 6. Variation in energy utilization ratio as a function of drying time at for the tropical fruits.

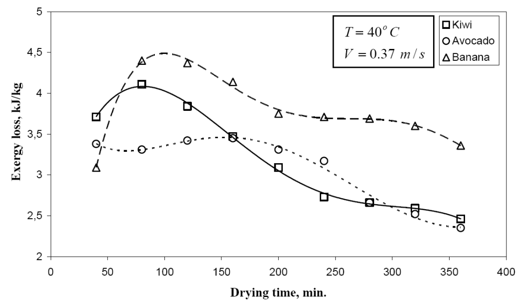

Figure 7. Variation in exergy loss with drying time for the drying chamber and the tropical fruit.

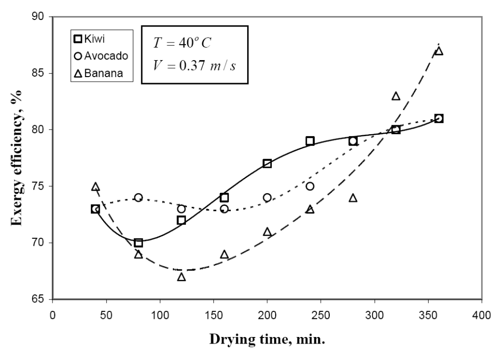

Figure 8. Variation in exergetic efficiency as a function of drying time in the drying chamber for the tropical fruit.

Table 2. The equations of exergy analysis.

The exergy values of the working medium	$Exergy = \underbrace{(u-u_\infty)}_{\text{internal energy}} - T_\infty \underbrace{(s-s_\infty)}_{\text{entropy}} + \underbrace{\frac{P_\infty}{j}(v-v_\infty)}_{\text{work}} + \underbrace{\frac{V^2}{2gJ}}_{\text{momentum}} + \underbrace{(z-z_\infty)\frac{g}{g_c j}}_{\text{gravity}} + \underbrace{\sum(\mu_c-\mu_\infty)N_c}_{\text{chemical}} + \underbrace{E_i A_i F_i (3T^4 - T_\infty^4 - 4T_\infty T^3)}_{\text{radiation emission}} + \cdots$	(13)
Exergy inlet to the drying chamber	$e_{ia} = \left[h_{ia}(T_{ia}) - h_{aai}(T_{aai}) - T_{aai}\left(S_{ia}(T_{ia}) - S_{aai}(T_{aai}) \right) \right]$	(14)
	In the equation;	
	$h_{ia}(T_{ia}) - h_{aai}(T_{aai}) = \bar{C}_p (T_{ia} - T_{aai})$	(15)
	$S_{ia}(T_{ia}) - S_{aai}(T_{aai}) = \bar{C}_p \ln\left(\frac{T_{ia}}{T_{aai}}\right)$	(16)
Re-organized in accordance with the Equations (15-16)	$e_{ia} = \bar{C}_p \left[(T_{ia} - T_{aai}) - T_{aai} \ln\left(\frac{T_{ia}}{T_{aai}}\right) \right]$	(17)
The average specific heat ($\bar{C}_p$)of drying air	$\bar{C}_p = C_{pa} + \omega_{ia} \cdot C_{pv}$	(18)
The exergy loss	$\sum E_{xL} = \sum E_{xi} - \sum E_{xo}$	(19)
The exergy outflow	$e_{oa} = \left[h_{oa}(T_{oa}) - h_v(T_{aai}) - T_{aai}\left(S_{oa}(T_{oa}) - S_v(T_{aai}) \right) \right]$	(20)
The general form of exergetic efficiency	$exergy\, efficiency = \frac{exergy\ outflow}{exergy\ \inf low}$ $\quad \eta_{ex} = \frac{e_{oa}}{e_{ia}}$	(21)

6. The Results of Experiment

Drying air temperature was attempted to be maintained at 40 °C in the heat pump dryer. The change of the drying air temperature according to the drying time during the drying process of the tropical fruits in heat pump dryer was given in Figure 3. As can be seen in Figure 3, drying air temperature changed between 40 °C and 40.2 °C. Drying air temperature in heat pump dryer was attempted to be kept the same with the accuracy of + 0.2 °C. Drying air velocity in heat pump dryer changed between 0.3 and 0.4 m/s. In the measurement of drying air velocity, air velocity measurement instrument (TESTO) with heated wire, NTC sensor, and 0.01 m/s accuracy was used. The mean value of dynamic drying air velocity between 0.3 m/s and 0.4 m/s during the drying period was 0.37 m/s. Drying air velocity is obtained as 0.37 m/s for energy and exergy analyses.

Before the drying process in heat pump dryer, initial-moisture content calculated from Equation (1) in the drying oven was 4.31 g water / g dry matter for kiwi, 1.51 g water / g dry matter for avocado and 4.71 g water/ g dry matter for banana. Initial moisture content of tropical fruits was determined. Then tropical fruits were dried separately in heat pump dryer. The change of their moisture contents according to the drying period during the drying in heat pump dryer was calculated from Equation (1) and given in Figure 4. Drying ratio of kiwi and banana whose initial moisture content was high was faster when compared to avocado whose initial moisture content was lower.

Energy utilization in heat pump dryer was calculated from Equation (5) and the change according to the drying time was given in Figure 5. As can be seen in Figure 5, the energy utilization increased at the onset of the drying process. As the drying process went on, utilized energy decreased. The increase in utilized energy at the onset of the drying process was a result of the energy made use of in heating drying chamber. Energy utilization in heat pump dryer together with heating the drying chamber was for evaporating the moisture in tropical fruits.

Energy utilization in drying chamber decreased as the moisture content in fruits decreased. Energy utilization-ratio of heat pump dryer in drying chamber was cal-

Table 3. Evaluation of heat pump dryer performance.

Fruit	COP_{ws}	$SMER_{ws}$ (g/kWh)	Drying time (min)	Initial and final moisture content (g water/ g dry matter)	Mean air velocity (m/s)	Drying air temperature (^oC)
Kiwi	2.49	81.5	360	4.31 - 0.59	0.37	40
Avocado	2.41	58.8	360	1.51 - 0.24	0.37	40
Banana	2.47	87.9	360	4.71 - 0.39	0.37	40

culated from Equation (9) and given in Figure 6. Energy utilization ratio of banana was high, whose moisture content was also high. Energy utilization ratio in drying chamber decreased as the moisture content in fruits decreased, similar to the utilized energy.

COP_{ws} was calculated from Equation (11) for whole system of heat pump dryer and SMER was calculated from Equation (12) and given in Table 3.

The outlet temperature of the drying air from the drying chamber was low due to the energy utilization for heating the drying chamber and the fruits at the onset of the drying process. Therefore, both energy utilization and exergy loss increased at the onset of the drying process.

Exergy loss in the drying chamber was calculated from Equation (19) and given in Figure 7. At the onset of the drying process, exergy efficiency decreased due to the exergy loss. Therefore, the exergy efficiency, which was low at the onset of the drying process, increased as the drying process continued. Energy utilization in drying chamber decreased as the moisture content of the fruits decreased and exergy efficiency increased. The change of the exergy efficiency according to the drying period was calculated from Equation (21) and given in Figure 8.

7. Conclusions

PID controlled heat pump dryer was analysed experimentally in the drying of the tropical fruits such as kiwi, avocado and banana. The study carried out on the obtained experimental results is as follows:

1) An energy source other than heat pump dryer system condenser can be used in dryer.

2) As a little amount of fruits were dried in heat pump dryer, SMER was low. SMER will increase as the amount of dried fruits or the moisture contents of the fruits to be dried are increased.

3) Some by-pass air can be used in heat pump dryer instead of fully using fresh air. This may also decrease the drying air velocity

4) The temperature value set in process control equipment was 40 ^oC. The air velocity may be increased by decreasing of set temperature.

5) It was experimentally shown that PID controlled heat pump dryer, which was studied herein, can be used for drying the materials which were adversely affected from the temperature changes during the drying process.

8.References

[1] İ. Ceylan and H. Doğan, “Nem kontrollü kondenzasyonlu kereste kurutma fırını,” II. Ulusal Ege Enerji Sempozyumu ve Sergisi., Dumlupınar Üniversitesi, Kütahya., Turkish, pp. 155–166, 2004.

[2] M. Fatouh, A. B. Metwally, A. B. Helali, and M. H. Shedid, “Herbs drying using a heat pump dryer,” Energy Conversion and Management, Vol. 47, No. 15–16, pp. 2629–2643, 2006.

[3] H. Ogura, N. Hamaguchi, H. Kage, and A. S. Mujumdar, “Energy and cost estimation for application of chemical heat pump dryer to industrial ceramics drying,” Drying Technology, Vol. 22, No. 1–2, pp. 307–323, 2004.

[4] R. Queiroz, A. L. Gabas, and V. R. N. Telis, “Drying kinetics of tomato by using electric resistance and heat pump dryers,” Drying Technology, Vol. 22, No. 7, pp. 1603–1620, 2004.

[5] K. J. Chua and S. K. Chou, “A modular approach to study the performance of a two- stage heat pump system for drying,” Applied Thermal Engineering, Vol. 25, No. 8–9, pp. 1363–1379, 2005.

[6] S. Achariyaviriya, S. Sopanronnarit, and A. Terdyothin, “Mathematical model development and simulation of heat pump fruit dryer,” Drying Technology, Vol. 18, No. 1–2, pp. 479–491, 2000.

[7] K. J. Chua, S. K. Chou, J. C. Ho, and M. N. A. Hawlader, “Heat pump drying: Recent developments and future trends,” Drying Technology, Vol. 20, No. 8, pp 1579–1610, 2002.

[8] M. N. A. Hawlader, C. O. Perera, M. Tian, and K. L. Yeo, “Drying of guava and papaya: Impact of different drying methods,” Drying Technology, Vol. 24, No. 1, pp. 77–87, 2006.

[9] A. Midilli and H. Kucuk, “Energy and exergy analyses of solar drying process of pistachio,” Energy, Vol. 28, pp. 539–556, 2003.

[10] Y. A. Cengel and M. A. Boles, “Thermodynamics: An engineering approach,” McGraw-Hill, New York, 1994.

[11] X. Jia, P. Jolly, and S. Clemets, “Heat pump assisted continues drying,” Part 2: Simulation Results, International Journal of Energy Research, Vol. 14, pp. 771–782, 1990.

[12] Y. A. Cengel and M. A. Boles, “Thermodynamics: An engineering approach,” Third Edition, McGraw-Hill,

New York, pp. 1056, 1998.

[13] E. L. Schmidt, K. Klocker, N. Flacke, and F. Steimle, “Applying the transcritical CO_2 process to a drying heat pump,” International Journal of Refrigeration, Vol. 21, No. 3, pp. 202–211, 1998.

[14] M. N. A. Hawlader, S. K. Chou, J. C. Ho, and K. J. Chua, “On the development of a heat pump dryer to maximise heat recevery,” in A. S. Mujumdar (Series Ed.), Proceedings of the 11th International Drying Symposium, Halkidiki, Greece, No. 19–22, pp. 616–623, August 1998.

[15] A. Bejan, “Advanced engineering thermodynamics,” Wiley, New York, 1988.

[16] O. Zuhal, “Testing of a heat-pump-assisted mechanical opener dryer,” Applied Thermal Engineering, Vol. 23, pp. 153–162, 2003.

[17] I. Ceylan, M. Aktaş, and H. Doğan, “Energy and exergy analysis of timber dryer assisted heat pump,” Applied Thermal Engineering, Vol. 27, pp. 216–222, 2007.

Nomenclature

M_i initial weight
M_d exact dry weight
C_p specific heat, kJ kg $^{-1}$ K $^{-1}$
$\overline{C}_p$ mean specific heat, kJ kg $^{-1}$ K $^{-1}$
$\dot{m}$ mass flow rate, kg s $^{-1}$
$\dot{Q}_{Cd}$ heat delivered in condenser, kJ s $^{-1}$
T temperature, K
$\dot{W}$ energy utilization, kJ s $^{-1}$
ω specific humidity, g g $^{-1}$
V velocity, m s $^{-1}$
ρ density of air , kg m $^{-3}$
$\dot{w}_C$ power input to compressor (kW)
$\dot{w}_F$ power input to fan (kW)
H enthalpy, kJ kg $^{-1}$
$COP_{c,h}$ heating coefficient of performance of Carnot cycle
COP_{ws} heating coefficient of performance of heat pump
$SMER_{hpd}$ specific moisture extraction rate for whole system, kg kJ^{-1} s h^{-1}
$\dot{m}_d$ drying rate, kg h^{-1}
e exergy, kJ kg^{-1}
S specific entropy, kJ kg $^{-1}$ K^{-1}
$\dot{V}_i$ volumetric flow rate of air, m^3 s^{-1}
EUR energy utilization ratio, %
PID proportional integral derivative

Subscripts

wi water inlet
we water evaporation
wo water outlet
i inlet
oa outlet air
∞ surrounding or ambient
ci condenser inlet
ws whole system
HPD heat pump dryer
v vapour
ia inlet air
aai ambient air inlet

Engineering, 2009, 1, 196-200
doi:10.4236/eng.2009.13023 Published Online November 2009 (http://www.scirp.org/journal/eng).

Analysis for Transverse Sensitivity of the Microaccelerometer

Yu LIU[1,2,3], Guochao WANG[1,2,3], Changwen GUO[1,2,3]
[1]*Automobile College, Chongqing University of Technology, Chongqing, China*
[2]*Key Laboratory of Automobile Parts & Test Technique in Chongqing, Chongqing, China*
[3]*Chongqing Engineering Research Center for Automobile Power System and Control, Chongqing, China*
E-mail: *liuyu_cq@126.com*
Received January 10, 2009; *revised February* 21, 2009; *accepted February* 23, 2009

Abstract

For the microaccelerometer, strong axial response and weak cross-axial one are always expected. This paper presents a general analysis about transverse sensitivity of the microaccelerometer. The analysis model is developed, where the influence of response stiffness and damping in different axes, as well as symmetrical decline angles of 3 degrees of freedom system is considered. Moreover, multi-freedom vibration equations based on the analysis model are established. And the equations are solved on condition that damping force is ignored. Finally, the theoretical analysis about transverse sensitivity is accomplished, and some effective methods, which are beneficial to reduce cross disturbance, are provided.

Keywords: MEMS, Accelerometers, Transverse Sensitivity, Multi-Freedom Vibration Equation

1. Introduction

For the microaccelerometer, there should be no output if the input acceleration is along the cross axis. In fact, however, the output created by forces induced in orthogonal axis is not equal to zero. This phenomena is called cross coupling, which is measured by transverse sensitivity [1–3].

In this paper, the analysis model for cross disturbance of the microaccelerometer is developed, where the influence of response stiffness and damping in different axes, as well as symmetrical decline angles of 3 degrees of freedom system is considered. Moreover, multi- freedom vibration equations based on the analysis model are established. And the equations are solved on condition that damping force is ignored. Finally, the theoretical analysis about transverse sensitivity is accomplished, and some effective methods, which are beneficial to reduce cross disturbance, are provided.

2. Transverse Sensitivity

Transverse sensitivity is the ratio of the output caused by acceleration perpendicular to the main sensitivity axis divided by the basic sensitivity in the main direction. It is an important characteristic of the microaccelerometer, and is primarily caused by two factors [4–6]. One is from the inherent microstructure, which may be eliminated by adopting the appropriate working principle and optimizing the design parameters. The other is from inaccuracies in fabrication process, package orientation and misalignment, which is only to be reduced as possible as we can.

For example, *x*-axis accelerometer, due to inevitability of errors in fabrication and misalignments, the applied acceleration can be expressed as acceleration along the *x*-axis and accelerations perpendicular to the main sensitivity axis, denoted as $\vec{a}_x, \vec{a}_y, \vec{a}_z$ respectively. Therefore, the output is given by

$$V_{xout} = S_x a_x + S_{yx} a_y + S_{zx} a_z \text{ ....}(1)$$

where S_{yx} or S_{zx} is transverse sensitivity of *x*-axis in *y* or *z* direction. Unfortunately, the accelerometer cannot distinguish the change in voltage caused by accelerations $\vec{a}_y$ and $\vec{a}_z$, which results in a difference of $S_{yx}a_y + S_{zx}a_z$.

Disturbance and coupling from different axes have important influences on the performance of the microaccelerometer. So strong axial response and weak cross-axial one are always expected. And the transverse sensitivity is always expected to small enough, even close to zero.

3. Analysis of Transverse Sensitivity

3.1. Model

In most cases, the microstructure of the accelerometer can be represented as a mass-spring-damper system. Figure 1 shows the mechanical model of the microaccelerometer with a single *x*- degree of freedom. In perfect condition, elastic deformation of the spring induced by the inertial force is always along the *x*-axis no matter where acceleration signal is from. In fact, however, the phenomenon of cross coupling exists inevitably. On the one hand, the elastic deformation of the equivalent spring occurs not only in primary *x*-axis but also in orthogonal *y*-axis and *z*-axis, and on the other hand, the displacement of the microstructure under acceleration $\vec{a}_x$ is not always along the primary *x*-axis, which may be at an angle with the ideal sensitive axis [7].

Figure 2 illustrates the mechanical model of microaccelerometer with three degrees of freedom, where elastic deformation is along *x*-axis, *y*-axis and *z*-axis. So the acceleration ponderance $\vec{a}_x, \vec{a}_y, \vec{a}_z$ are detected by the corresponding degree of freedom system. Because the microstructure has the same proof mass, the different equivalent stiffness and damping coefficients, denoted as K_x, K_y, K_z and B_x, B_y, B_z respectively, the model in Figure 2 is the analysis model of cross disturbance resulted from stiffness and damping in different axes.

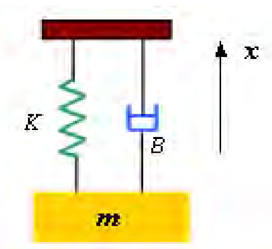

Figure 1. Simplified mechanical model of the microaccelerometer with a single *x*- degree of freedom.

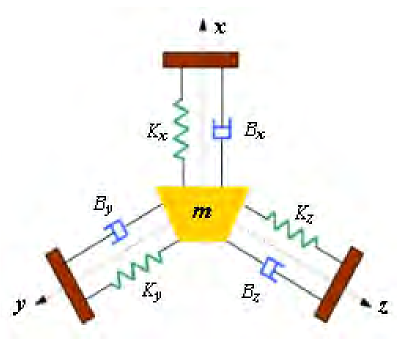

Figure 2. Analysis model of cross disturbance resulted from stiffness and damping in different axes.

Figure 3 shows the other model of the microaccelerometer, where the spring and the damper are not along the primary axis but that at an angle with the corresponding ideal axis. For example, *x*- degree of freedom system, as illustrated in Figure 3(a), due to inevitability of errors in fabrication process, package orientation as well as misalignment, the spring K_x and damper B_x are all at an angle with *x*-axis, which is called symmetrical decline angle anddenoted as α_x. At the same time, the spring K_x and damper B_x are also at an angle with *y*-axis or *z*-axis, denoted as β_x, γ_x respectively. Most often, α_x is quite small, and β_x, γ_x are all close to $\pi/2$. Therefore,

$$\cos^2\alpha_x + \cos^2\beta_x + \cos^2\gamma_x = 1 \tag{2}$$

Similarly, β_y, γ_z are the symmetrical decline angles of *y*- and *z*- degree of freedom systems respectively, as shown in Figure 3 (b) and (c).

So the model in Figure 3 is the analysis model of cross disturbance resulted from the symmetrical decline angles.

3.2. Solution

In order to analyze the influence of cross disturbance, the multi-freedom vibration equations based on the above-mentioned models should be established.

Here sinusoidal signal is considered. $a_x \sin\omega t$, $a_y \sin\omega t$, $a_z \sin\omega t$ denote three projections of vector acceleration respectively. Furthermore, assume the displacement function is as follows:

$$\begin{cases} w_x = W_x^{(x)}\sin\omega t \\ w_y = W_y^{(x)}\sin\omega t \\ w_z = W_z^{(x)}\sin\omega t \end{cases} \tag{3}$$

where $W_x^{(x)}, W_y^{(x)}, W_z^{(x)}$ are the amplitudes along the *x*, *y* and *z*-direction respectively.

For *x*-degree of freedom system, the vibration equation responded to acceleration signal $a_x \sin\omega t$ is given by:

$$m\begin{Bmatrix}\ddot{w}_x\\ \ddot{w}_y\\ \ddot{w}_z\end{Bmatrix} + \begin{bmatrix} B_{xx} & B_{xy} & B_{xz}\\ B_{xy} & B_{yy} & B_{yz}\\ B_{xz} & B_{yz} & B_{zz}\end{bmatrix}\begin{Bmatrix}\dot{w}_x\\ \dot{w}_y\\ \dot{w}_z\end{Bmatrix} + \begin{bmatrix} K_{xx} & K_{xy} & K_{xz}\\ K_{xy} & K_{yy} & K_{yz}\\ K_{xz} & K_{yz} & K_{zz}\end{bmatrix}\begin{Bmatrix} w_x\\ w_y\\ w_z\end{Bmatrix} = \begin{Bmatrix} ma_x\sin\omega t\\ 0\\ 0\end{Bmatrix} \tag{4}$$

where w_x, w_y, w_z are the displacements of proof mass along the *x*, *y* and *z*-direction respectively. $\dot{w}_x$, $\dot{w}_y$, $\dot{w}_z$ and $\ddot{w}_x$, $\ddot{w}_y$, $\ddot{w}_z$ denote the first and the second derivative of displacement w_x, w_y, w_z with respect to time *t* respectively. K_{xx}, K_{yy}, K_{zz} are the self-stiffness of equiva-

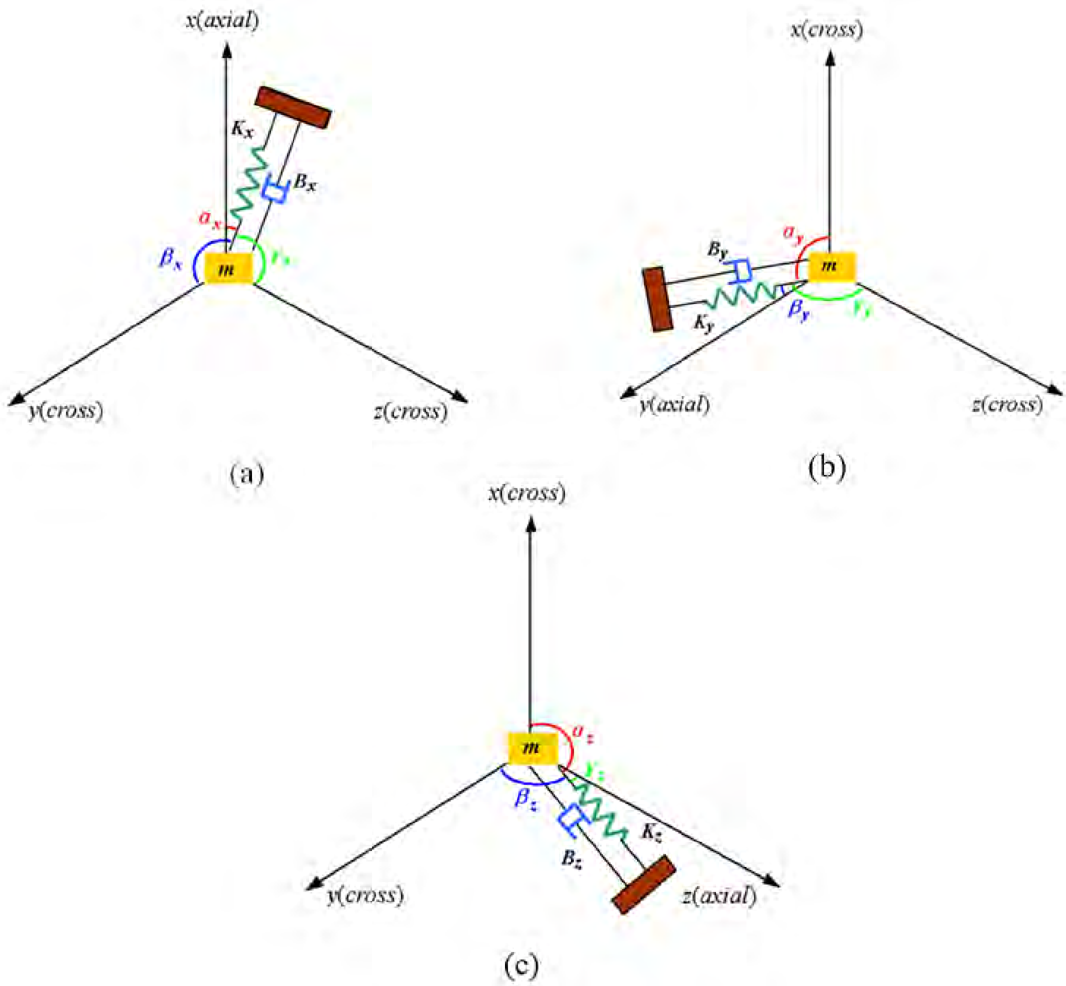

Figure 3. Analysis model of cross disturbance resulted from the symmetrical decline angles. (a) *x*-degree of freedom system. (b) *y*-degree of freedom system. (c) *z*-degree of freedom system.

lent spring K_x, which reflect responsibility of spring K_x in three orthogonal axes. K_{xy}, K_{yz}, K_{xz} are the coupling stiffness of equivalent spring K_x, which reflect responsibility of spring K_x in three coupling orthogonal axes. And B_{xx}, B_{yy}, B_{zz} are the self-damping of equivalent coefficient B_x, which reflect the damping effect of B_x in three orthogonal axes. B_{xy}, B_{yz}, B_{xz} are the coupling damping of equivalent coefficient B_x, which reflect the damping effect of B_x in three coupling orthogonal axes.

Substituting Equation (3) into Equation (4), we get the system of three linear equations in three variables $W_x^{(x)}$, $W_y^{(x)}, W_z^{(x)}$:

$$\begin{cases}(K_{xx}\sin\omega t + B_{xx}\omega\cos\omega t - m\omega^2\sin\omega t)W_x^{(x)} + (K_{xy}\sin\omega t + B_{xy}\omega\cos\omega t)W_y^{(x)} + (K_{xz}\sin\omega t + B_{xz}\omega\cos\omega t)W_z^{(x)} = ma_x\sin\omega t \\ (K_{xy}\sin\omega t + B_{xy}\omega\cos\omega t)W_x^{(x)} + (K_{yy}\sin\omega t + B_{yy}\omega\cos\omega t - m\omega^2\sin\omega t)W_y^{(x)} + (K_{yz}\sin\omega t + B_{yz}\omega\cos\omega t)W_z^{(x)} = 0 \\ (K_{xz}\sin\omega t + B_{xz}\omega\cos\omega t)W_x^{(x)} + (K_{yz}\sin\omega t + B_{yz}\omega\cos\omega t)W_y^{(x)} + (K_{zz}\sin\omega t + B_{zz}\omega\cos\omega t - m\omega^2\sin\omega t)W_z^{(x)} = 0\end{cases} \tag{5}$$

Usually, there are three ponderances of vector acceleration, denoted as $\bar{a}_x, \bar{a}_y, \bar{a}_z$. They are responded by the respective degree of freedom system. Furthermore, response along the *x*, *y* and *z*-direction exist in each degree of freedom system. So there are nine amplitude expressions responded to the acceleration signal. In order to simplify the analysis, damping force is ignored. Therefore, Equation (5) is simplified to:

$$\begin{cases} (K_{xx}-m\omega^2)W_x^{(x)}+K_{xy}W_y^{(x)}+K_{xz}W_z^{(x)}=ma_x \\ K_{xy}W_x^{(x)}+(K_{yy}-m\omega^2)W_y^{(x)}+K_{yz}W_z^{(x)}=0 \\ K_{xz}W_x^{(x)}+K_{yz}W_y^{(x)}+(K_{zz}-m\omega^2)W_z^{(x)}=0 \end{cases} \tag{6}$$

Hence,

$$\begin{cases} W_x^{(x)}=-\dfrac{K_x\sin^2\alpha_x-m\omega^2}{(K_x-m\omega^2)\omega^2}a_x \\ W_y^{(x)}=\dfrac{K_x\cos\alpha_x\cos\beta_x}{(K_x-m\omega^2)\omega^2}a_x \\ W_z^{(x)}=\dfrac{K_x\cos\alpha_x\cos\gamma_x}{(K_x-m\omega^2)\omega^2}a_x \end{cases} \tag{7}$$

Likewise, the amplitudes responded to acceleration signal $a_y\sin\omega t, a_z\sin\omega t$ are respectively given by

$$\begin{cases} W_x^{(y)}=\dfrac{K_y\cos\alpha_y\cos\beta_y}{(K_y-m\omega^2)\omega^2}a_y \\ W_y^{(y)}=-\dfrac{K_y\sin^2\beta_y-m\omega^2}{(K_y-m\omega^2)\omega^2}a_y \\ W_z^{(y)}=\dfrac{K_y\cos\beta_y\cos\gamma_y}{(K_y-m\omega^2)\omega^2}a_y \end{cases} \tag{8}$$

And

$$\begin{cases} W_x^{(z)}=\dfrac{K_z\cos\alpha_z\cos\gamma_z}{(K_z-m\omega^2)\omega^2}a_z \\ W_y^{(z)}=\dfrac{K_z\cos\beta_z\cos\gamma_z}{(K_z-m\omega^2)\omega^2}a_z \\ W_z^{(z)}=-\dfrac{K_z\sin^2\gamma_z-m\omega^2}{(K_z-m\omega^2)\omega^2}a_z \end{cases} \tag{9}$$

3.3. Analysis

Building on the previous analysis, we get the nine amplitude expressions responded to the sinusoidal acceleration signal, as listed in Table 1.

For 3-axis microaccelerometer, what we need is the amplitude response in leading diagonal of Table 1. They should be the strongest, whereas the others are the cross disturbance. Therefore, transverse sensitivity of *x*-axis in *y*- and *z*-direction are given by

$$\begin{aligned} S_{yx}&=\frac{S_{y-cross}}{S_{x-axial}}=\frac{K_y\cos\alpha_y\cos\beta_y}{m\omega^2-K_x\sin^2\alpha_x}\cdot\frac{K_x-m\omega^2}{K_y-m\omega^2}, \\ S_{zx}&=\frac{S_{z-cross}}{S_{x-axial}}=\frac{K_z\cos\alpha_z\cos\gamma_z}{m\omega^2-K_x\sin^2\alpha_x}\cdot\frac{K_x-m\omega^2}{K_z-m\omega^2}. \end{aligned} \tag{10}$$

Similarly,

$$\begin{aligned} S_{xy}&=\frac{S_{x-cross}}{S_{y-axial}}=\frac{K_x\cos\alpha_x\cos\beta_x}{m\omega^2-K_y\sin^2\beta_y}\cdot\frac{K_y-m\omega^2}{K_x-m\omega^2}, \\ S_{zy}&=\frac{S_{z-cross}}{S_{y-axial}}=\frac{K_z\cos\beta_z\cos\gamma_z}{m\omega^2-K_y\sin^2\beta_y}\cdot\frac{K_y-m\omega^2}{K_z-m\omega^2}. \end{aligned} \tag{11}$$

$$\begin{aligned} S_{xz}&=\frac{S_{x-cross}}{S_{z-axial}}=\frac{K_x\cos\alpha_x\cos\gamma_x}{m\omega^2-K_z\sin^2\gamma_z}\cdot\frac{K_z-m\omega^2}{K_x-m\omega^2}, \\ S_{yz}&=\frac{S_{y-cross}}{S_{z-axial}}=\frac{K_y\cos\beta_y\cos\gamma_y}{m\omega^2-K_z\sin^2\gamma_z}\cdot\frac{K_z-m\omega^2}{K_y-m\omega^2}. \end{aligned} \tag{12}$$

If the microaccelerometer sensitive to the change in displacement has three primary axes, then the equation $K_x=K_y=K_z$ is always expected for uniform sensitivity in three sense directions. So the expressions of transverse sensitivity in Equation (10)–(12) could be simplified. Considering constraints for symmetrical decline angles of *x*-, *y*- and *z*- degrees of freedom system, that is, $\alpha_x, \beta_y, \gamma_z$ are all close to zero, it's not difficult to find that transverse sensitivity only relates to the coupling angles and the way for small transverse sensitivity is to make the coupling angles equal to $\pi/2$. Of course, α_y, α_z are the coupling angles of *x*- system, while β_x, β_z and γ_x, γ_y are those of *y*- and *z*- systems respectively. If the coupling angles are all equal to $\pi/2$, then transverse sensitivity S=0.

It should be pointed out if the microaccelerometer has only one or two primary axes, then the above six expressions about transverse sensitivity will be decreased by four or two. For instance, there are only S_{yx}, S_{zx} for *x*-axis accelerometer. So transverse sensitivity relates not only to the coupling angles but also to the response stiffness in different axes. Therefore, two methods are recommended to reduce transverse sensitivity. One is to make the coupling angles equal to $\pi/2$. The other is to ensure the response stiffness in the primary axis far less than that in the cross axis.

4. Summary

This paper presents a general analysis about transverse sensitivity of the microaccelerometer. Firstly, the analysis model for cross disturbance of the microaccelerometer is developed, where the influence of response stiffness and damping in different axes, as well as symmetrical decline angles of 3 degrees of freedom system are considered. Secondly, multi-freedom vibration equations based on the analysis model are established. And the equations are solved on condition that damping force is ignored. Finally, some effective methods, which are beneficial to reduce cross disturbance, are provided. For the microaccelerome-sensitive to the change in displacement, if it has

Table 1. Amplitude responded to the sinusoidal acceleration signal.

Amplitude / Acceleration	*x*-direction	*y*-direction	*z*-direction
$a_x \sin \omega t$	$-\frac{K_x \sin^2 \alpha_x - m\omega^2}{(K_x - m\omega^2)\omega^2} a_x$	$\frac{K_x \cos \alpha_x \cos \beta_x}{(K_x - m\omega^2)\omega^2} a_x$	$\frac{K_x \cos \alpha_x \cos \gamma_x}{(K_x - m\omega^2)\omega^2} a_x$
$a_y \sin \omega t$	$\frac{K_y \cos \alpha_y \cos \beta_y}{(K_y - m\omega^2)\omega^2} a_y$	$-\frac{K_y \sin^2 \beta_y - m\omega^2}{(K_y - m\omega^2)\omega^2} a_y$	$\frac{K_y \cos \beta_y \cos \gamma_y}{(K_y - m\omega^2)\omega^2} a_y$
$a_z \sin \omega t$	$\frac{K_z \cos \alpha_z \cos \gamma_z}{(K_z - m\omega^2)\omega^2} a_z$	$\frac{K_z \cos \beta_z \cos \gamma_z}{(K_z - m\omega^2)\omega^2} a_z$	$-\frac{K_z \sin^2 \gamma_z - m\omega^2}{(K_z - m\omega^2)\omega^2} a_z$

three primary axes, then transverse sensitivity only relates to the coupling angle and the way for small transverse sensitivity is to make the coupling angles equal to $\pi/2$. If it has one or two primary axes, then transverse sensitivity relates not only to the coupling angle but also to the response stiffness in different axes. So in order to reduce transverse sensitivity, two methods are recommended. One is to make the coupling angles equal to $\pi/2$. The other is to ensure the response stiffness in the primary axis far less than that in the cross axis.

5. References

[1] L. Fei, X. X. Zhong, Z. Y. Wen, *et al*, "Methods for reducing sensitivity of micromachined silicon accelerometer," Optics and Precision Engineering, No. 3, pp. 64–68, 1995

[2] J. S. Wang, Q. Wang, and S. H. Sun, "Effect of cross-coupling coefficient of accelerometer on gyros–free inertial measurement unit," Journal of Chinese Inertial Technology, No. 11, pp. 29–33, 2003.

[3] L. Zhong., J. G. Liu, and H. Y. Zhao, "A solution to the problem of excessive error of piezoelectrical accelerometer's cross axis sensitivity," Electro-Mechanical Engineering, Vol. 20, pp. 4–5, 2004.

[4] Y Liu, Z. Y. Wen, Z. Q. Wen, *et al*, "Design and fabrication of a high-sensitive capacitive biaxial microaccelerometer," J. Micromech. Microeng, Vol. 17, pp. 36–41, 2007.

[5] Y Liu, Z. Y. Wen, and H. Y. Yang, "Effect of fabrication characteristic of 2–d microaccelerometer on performance," Journal of Functional Materials and Devices, Vol. 14, pp. 331–335, 2008.

[6] Y. Liu, Z. Y. Wen, L. Q. Zhang, *et al*, "Structure design and system simulation of 2–d microaccelerometer," ISTM05, Vol. 3, pp. 2071–2075.

[7] N. Zeng, "Research on the key technology of fiber optic accelerometers," Doctor Thesis, Tsinghua University, pp. 97–100, 2005.

Engineering, 2009, 1, 201-210
doi:10.4236/eng.2009.13024 Published Online November 2009 (http://www.scirp.org/journal/eng).

Quasi-Square Wave Mode Phase-Shifted PWM LCC Resonant Converter for Regulated Power Supply

S. PADMANABHAN, Y. SUKHI, Y. JEYASHREE
R M K Engineering College, Anna University, Chennai, India
E-mail:*sukhirmk*03@gmail.com
Received January 10, 2009; *revised February* 21, 2009; *accepted February* 23, 2009

Abstract

This paper presents an improved self sustained oscillating controller circuit using LCC components for improving the overall efficiency of the system. It has a micro controller based active controller, which controls the performance from no-load up to full-load. The steady state characteristics are developed and a design example is given in detail. The proposed controller allows zero current switching at any loading condition which results in a reasonable reduction of power loss during switching with a promising efficiency. Analytical and experimental results verify the achievement the design specifications.

Keywords: Zero Voltage Switching, Zero Current Switching, DC-DC Converter, Resonant Converter, Soft Switching

1. Introduction

With ever increasing concerns about electromagnetic compatibility (EMC) issues, more attention is being paid to resonant converters as they provide better sinusoidal waveforms. Furthermore, resonant converters can make use of natural oscillation to achieve zero voltage switching (ZVS) and/or zero current switching (ZCS) thus eliminating switching losses [1]. As such both higher power-packing densities and conversion efficiencies can be achieved at high switching frequencies without snubbers. The full-bridge converter is widely used in power dc–dc conversions because it can achieve soft-switching with the help of LCC components added in the circuit [2]. The soft-switching techniques for PWM full bridge converter can be classified into two kinds: one is zero-voltage-switching (ZVS) and the other is zero-current-switching (ZCS). For dc-dc power conversion applications, the conventional phase-shift full-bridge dc/dc converter has drawn more attention in recent decades due to its advantages: high conversion efficiency, high power density, and low electro magnetic interference [3–8]. In order to obtain high conversion efficiency for dc-dc power conversion applications, a soft-switched dc/dc converter with a LCC primary-side energy storage elements based on [9–12] is studied and implemented in this paper.

Section II presents the principle of operation of the LCC resonant converter. Successively, the Section III deal with the mathematical analysis of converter. The performance characteristics of the converter are obtained from the mathematical analysis in section IV. An optimum design procedure of this converter is proposed in section V paper only after having a study on the performance characteristics of the LCC resonant converter and it can be considered as a design reference for other engineers. Finally, a 100-kHz, 48W (40V/1.2A) laboratory-made prototype is built up to verify all the theoretical analysis and evaluation. The highest full-load conversion efficiency of this converter reaches about 95.56%. Compared with the traditional dc/dc converter, its advantage in high conversion efficiency shows good potential for various dc-dc power converter applications. Finally, some conclusions of the work are provided in Section IX.

2. Principle of Operation

Like switch mode dc-to-dc converter, resonant converters are used to convert dc-to-dc through an additional conversion stage: the resonant stage in which dc signal is converted to high frequency ac signal. The potential

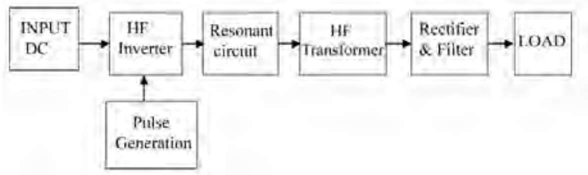

Figure 1. Block diagram.

advantage of resonant converter include the natural commutation of power switches, resulting in low switching power dissipation and reduced component stresses, which in terns results in increased power efficiency and increased switching frequency; higher operating frequencies results in reduced size and weight of equipment and results in faster responses; possible reduction in EMI problems. Since the size and weight of the magnetic components (inductors and transformers) and capacitors in a converter are inversely proportional to the converter switching frequency, many power converters have been designed at progressively higher frequencies in order to reduce excessive size and weight and obtain fast converter transients. In recent years, the market demand for wide applications that need variable speed drives, highly regulated power supplies, uninterruptible power supplies, and the desire to have smaller size and lighter weight power electronics systems has been increased. There are many soft witching techniques available in the literature to improve the switching behavior of dc-to-dc resonant converters. At the time of writing these words, intensive research in soft switching is under way to further improve efficiency with increased switching frequency of power electronic circuits**.**

A dc-to-dc resonant converter can be described by the major circuit blocks as shown in Figure 1. The dc-to-ac input inversion circuit, the resonant energy buffer tank circuit, and the ac-to-dc output rectifying circuit. Typically, the dc to ac inversion is achieved by using a various types of switching network topologies. The resonant tank which serves as an energy buffer between the input and output is normally synthesized by using lossless frequency selective network. The purpose of that network is to regulate the energy flow from the source to the load. Finally, the ac-to-dc conversion is achieved by incorporating rectifier circuits at the output section of the converter.

3. Mathematical Analysis of Converter

Figure 2 shows the A.C. equivalent circuit of LCC

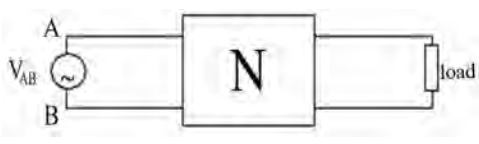

Figure 2. A.C equivalent circuit of LCC resonant converter.

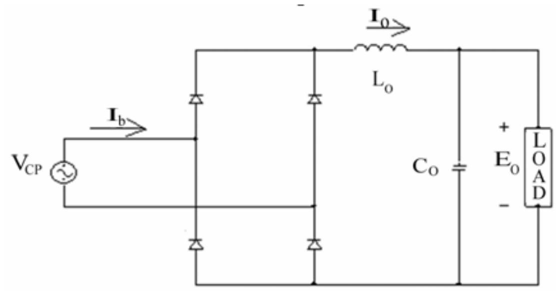

Figure 3. Output circuit of bridge rectifier and filter component to resonant converter.

resonant converter. The following assumptions are used in the mathematical analysis of the series parallel resonant converter.

1) The switches, diodes, inductors, capacitors and snubber components used are ideal.

2) The effects of snubber are neglected.

3) The filter inductance is large enough to keep the load current constant.

4) The high frequency transformer is ideal and has unity turns ratio.

Where N - is the resonant network, R_{ac} - AC equivalent load resistance, V_{AB} - RMS fundamental component of $V_{AB.}$

From the output circuit of bridge rectifier and filter component to resonant converter fig.3, V_{cp} and I_b represent the rms fundamental component of V_{cp} (t) and I_b (t) respectively. The output circuit consists of the diode bridge rectifier and inductive filter present in the output circuit.

The D. C. output voltage is obtained as the average of A.C. input voltage, V_{cp}

$$E_0 = \frac{1}{\pi}\int_0^{\pi} \sqrt{2}V_{cp} \sin \omega t d\left(\omega t\right) \tag{1}$$

$$E_0 = \frac{2\sqrt{2}}{\pi}V_{cp} \tag{2}$$

ω = 2πf and f is the switching frequency. The rms value of the fundamental component of Diode Bridge current is calculated using Fourier analysis as

$$I_b = \frac{1}{\sqrt{2}\pi}\int_0^{2\pi} i_b\left(t\right)\sin \omega t d\left(\omega t\right) \tag{3}$$

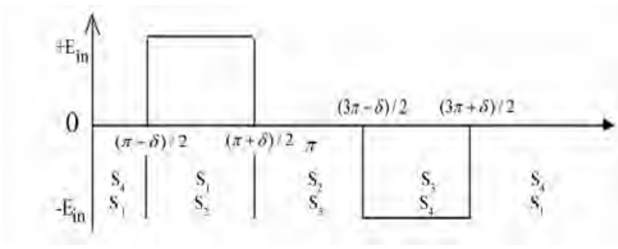

Figure 4. Quasi-square voltage waveform of LCC resonant converter.

$$I_b = \frac{2\sqrt{2}}{\pi} I_0 \tag{4}$$

Using Equation (2) & (4) the equivalent A. C. resistance as seen at the input of the rectifier bridge is given by

$$R_{ac} = \frac{V_{cp}}{I_b} = \frac{\pi^2}{8} R_L \tag{5}$$

δ and D are related by:

$$\delta = \pi D \tag{6}$$

The duty ratio D is defined as the ratio of the time duration for which the switch S_1 & S_2 or S_3 & S_4 are switched on simultaneously i.e. t_{on} to the half of the switching period (T/2) i.e., $D = t_{on}/(T/2)$.When the switches S_1 and S_2 (S_3 or S_4) are switched on simultaneously, the voltage across A and B is the input voltage E_{in}.

The R.M.S. fundamental Voltage across A and B is given by:

$$V_{AB} = \frac{1}{\sqrt{2}\pi} \int_0^{2\pi} V_{AB}(t) \sin \omega t d(\omega t) \tag{7}$$

$$V_{AB} = \frac{1}{\sqrt{2}\pi} \left[\int_{(\pi-\delta)/2}^{(\pi+\delta)/2} E_{in} \sin \omega t d(\omega t) - \int_{(3\pi-\delta)/2}^{(3\pi+\delta)/2} E_{in} \sin \omega t d(\omega t) \right] \tag{8}$$

$$V_{AB} = \frac{2\sqrt{2} E_{in} \sin \delta / 2}{\pi} \tag{9}$$

The equivalent circuit of the converter across the terminal A and B shown in Figure 2 is replaced by its equivalent circuit shown in Figure 5. In order to simplify the presentation, all the equations are normalized using the following base quantities.

Base voltage = E_{in}

Base impedance = $\omega_0 L$

Base current = $E_{in} / \omega_0 L$

Base frequency $\omega_0 = 1/\sqrt{LC}$

The RMS fundamental voltage across the parallel capacitor C_p is given by:

$$V_{cp} = \left[\frac{V_{AB}}{j(X_L - X_{cs}) + \frac{1}{\frac{1}{R_{ac}} - \frac{1}{jX_{cp}}}} \right] \times \left(\frac{1}{\frac{1}{R_{ac}} - \frac{1}{jX_{cp}}} \right) \tag{10}$$

here

$$X_L = \omega L,\ X_{cs} = 1/\omega C_s,\ X_{cp} = 1/\omega C_p \tag{11}$$

Substituting the Equation (11) in Equation (10), the equation becomes

$$V_{cp} = \frac{V_{AB}}{1 + \frac{C_P}{C_S} - \omega^2 L C_P + j\frac{8}{\pi^2}} \times \frac{\omega L}{R_L} - \frac{1}{\omega C_S R_L} \tag{12}$$

Substituting the Equation (9) in Equation (12) and after simplification, the equation becomes

$$V_{cp} = \frac{2\sqrt{2} E_{in} \sin \delta / 2}{\pi \times \left[\left(\frac{m+1}{m} \right)(1-y^2) + \frac{8}{\pi^2} jQ \left(y - \frac{1}{(m+1)y} \right) \right]} \tag{13}$$

where

$$m = C_s / C_p,\ Q = \omega_o L / R_L = 1/\omega_o C R_L,\ y = \omega/\omega_o \tag{14}$$

Substituting Equation (13) in Equation (2) and after normalization, the equation becomes

$$\frac{E_0}{E_i} = \frac{\sin \delta / 2}{\frac{\pi^2}{8} \left(\frac{m+1}{m} \right)(1-y^2) + jQ \left(y - \frac{1}{(m+1)y} \right)} \tag{15}$$

The equivalent impedance across the terminals A and B is given by

$$Z_{eq} = j(X_L - X_{CS}) + \frac{1}{\frac{1}{R_{ac}} - \frac{1}{jX_{CP}}} \tag{16}$$

Substituting Equation (5), Equation (11) in Equation (14), the equation becomes

$$Z_{eq} = \left[j\left(\frac{\omega L}{R_L} - \frac{1}{\omega C_S R_L} \right) + \frac{1}{\frac{8}{\pi^2} + j\omega C_P R_L} \right] \tag{17}$$

Using Equation (11) in Equation (17) and after simplification, the equation becomes

$$Z_{eq} = \left[jR_L Q \left(y - \frac{1}{(m+1)y} \right) + \frac{1}{\frac{8}{\pi^2} + j\frac{y(m+1)}{Qm}} \right] \tag{18}$$

After simplification and rearranging the terms we get

$$Z_{eq} = \omega_0 L \frac{B_1 + jB_2}{B_3} \tag{19}$$

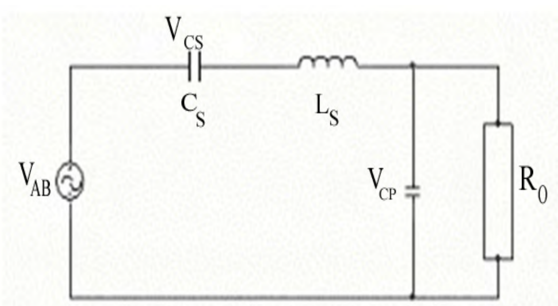

Figure 5. AC equivalent circuit of resonant converter.

where

$$B_1 = \frac{8Q}{\pi^2}\left[\frac{m}{y(m+1)}\right]^2 \quad (20)$$

$$B_2 = \left[y - \frac{1}{y(m+1)}\right]B_3 - \frac{m}{y(m+1)} \quad (21)$$

$$B_3 = 1 + \left[\frac{8Qm}{\pi^2 y(m+1)}\right] \quad (22)$$

Normalizing Equation (19), the equation becomes

$$Z_{eqpu} = \frac{B_1 + jB_2}{B_3} = \left|Z_{eqpu}\right| e^{j\Psi} \quad (23)$$

$$\left|Z_{eqpu}\right| = \frac{\sqrt{B_1^2 + B_2^2}}{B_3^2} \quad (24)$$

Impedance angle

$$\Psi = \tan^{-1}\frac{B_1}{B_2} \quad (25)$$

The resonant link current I

$$I = \frac{V_{AB}}{Z_{equ}} \quad (26)$$

$$I = |I|\angle -\psi \quad (27)$$

where

$$|I| = \frac{V_{AB}}{\left|Z_{equ}\right|} \quad (28)$$

Substituting Equation (9) in Equation (4) and after normalization, the equation becomes

$$|I|_{pu} = \frac{2\sqrt{2}\sin\frac{\delta}{2}}{\pi\left|Z_{equ}\right|} \quad (29)$$

Peak Inductor is given by

$$|I|_{ppu} = \sqrt{2}\,|I|_{ppu} = \frac{4\sin\frac{\delta}{2}}{\pi\left|Z_{equ}\right|} \quad (30)$$

$$\left|V_{cs}\right|_{ppu} = |I|\frac{X_{cs}}{\omega_0 L} \quad (31)$$

Using (30) Peak Voltage across C_s is calculated as

$$\left|V_{cs}\right|_{ppu} = \frac{|I|_{ppu}}{y(m+1)} \quad (32)$$

The peak Voltage across C_P is obtained using Equation (1) and rearranging the terms.

$$\left|V_{cp}\right|_{ppu} = \frac{\pi}{2}\left|\frac{E_O}{E_{in}}\right| \quad (33)$$

The load ripple voltage is given by,

$$V_{ac} = \left[V_{crms}^2 - V_c^2\right]^{1/2} \quad (34)$$

V_{crms} is the total rms load voltage. V_o is the average load voltage.

The Voltage ripple factor, which is a measure of the ripple content, is given by the equation

$$RF = \frac{V_{ac}}{V_c} \quad (35)$$

Similarly the Voltage ripple factor using the filter elements is given by the equation

$$RipplleFactor = \frac{V_{2rms}}{V_c} \quad (36)$$

where V_{2rms} represents the rms value of the second harmonic component.

$$V_{2rms} = \frac{V_m}{3\sqrt{2}\pi\omega^2 LC} \quad (37)$$

where V_m represents the maximum value of voltage after rectification.

The efficiency of the converter is calculated using the expression

$$\%\eta = \frac{P_{out}}{P_{in}} \times 100 \quad (38)$$

4. Performance Characteristics

4.1. Variation of Input Impedance Magnitude and Phase Angle vs. Normalized Switching Frequency

The effect of impendence on circuit performance has been studied using Equation (19) to Equation (22) and have been used to draw the curves of the variation of the normalized input impedance magnitude and impedance phase angle, with change in normalized switching yield stress for various values of Q are shown in Figure 6 and Figure 7 respectively.

It can be seen that for a particular value of quality factor Q the impedance magnitude decreases as the frequency increases up to a certain value, after which it increases with frequency, but with less effect. The effect of quality factor variation can also be observed. As Q decreases the input impedance magnitude verses normalized switching frequency curve shifts towards higher frequency. It is observed that at about 0.9pu frequency, all the input impedance magnitude curve converges and diverges as the frequency increases.

From impedance phase angle curves the boundary between operation below and above resonance can be identified. The frequency at which the impedance phase

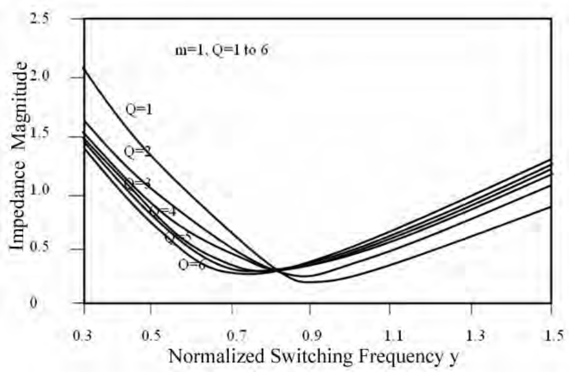

Figure 6. Variation of impedance magnitude versus normalized switching frequency for various values of Q with m = 1.

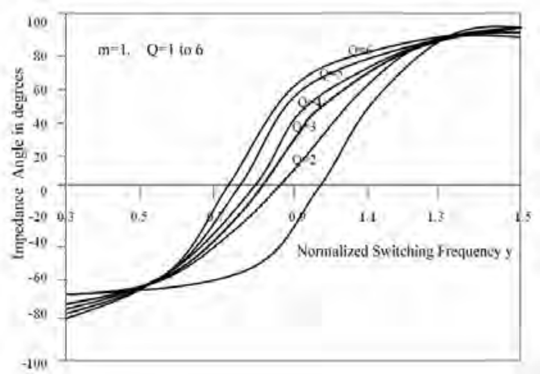

Figure 7. Variation of impedance angle in degrees versus normalized switching frequency for various values of Q with m = 1.

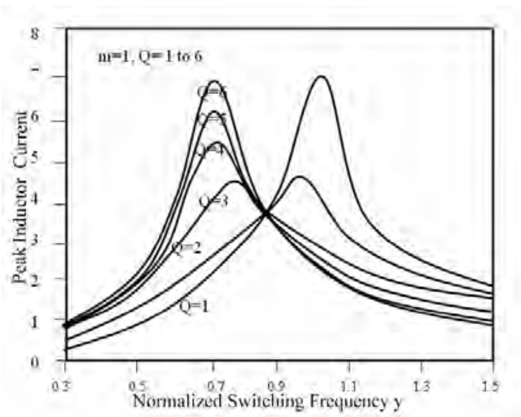

Figure 8. Variation of peak inductor current versus normalized switching frequency for various values of Q with m = 1.

angle Ψ is equal to zero is defined as f_r. This frequency forms boundary between leading power factor and lagging power factor operation. For $f<f_r$, Ψ<0, the resonant circuit represents a capacitive load (below resonance operation), for $f>f_r$, Ψ>0 the resonant circuit represents an inductive load (above resonance operation). It is seen from Figure 7 that f_r depends on Q.

4.2. Variation of Peak Inductor Current vs. Normalized Switching Frequency

Equation 30 shows that peak inductor current is a function of Q and y. Figure 8 shows that peak inductor current increases with increase in Q, since the output voltage decreases for the same output power. But for a given value of y, it can be seen peak current decreases as load current increases with increase in value of Q.

4.3. Variation of Duty Ratio vs. Q for M=1

The qualitative analysis of the relationship between duty ratio and quality factor Q is made. Figure 9 to Figure 16 show how the duty ratio D varies as Q changes, to keep output load voltage constant at particular value. These curves are obtained by solving Equation 15 numerically for duty ratio as a function of Q for various values of converter gain Eo/Ein (for 0.7 to 1.0) and various switching frequency (yield stress = 0.7 to 0.9).

It is observed that as the Eo/Ein decreases, the duty ratio versus Q curves shifts downwards. The increase in value of yield stress results in shrinkage of D vs. Q Curve ranges. However when Cs/Cp ratio is observed that the above two characteristics are intensified. The detailed analysis offers each figure is given in the following paragraphs.

If the normalized frequency is further increased, the graphs show similar pattern as described above. Figure 10, Figure 11 and Figure 12 are shown for yield stress y= 0.8,

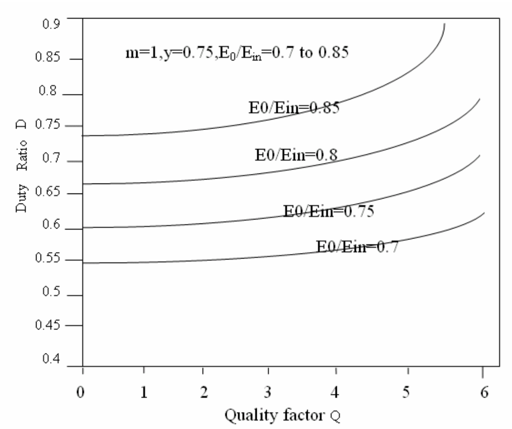

Figure 9. Variation of duty ratio versus quality factor with m = 1, y = 0.75.

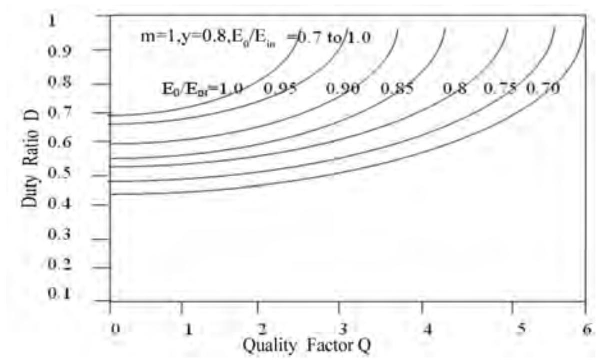

Figure 10. Variation of duty ratio versus quality factor with m = 1, y = 0.80.

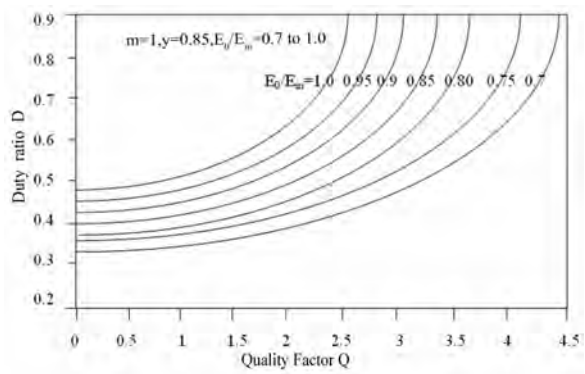

Figure 11. Variation of duty ratio versus quality factor with m = 1, y = 0.85.

0.85 and 0.9 respectively**.** Figure 13,14,15,16 show the effect of increased capacitance ratio of 2. From these graph, it is observed that as the value of yield stress changes from 0.85 to 0.9, the range of Q becomes narrower with increasing of Eo/Ein, (0.7 to 1.0). Also, at light load (Q is small), when Eo/Ein increases, the duty ratio increases while the spread of duty ratio decreases. Similarly, it becomes narrower and shifts to smaller values of duty ratio D as yield stress increases.

4.4. Variation of Duty Ratio vs. Q for m=2

Figure 13 to Figure 16 show how the duty ratio D varies as Q changes, to keep output load voltage constant at particular value. These curves are obtained by solving Equation 15 numerically for duty ratio as a function of Q for various values of converter gain Eo/Ein (for 0.7 to 1.0) and various switching frequency (yield stress = 0.7 to 0.9).

It is observed that as the Eo/Ein decreases, the duty ratio versus Q curves shifts downwards. The increase in value of yield stress results in shrinkage of D vs. Q Curve ranges. However when Cs/Cp ratio is observed that the above two characteristics are intensified. The detailed analysis offers each figure is given in the following paragraphs.

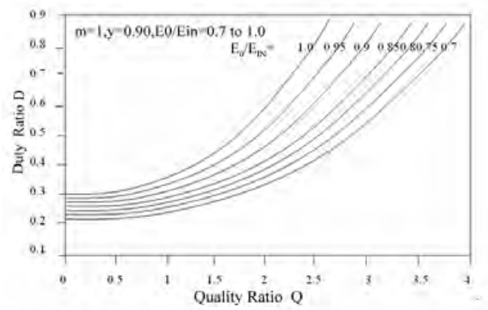

Figure 12. Variation of duty ratio versus quality factor with m = 1, y = 0.9.

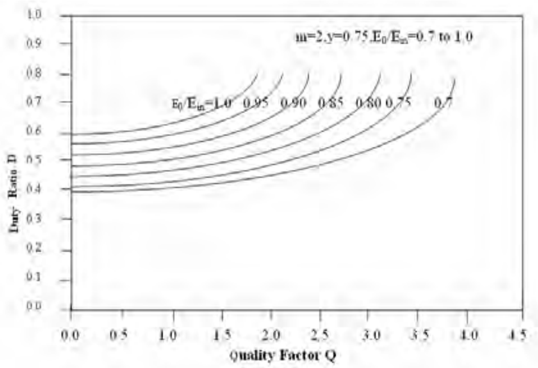

Figure 13. Variation of duty ratio versus quality factor with m = 2, y = 0.75.

If the normalized frequency is further increased, the graphs show similar pattern as described above. Figure 13, Figure 14, 15 and 16 show the effect of increased capacitance ratio of 2. From these graph, it is observed that as the value of yield stress changes from 0.85 to 0.9, the range of Q becomes narrower with increasing of Eo/Ein, (0.7 to 1.0). Also, at light load (Q is small), when Eo/Ein increases, the duty ratio increases while the spread of duty ratio decreases. Similarly, it becomes narrower and shifts to smaller values of duty ratio D as yield stress increases.

5. Design of Series Parallel Resonant Converter

Following criteria has been taken into account in order to obtain optimum design of series - parallel resonant converters.

1) Normalized switching frequency `y', such that maintains the lagging power factor conditions.

2) Minimum inverter output peak current for small rating and losses.

3) Minimum stress in series & parallel capacitor.

4) Minimum variation of Duty ratio from full load to no load i.e. good voltage regulation.

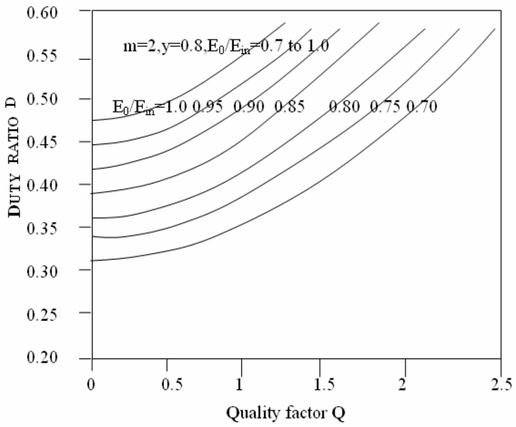

Figure 14. Variation of duty ratio versus quality factor with m = 2, y = 0.80.

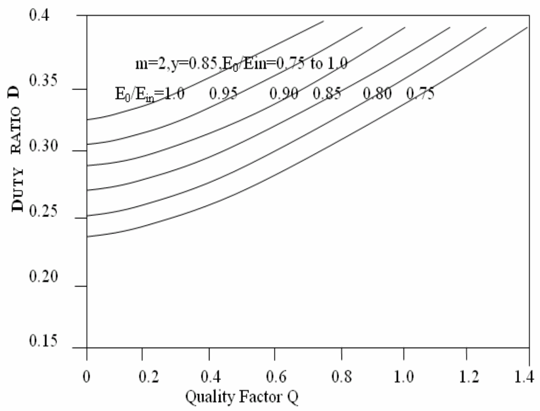

Figure 15. Variation of duty ratio versus quality factor with m = 2,y = 0.85.5.Design of series parallel resonant converter.

5.1. Selection of Cs/Cp (m)

It is observed from Figure 10 and Figure 14 that as m increases, the variation in the duty ratio required to keep the output constant decreases. For regulation of output voltage, the duty ratio has to be varied over larger range for m = 1.compared to m = 2. The effect of m on equivalent input impedance of the resonant network should be considered

while taking the values of m. From Equation (19) which is used to plot the variation of equivalent input impedance Zeqpu with the variation on normalized switching frequency and is shown in Figure 6. From the equation it is observed that as m increases from 1 to 2 the equivalent input impedances Zeqpu of resonant network decrease. This result in increased peak current through various components and consequently increased power loss. So from these considerations, the value of m = 1 should be taken.

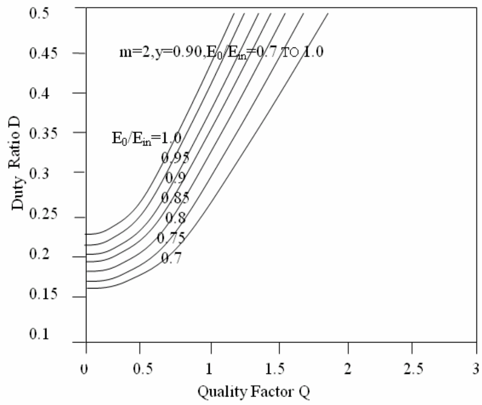

Figure 16. Variation of duty ratio versus quality factor with m = 2, y = 0.90.

5.2. Selection of Normalized Switching Frequency

The output voltage is regulated at all load by proper selection of y. In Figure 10 for y = 0.75 the output voltage can be regulated at Eo/Ein = 0.8 for the variation in Q up to 6. But at y =0. 8, the output voltage can be maintained at this value of only up to Q = 5 (Figure 11). As y increases further, the range of Q up to which the converter can be regulated decreases. This implies that too high value of y cannot be chosen especially when wide load variations are expected. Besides, y should not be of low value. Otherwise operation above resonance may not possible. Keeping these two factors in mind, y = 0.8 have been chosen. It can be seen from figure 10 that for variation in Q up to 5, Eo/Ein =0.8 can be maintained. As shown in Figure 7, for y =0.8, the input impedance angle changes from positive to negative as the values of Q is changed from 5 corresponding to full load to 1 for light load. This means that near full load, the converter operates above resonance and at partial loads the converter operates below resonance.

5.3. Selection of Tank Circuit Q at Full Load

Size of tank depends upon the value of quality factor Q and it should not be large. Equation (19), Equation (20), Equation (21), Equation (22) and Equation (30) show that peak inductor current is a function of Q and y. Figure 8 shows that peak inductor current increases with increase in Q, since the output voltage decreases for the same output power. But for a given value of y, it can be seen that the peak inductor current decreases as load current increases with increase in value of Q. However this decrease is not drastic for values of Q greater than 5. A compromised value of Q = 5 is chosen in this design.

5.4. Selection of Normalized Converter Gain

It is clear from the circuit topology that output current is

rectified and averaged tank current reflected to the secondary side of the transformer. Since the tank current is directly related to the output current, therefore we should choose a large conversion ratio, so that the turns ratio is minimized, resulting in the smallest possible tank current on the primary for a specified output current on the secondary. Hence the conversion ratio should be chosen close to one. Based on above consideration, the following optimum values are selected in the design of the converter.
Normalized frequency y = 0.8.
Cs/Cp ratio m = 1
Q of tank circuit at full load = 5

6. Design

Input voltage E_{in} = 50 volts. Output voltage E_o =40 volts. Output Current = 1.2 Amps. Switching frequency = 100 kHz

From the performance characteristics, the following values are considered for design.m=C_s/C_p = 1, Q=5, y=1.1
Load resistance $R=V_0/I_0=32\Omega$

$$R=\frac{\omega_0 L}{Q}=\frac{1}{Q}\times\sqrt{\frac{L}{C}}$$

$$\sqrt{\frac{L}{C}}=Q\times R=5\times 32=160$$

Resonant frequency f_o is given by $f_o = f/y$ = 100,000/1.1 = 90.9 kHz
But

$$f_0=\frac{1}{2\pi\sqrt{LC}}$$

$$\frac{1}{\sqrt{LC}}=2\pi\times 90.9\times 10^3$$

The values of L & C are L = 280μH and C = 0.01 μ F.

7. Experimental Results

This section aims to validate the concepts developed in the previous sections. This section is intended to highlight the compliance of the proposed converter with the desired design specifications. Some testing results are presented in this section to verify the theoretical predictions of previous sections. An experimental proto type has been implemented for a resistive load as shown in Figure 17. The load rating is 40V, 50W, 1.2A. The resonant inductor is 0.28mH and the inductor is wound around ferrite core and the series resonant capacitor is 0.01μF and the capacitor used is of polypropylene film type.

The switching frequency is 100 KHz. All the four switches used is of IRF450 with an external fast recovery diode BYE26E connected across each switching device. In the secondary side, the diodes used for rectification are FR306. The filter inductor is 40μH and is wound around ferrite core. The filter capacitance is 100μF, 63V and the capacitor used is of electrolytic type. Figure 16 to Figure 18 shows the experimental output obtained. In each Figure, (a) shows the voltage across the series inductor and (b) shows the output voltage across the load after connecting the filter elements.

Table 3 efficiency obtained with conventional method (without LC) for variable I/P D-C supply voltage and switching frequency = 100 kHz

Table 4 efficiency obtained for series parallel resonant converter (proposed method) for I/P D-C supply voltage = 30 V and switching frequency = 100 kHz.

Table 1&2 give the Comparison of Results between Calculated and experimental results respectively of Series parallel resonant converter for an input DC supply voltage of 50V and switching frequency of 100 kHz**.**

Table 1. Calculated results.

Load %	Duty Ratio D	Series capacitor voltage Vcs(peak) volts	Series inductor voltage V_{LS}(peak) volts	Output current I_0 amps	Output voltage V_0 volts	Ripple Factor without filter %	Ripple Factor with filter %
100	0.8	385.4	468.9	1.2	40	18.1	0.0048
80	0.71	318.5	394.2	0.96	40	17.5	0.0034
60	0.64	245.6	325.6	0.72	40	16.6	0.0029
40	0.57	158.6	247.2	0.48	40	15.3	0.0016
20	0.49	73.1	143.4	0.24	40	14.9	0.0007
10	0.42	46.5	86.9	0.12	40	13.6	0.0001

Table 2. Experimental results.

Load %	Duty Ratio D	Series capacitor voltage Vcs(peak) volts	Series inductor voltage V_{LS}(peak) volts	Output current I_0 amps	Output voltage V_0 volts	Ripple Factor without filter %	Ripple Factor with filter %
100	0.8	398.8	487.4	1.2	40	20.2	0.0051
80	0.7	335.6	418.5	0.96	40	19.4	0.0042
60	0.62	268.4	345.9	0.72	40	18.5	0.0035
40	0.54	185.9	265.2	0.48	40	17.3	0.0028
20	0.45	105.1	168.4	0.24	40	16.9	0.0017
10	0.39	70.6	96.4	0.12	40	15.6	0.0009

Table 3. Experimental results.

Duty Ratio	Input Current (amps)	Input Voltage (volts)	Output Current (amps)	Output Voltage (volts)	Efficiency %
0.7	1.41	50	1.2	55.9	95.56
0.7	1.19	50	1.0	56.3	94.51
0.7	0.98	50	0.8	57.6	93.44
0.7	0.76	50	0.6	58.9	92.78
0.7	0.53	50	0.4	61.2	91.96
0.7	0.27	50	0.2	62.9	91.19

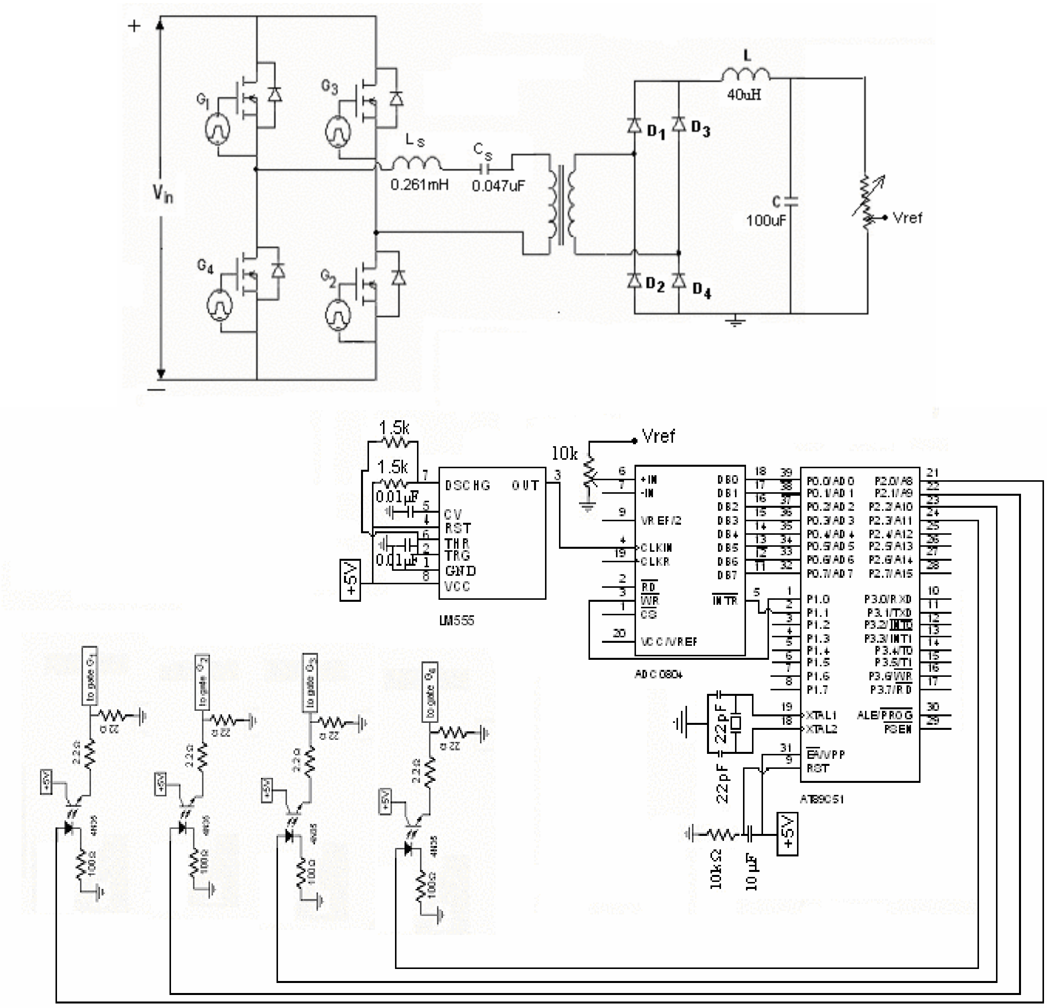

Figure 17. Experimental circuit.

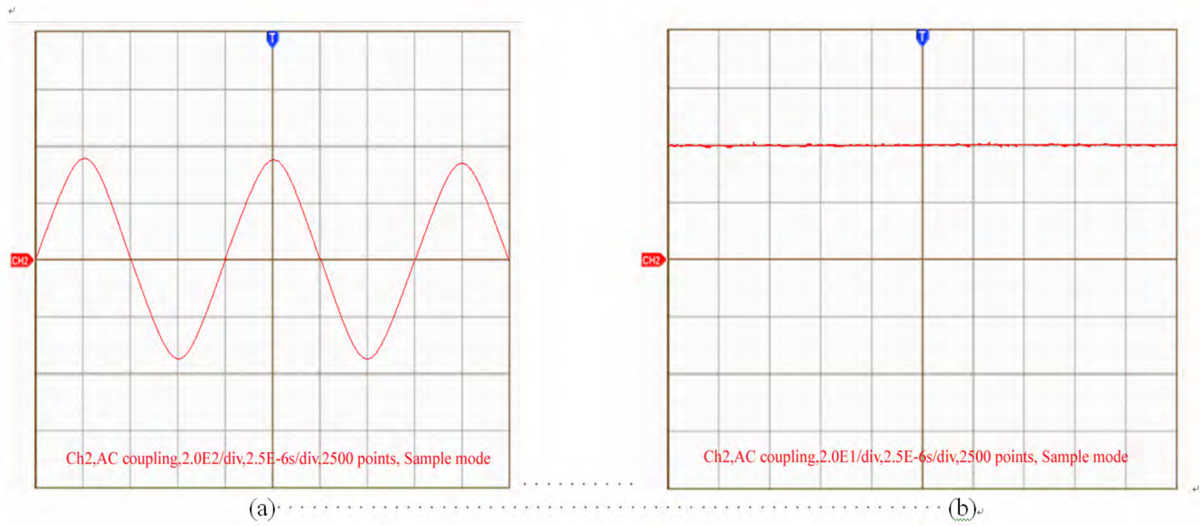

Figure 18. Experimental results for series parallel resonant converter at 60% load with m=1: (a) V_{LS}, (b) V_0 with filter.

Table 4. Experimental results.

Duty Ratio	Input Current (amps)	Input Voltage (volts)	Output Current (amps)	Output Voltage (volts)	Efficiency %
0.7	1.29	50	1.2	48.2	89.53
0.7	1.08	50	1.0	48.3	88.76
0.7	0.88	50	0.8	48.4	87.62
0.7	0.67	50	0.6	48.5	86.48
0.7	0.45	50	0.4	48.6	85.49
0.7	0.23	50	0.2	48.8	84.32

8. Conclusions

This paper presents a new front-end dc–dc power supply based on the series parallel resonant converter. A detailed design procedure has been given to select the values of the resonant components for a design case. Experimental results show that the proposed converter enjoys a high efficiency. It can be concluded from the experimental output that the variation of the working efficiency with output load power for different duty ratio is in direct proportion with the load.

9. References

[1] A. K. S. Bhat and S. B. Dewan, "Analysis & design of a high frequency resonant converter using LCC Type Communtation," IEEE Transactions on Power Electronics, Vol. 2, No. 1, pp. 291–301, October 1987.

[2] A. K. S. Bhat, "Analysis & design of series parallel resonant converter," IEEE Transactions on PE, Vol. 8, No. 1, pp. 174–182, January 1993.

[3] A. J. Foryth, G. A. Ward, and S. V. Mollow, "Extended fundamental frequency analysis of the LCC resonant converter," IEEE Transactions on PE, Vol. 8, No. 6, pp. 1286–1292, November 2003.

[4] F. Z. Peng, H. Li, G. J. Su, and J. S. Lawler, "A new ZVS bidirectional DC-DC converter for fuel cell and battery applications," IEEE Transactions on PE, Vol. 9, No. 1, pp. 54–64, January 2004.

[5] N. Jain, K. P. Jain, and J. Geza, "A zero voltage transtition boost converter employing a soft switching auxiliary circuit with reduced conduction losses," IEEE Transactions on PE, Vol. 9, No. 1, pp. 130–139, January 2004.

[6] J. M. Zhang, X. G. Xie, X. K. Wu, G. L. Wu, and Z. M. Qian, "A novel zero-current-transition full bridge DC/DC converter," IEEE Transactions on Power Electronics, Vol. 21, No. 2, pp. 354–361, March 2006.

[7] M. Z. Youssef and P. K. Jain, "A novel single stage AC–DC self-oscillating series-parallel resonant converter," IEEE Transactions on Power Electronics, Vol. 21, No. 6, pp. 1735–1785, November 2006

[8] J. H. Zhang, J. S. Lai, R. Y. Kim, and W. S. Yu "High-power density design of a soft-switching high-power bidirectional dc–dc converter," IEEE Transactions on Power Electronics, Vol. 22, No. 4, pp. 1145–1155, July 2007.

[9] Y. Lu, K. W. E. Cheng, and S. L. H. Quasi, "Current mode control for the phase-shifted series resonant converter," IEEE Transactions on Power Electronics, Vol. 23, No. 1, pp. 353–359, January 2008.

[10] W. Chen, X. B. Ruan, and R. R. Zhang, "A novel zero-voltage-switching PWM full bridge converter," IEEE Transactions on Power Electronics, Vol. 23, No. 2, pp. 793–802, March 2008.

[11] C. Zhao, X. K. Wu, P. P. Meng, and Z. M. Qian, "Optimum design consideration and implementation of a novel synchronous rectified soft-switched phase-shift full-bridge converter for low–output–voltage high–output–current applications," IEEE Transactions on Power Electronics," Vol. 24, No. 2, pp. 388–398, February 2009.

[12] A. Ecklebe, A. Lindemann, and S. Schulz, "Bidirectional switch commutation for a matrix converter supplying a series resonant load," IEEE Transactions on Power, Vol. 24, No. 5, pp. 1173–1181, May 2009.

Engineering, 2009, 1, 79-83
doi:10.4236/eng.2009.13025 Published Online November 2009 (http://www.scirp.org/journal/eng).

Applications of Data Mining Theory in Electrical Engineering

Yagang ZHANG, Jing MA, Jinfang ZHANG, Zengping WANG
Key Laboratory of Power System Protection and Dynamic Security Monitoring and Control under Ministry of Education, North China Electric Power University, Baoding, China
E-mail: *yagangzhang@gmail.com*
Received January 10, 2009; *revised February* 21, 2009; *accepted February* 23, 2009

Abstract

In this paper, we adopt a novel applied approach to fault analysis based on data mining theory. In our researches, global information will be introduced into the electric power system, we are using mainly cluster analysis technology of data mining theory to resolve quickly and exactly detection of fault components and fault sections, and finally accomplish fault analysis. The main technical contributions and innovations in this paper include, introducing global information into electrical engineering, developing a new application to fault analysis in electrical engineering. Data mining theory is defined as the process of automatically extracting valid, novel, potentially useful and ultimately comprehensive information from large databases. It has been widely utilized in both academic and applied scientific researches in which the data sets are generated by experiments. Data mining theory will contribute a lot in the study of electrical engineering.

Keywords: Fault Analysis, Data Mining Theory, Classification, Electrical Engineering

1. Introduction

Data mining is the efficient discovery of valuable, non-obvious information from a large collection of data. It is also referred to as exploratory data analysis, deals with extraction of knowledge from data. Data mining is the process of discovering interesting knowledge, such as patterns, associations, changes, anomalies and significant structures, from large amounts of data stored in databases, data warehouses, or other information repositories [1]. And data mining is usually used for very large databases, where it is normally not possible to comprehend or analyze the data because of the complexity and the immensity of the size of database. It aims at the discovery of useful information from these large databases, and it is also popularly referred to as knowledge discovery in databases (KDD). Data mining involves an integration of techniques from multiple disciplines such as database technology, statistics, machine learning, high-performance computing, pattern recognition, neural networks, data visualization, information retrieval, etc [2–4]. A common problem in data mining is to find associations among attributes of the data.

Data mining tasks have the following categories: [5]

- Class description;
- Association analysis;
- Cluster analysis;
- Outlier analysis;
- Evolution analysis.

A fault is defined as a departure from an acceptable range of an observed variable or calculated parameter associated with equipments, that is, a fault is a process abnormality or symptom. In general, faults are deviations from the normal behavior in the plant or its instrumentation. They may arise in the basic technological equipment or in its measurement and control instruments, and may represent performance deterioration, partial malfunctions or total breakdowns [6]. The analysis procedure locates the process or unit malfunction that caused the symptoms.

The goal of fault analysis is to ensure the success of the planned operations by recognizing anomalies of system behavior. As a result of proper process monitoring, downtime is minimized, safety of plant operations is improved, and manufacturing costs are reduced. Generally speaking, the process of fault analysis can be divided into three main steps: alarm, identification, evaluation.

Electric power system is one of the most complex artificial systems in this world, which safe, steady, economical and reliable operation plays a very important part in guaranteeing socioeconomic development, even in safeguarding social stability. In order to resolve this difficult problem, some methods and technologies that can reflect modern science and technology level have been introduced into this domain. Of course, no matter what kind of new analytical method or technical means we adopt, we must have a distinct recognition of electric power system itself and its complexity, and increase continuously analysis, operation and control level [7–11].

When electric power system operates from normal state to failure or abnormal operates, its electric quantities may change significantly. Relay protection is just using the sudden changes of electric to distinguish whether the power system is failure or abnormal operation. After contrasting the electric variational measurements with the electric parameters of normal system, we can detect fault types and fault locations. Furthermore, we can implement selective failure removal. In our researches, global information will be introduced into the backup protection system. After some accidents, utilizing real-time measurements of phasor measurement unit (PMU), we will seek after for characters of electrical quantities' marked changes. Then we can carry out quickly and exactly analysis of fault components and fault sections, finally, we can accomplish fault isolation. Basing on statistical theory, we have carried out large numbers of basic researches in nonlinear complex systems [12–14]. In this paper, we are using mainly cluster analysis technology of data mining theory to resolve fault detection problem in electrical engineering.

2. Electric Circuit Principle

We consider a circuit with resistors(R), inductors (L), and capacitors(C) [15]. The simplest circuit has one element of each connected in a loop. The part of the circuit containing one element is called a branch. The points where the branches connect are called nodes. In this simplest example, there are three branches and nodes. See Figure 1.

We let i_R, i_L and i_C be the current in the resistor, inductor and capacitor respectively. Similarly let v_R, v_L and v_C be the voltage drop across the three branches of the circuit. If we think of water flowing through pipes, then the current is like the rate of flow of water, and the voltage is like water pressure. Kirchhoff's current law states that the total current flowing into a node must equal the current flowing out of that node. In the circuit being discussed, this means that $|i_R| = |i_L| = |i_C|$ with the correct choice of signs. We orient the branches in the direction given in Figure.1, so,

$$i = i_R = i_L = i_C .$$

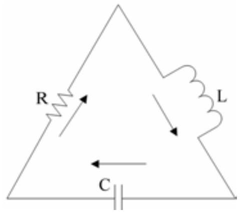

Figure 1. RLC electric circuit.

Kirchhoff's voltage law states that the sum of the voltage drops around any loop is zero. For the present example, this just means that,

$$v_R + v_L + v_C = 0$$

Next, we need to describe the properties of the elements and the laws that determine how the variables change. A resistor is determined by a relationship between the current i_R and voltage v_R. In the present section, we consider only a linear resistor given by

$$v_R = R\ i_R$$

where $R > 0$ is a constant. This is Ohm's law. In further discussions, we consider v_R as a nonlinear function of i_R or i_R as a nonlinear function of v_R.

An inductor is characterized by giving the time derivative of the current $\frac{di_L}{dt}$, in terms of the voltage v_C: Faraday's law has proved that

$$L\frac{di_L}{dt} = v_L$$

where the constant $L > 0$ is called the inductance. Classically, an inductor was constructed by making a coil of wire. Then, the magnetic field induced by the change of current in the coil creates a voltage drop across the coil.

A capacitor is characterized by giving the time derivative of the voltage $\frac{dv_C}{dt}$, in terms of the current i_C,

$$C\frac{dv_C}{dt} = i_C$$

where the constant $C > 0$ is called the capacitance.

3. Classification in the Data Mining

Classification is one of the classical topics in the data mining field. Clustering is the process of grouping data objects into a set of disjoint classes, called clusters, so that objects within a class have high similarity to each other, while objects in separate classes are more dissimilar. Clustering is an example of unsupervised classification. "Classification" refers to a procedure that assigns data objects to a set of classes. "Unsupervised" means that clustering does not rely on predefined classes and training examples while classifying the data objects. Theories of classification come from philosophy, mathematics, statistics, psychology, computer science, linguistics, biology, medicine, and other areas. Cluster analysis encompasses the methods used to:

1) Identify the clusters in the original data;
2) Determine the number of clusters in the original data;
3) Validate the clusters found in the original data.

Cluster analysis has great strength in data analysis and has been applied successfully to the researches of various fields.

Suppose there are n samples, each sample has m indexes, the observation data can be expressed as $\alpha_{ij}\ (i=1,\cdots,n,\ j=1,\cdots,m)$. The most commonly used measurement that describes the degree of relationship is distance, d_{ij} is usually denoted the distance between samples $\xi_{(i)}$ and $\eta_{(j)}$. The distance definitions in common use include:

a. Minkovski distance

$$d_{ij}(q)=[\sum_{t=1}^{m}\left|\alpha_{it}-\alpha_{jt}\right|^{q}]^{\frac{1}{q}} \qquad (i,j=1,2,\cdots,n)\ .$$

b. Lance distance($\alpha_{ij}>0$)

$$d_{ij}(L)=\frac{1}{m}\sum_{t=1}^{m}\frac{\left|\alpha_{it}-\alpha_{jt}\right|}{(\alpha_{it}+\alpha_{jt})}, \qquad (i,j=1,2,\cdots,n)\ .$$

c. Mahalanobis distance

$$d_{ij}(M)=(\xi_{(i)}-\eta_{(j)})'S^{-1}(\xi_{(i)}-\eta_{(j)}) \quad (i,j=1,2,\cdots,n)$$

Hereinto, S^{-1} is an inverses matrix of samples' covariance matrix.

d. Oblique space distance

In order to overcome the influence of relativity between variables, one can define the distance of oblique space:

$$d_{ij}=[\frac{1}{m^2}\sum_{k=1}^{m}\sum_{l=1}^{m}(\alpha_{ik}-\alpha_{jk})(\alpha_{il}-\alpha_{jl})\ \rho_{kl}]^{\frac{1}{2}}$$
$$(i,j=1,2,\cdots,n)$$

Hereinto, ρ_{kl} is the correlation coefficient between ξ_k and η_l.

4. Fault Analysis Based on Data Mining

Now let us consider IEEE9-Bus system, Figure 2 is its electric diagram. In the structure of electric power network, Bus1 appears single-phase to ground fault. By BPA programs, the vector-valued of corresponding variables is only exported one times in each period. Using these actual measurement data of corresponding variable,

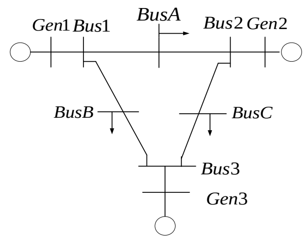

Figure 2. Electric diagram of IEEE 9-Bus system.

we can carry through fault analysis of fault component and non-fault component (fault section and non-fault section).

4.1. Fault Diagnosis Based on Node Phase Voltage

After computing IEEE9-Bus system, we can get node phase voltages at T_{-1}, T_0 (Fault), T_1, T_2 and T_3 five times, see Table 1. Figure 3 is the dendrogram of cluster analysis based on node phase voltage. The entire cluster analysis process is carried out according to the principle of similarity from high to low (distance from near to far), the order is,

Steps 1: BusC combines with BusB and forms the new BusB;

Steps 2: Bus3 combines with Bus2 and forms the new Bus2;

Steps 3: BusA combines with Bus2 and forms the new Bus2;

Steps 4: Bus2 combines with Gen1 and forms the new Gen1;

Steps 5: Gen3 combines with Gen2 and forms the new Gen2;

Steps 6: Gen2 combines with Gen1 and forms the new Gen1;

Steps 7: BusB combines with Bus1 and forms the new Bus1;

Steps 8: Bus1 combines with Gen1 and forms the new Gen1.

It can be found easily out from Figure 3 that Bus1 has remarkable difference with other buses, and the fault characteristic is obvious. These results are entirely identical to the fault location set in advance, so we can confirm exactly fault location by the cluster analysis based on node phase voltage.

4.2. Fault Diagnosis Based on Node Negative Sequence Voltage

By BPA programs, we can get node negative sequence voltage at T_{-1}, T_0 (Fault), T_1, T_2 and T_3 five times, see Table 2. Figure 4 is the dendrogram of cluster analysis based on negative sequence voltage.

Let us explain the entire process of cluster analysis in detail. The entire cluster analysis process is still carried out according to the principle of similarity from high to low (distance from near to far), the order is,

Steps 1: BusA combines with Bus2 and forms the new Bus2;

Steps 2: Bus3 combines with Bus2 and forms the new Bus2;

Steps 3: BusC combines with BusB and forms the new BusB;

Steps 4: Bus2 combines with Gen1 and forms the new Gen1;

Steps 5: Gen3 combines with Gen2 and forms the new Gen2;

Steps 6: Gen2 combines with Gen1 and forms the new Gen1;

Steps 7: BusB combines with Bus1 and forms the new Bus1;

Steps 8: Bus1 combines with Gen1 and forms the new Gen1.

From the entire hierarchical cluster process analysis, Bus1 has the lowest similarity to other nodes (the farthest distance to other nodes). Figure.4 shows that the difference of Bus-1 and other Buses is more distinct by cluster analysis based on node negative sequence voltage. So, it can also identify effectively fault location that using cluster analysis based on node negative sequence voltage.

These instances have fully proven that the analysis of fault component (fault section) can be performed by data mining theory.

5. Conclusions and Discussions

In the control of electric power systems, especially in the wide area backup protection of electric power systems, the prerequisite of protection device's accurate, fast and reliable performance is its corresponding fault type and fault location can be discriminated quickly and defined exactly. In our researches, global information has been introduced into the backup protection system. Based on data mining theory, we are using mainly cluster analysis technology to seek after for the characters of electrical quantities' marked changes. Then, we carry out fast and exact identification of faulty components and faulty sections, and finally accomplish fault analysis. The main technical contributions and innovations in this paper include, introducing global information into electrical en-

Table 1. The node phase voltages a T_{-1}, T_0 (Fault), T_1, T_2 and T_3 five times.

Bus / Time	T_{-1}	T_0 (Fault)	T_1	T_2	T_3
*Gen*1	1.0100	0.7275	0.6924	0.6814	0.6747
*Gen*2	1.0100	0.8762	0.8476	0.8327	0.8134
*Gen*3	1.0100	0.8449	0.8071	0.7909	0.7710
*Bus*1	1.0388	0	0	0	0
*Bus*2	1.0430	0.7622	0.7350	0.7217	0.7049
*Bus*3	1.0534	0.7600	0.7275	0.7134	0.6960
*Bus*A	1.0319	0.7540	0.7248	0.7114	0.6944
*Bus*B	1.0222	0.2512	0.2404	0.2356	0.2294
*Bus*C	1.0061	0.2470	0.2381	0.2336	0.2276

Table 2. The node negative sequence voltages at T_{-1}, T_0 (Fault), T_1, T_2 and T_3 five times.

Bus / Time	T_{-1}	T_0 (Fault)	T_1	T_2	T_3
*Gen*1	0	0.1330	0.1270	0.1247	0.1227
*Gen*2	0	0.0556	0.0530	0.0521	0.0512
*Gen*3	0	0.0742	0.0708	0.0696	0.0684
*Bus*1	0	0.3408	0.3252	0.3196	0.3142
*Bus*2	0	0.1058	0.1009	0.0992	0.0975
*Bus*3	0	0.1168	0.1115	0.1096	0.1077
*Bus*A	0	0.1027	0.0980	0.0963	0.0947
*Bus*B	0	0.2419	0.2309	0.2269	0.2231
*Bus*C	0	0.2287	0.2182	0.2144	0.2108

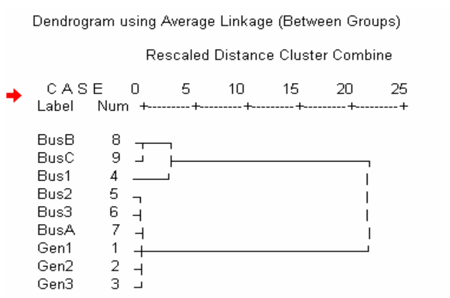

Figure 3. The dendrogram of cluster analysis based on node phase voltage.

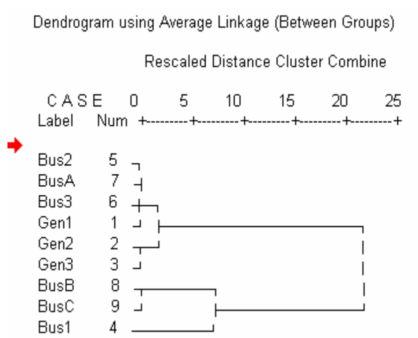

Figure 4. The dendrogram of cluster analysis based on node negative sequence voltage.

gineering, developing a new application to fault analysis in electrical engineering.

Data mining is defined as the process of automatically extracting valid, novel, potentially useful and ultimately comprehensive information from large databases. It has been widely utilized in both academic and applied scientific researches in which the data sets are generated by experiments. The most important characteristic of data mining theory is its interdisciplinarity and universality. Data mining is largely connected with machine learning in which scientists develop algorithms and techniques to find and describe potential laws in data. Generally speaking, data mining adds useful techniques to many other fields such as information processing, pattern recognition and artificial intelligence etc.

6. Acknowledgment

This research was supported partly by Key Program of National Natural Science Foundation of China (50837002, 50907021) and the Science Foundation for the Doctors of NCEPU.

7. References

[1] Y. Shi, "Dynamic data mining on multi-dimensional data," Ph. D. thesis of State University of New York at Buffalo, 2006.

[2] J. W. Han and M. Kamber, "Data mining: Concepts and techniques," Second Edition, Morgan Kaufmann, Elsevier, San Francisco, 2006.

[3] D. Dursun, F. Christie, M. Charles and R. Deepa, "Analysis of healthcare coverage: A data mining approach," Expert Systems with Applications, Vol. 36, No. 2, pp. 995–1003, 2009.

[4] Y. J. Kwon, O. A. Omitaomu, and G. N. Wang, "Data mining approaches for modeling complex electronic circuit design activities," Computers & Industrial Engineering, Vol. 54, No. 2, pp. 229–241, 2008.

[5] K. G. Srinivasa, K. R. Venugopal, and L. M. Patnaik, "A self–adaptive migration model genetic algorithm for data mining applications," Information Sciences, Vol. 177, No. 20, pp. 4295–4313, 2007.

[6] J. Cao, "Principal component analysis based fault dection and isolation", Ph. D. thesis of George Mason University of Virginia, 2004.

[7] J. X. Yuan, "Wide area protection and emergency control to prevent large scale blackout," China Electric Power Press, Beijing, 2007.

[8] L. Ye, "Study on sustainable development strategy of electric power in China in 2020," Electric Power, Vol. 36, No. 10, pp. 1–7, 2003.

[9] Y. S. Xue, "Interactions between power market stability and power system stability," Automation of Electric Power Systems, Vol. 26, No. 21–22, pp. 1–6, pp. 1–4, 2002.

[10] Q. X. Yang, "A review of the application of WAMS information in electric power system protective relaying," Modern Electric Power, No. 3, pp. 1, 2006.

[11] J. Yi and X. X. Zhou, "A survey on power system wide-area protection and control," Power System Technology, Vol. 30, pp. 7–13, 2006.

[12] Y. G. Zhang, P. Zhang, and H.F. Shi, "Statistic character in nonlinear systems," Proceedings of the Sixth International Conference on Machine Learning and Cybernetics (ICMLC), Hong Kong, Vol. 5, pp. 2598–2602, August 2007.

[13] Y. G. Zhang, C. J. Wang, and Z. Zhou, "Inherent randomicity in 4-symbolic dynamics," Chaos, Solitons and Fractals, Vol. 28, No. 1, pp. 236–243, 2006.

[14] Y. G. Zhang and C. J. Wang, "Multiformity of inherent randomicity and visitation density in *n*-symbolic dynamics," Chaos, Solitons and Fractals, Vol. 33, No. 2, pp. 685–694, 2007.

[15] R. C. Robinson, "An introduction to dynamical systems: Continuous and discrete," Pearson Education, New Jersey, 2004.

Call for Papers

ENGINEERING

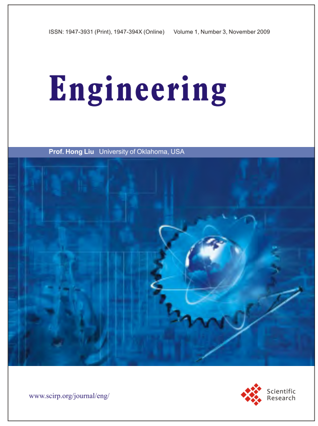

A Journal Published by Scientific Research Publishing, USA

www.scirp.org/journal/eng

ENGINEERING is an international journal dedicated to the latest advancement of engineering. The goal of this journal is to provide a platform for engineers and academicians all over the world to promote, share, and discuss various new issues and developments in different areas of engineering. All manuscripts must be prepared in English, and are subject to a rigorous and fair peer-review process. Accepted papers will immediately appear online followed by printed hard copy. The journal publishes original papers including but not limited to the following fields:

- Aerospace Engineering
- Agricultural Engineering
- Chemical Engineering
- Civil Engineering
- Electrical Engineering
- Environmental Engineering
- Industrial Engineering
- Materials Engineering
- Mechanical Engineering
- Mining Engineering
- Nanotechnology
- Nuclear Engineering
- Power Engineering
- Test Engineering
- Transportation Engineering

We are also interested in: 1) Short Reports—2-5 page papers where an author can either present an idea with theoretical background but has not yet completed the research needed for a complete paper or preliminary data; 2) Book Reviews—Comments and critiques.

☆ Notes for Intending Authors

Submitted papers should not be previously published nor be currently under consideration for publication elsewhere. Paper submission will be handled electronically through the website. For more details, please access the website.

☆ Website and E-Mail

http://www.scirp.org/journal/eng   eng@scirp.org

Engineering, 2009, 1, 133-211
Published Online November 2009 in SciRes (www.scirp.org/journal/eng/)

TABLE OF CONTENTS

Volume 1 Number 3 **November 2009**

9771947393001 03